TÉCNICO LISBOA

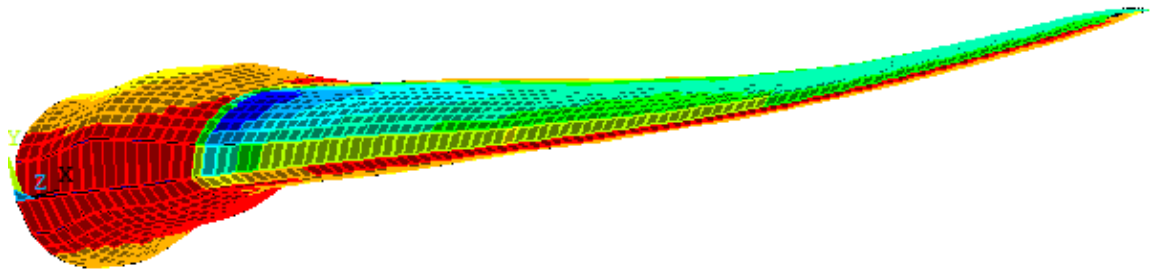

Passive Control of Aerodynamic Load in Wind Turbine Blades

Edgar Sousa Carrolo

Thesis to obtain the Master of Science Degree in

Aerospace Engineering

Supervisor: Professor André Calado Marta

Examination Committee

Chairperson:	Professor Filipe Szolnoky Ramos Pinto Cunha
Supervisor:	Professor André Calado Marta
Member of the Committee:	Doctor José Lobo do Vale

June 2015

Acknowledgments

I would like to give a word of gratitude in first place, to my supervisor André Marta for his total availability whenever I needed. He trusted in me since the beginning and gave me all the confidence to overcome the difficulties I had throughout this work. Thank you for everything! The greeting is extended to the Ph D. student Simão Rodrigues for his technical tips and advices.

I want to thank my dear friends and colleagues José and Diogo, for their concern about my progress and emotional support, not only during the dissertation period but all the university time. All those who always cared about me are also included.

Finally, I want to thank my family, whose financial support was crucial. They never put pressure on me, and gave me freedom to follow my own path, always demonstrating their confidence on me. I hope, from now on, through the working tool you gave me opportunity to get, reward all the effort you done in my education ever since.

Resumo

As pás de turbinas eólicas com grandes dimensões têm muitas vantagens em termos de eficiência energética, no entanto o seu dimensionamento representa um maior desafio, devido às elevadas cargas a que estas estruturas estão sujeitas.

Tradicionalmente, os sistemas de controlo activo permitem à pá adaptar-se de acordo com as condições de vento, e assim manter a sua eficiência dentro de níveis aceitáveis. Desde o final do século passado, alguns investigadores têm vindo a discutir acerca de técnicas de controlo passivo. A implementação deste tipo de resposta aerolástica não introduz peso ou manutenção adicional, ao contrário do controlo activo, porque não existem estruturas adicionais ou complementares, e é muito útil para a redução de cargas de fadiga ou optimizar a energia produzida. O objectivo passou por conseguir uma redução efectiva da carga aerodinâmica num modelo computacional de uma pá. No âmbito deste trabalho foram desenvolvidos modelos computacionais que simulam a interacção fluído-estrutura num modelo de pá aperfeiçoado, e foi considerado inicialmente num análise acoplada, apenas a carga aerodinâmica e de seguida, combinando-a com carregamentos inerciais. Os resultados demonstraram que este design reduzir em 2.1% a carga aerodinâmica na condição de um vento de velocidade máxima de operação. Uma validação estática preliminar foi realizada com sucesso, tendo em conta valores máximos de referência.

Palavras-chave: Adaptação aeroelástica, Acoplamento flexão-torção, Controlo passivo, Carregamento aerodinâmico, Interação fluido-estrutura.

Abstract

Large wind turbine blades have many advantages in terms of power efficiency, despite representing an hazard concerning the high loads applied on the structure. Traditionally, there are active control systems that allow blades to adapt according to wind conditions, and so maintain power efficiency and aerodynamic load within acceptable levels. Since the end of the last century, some researchers have been discussing about passive control techniques. The implementation of this kind of aeroelastic response does not bring additional maintenance or weight, unlike active control, because there are no additional devices or complementary structures, and is very useful either to reduce fatigue loads or optimize energy output. The main purpose was to achieve an effective reduction in aerodynamic loading in a wind turbine blade. In the scope of this work, computational models were developed that simulated the fluid-structure interaction on a enhanced blade model. Coupled analysis considering first only the aerodynamic load and then combining it with inertial were performed. The results demonstrated that this design could reduce 2.1% aerodynamic load in high wind speeds at the cut-out wind speed, thus proving to be a realistic passive control technique. A preliminary static validation of the enhanced blade model was successfully done, taking into account maximum reference values.

Keywords: Aeroelastic Tailoring, Bend-twist Coupling, Passive Control, Aerodynamic Load, Fluid- structure Interaction.

Contents

List of Tables

List of Figures

Nomenclature

Greek symbols

α	Angle of attack.
β	Twist angle.
Γ	Circulation.
λ	Tip speed ratio.
λ_r	Tip speed ratio in position r of the blade span.
ν	Poisson ratio.
Ω	Rotor rotational speed.
ω	Flow rotation speed.
Φ	Potential function.
Ψ	Stream function.
ρ	Air density.
σ	Solidity ratio.
σ_y	Yield strength.
σ_{eqv}	von Mises equivalent stress.
σ_{UCS}	Ultimate compressive strength.
θ	Pitch angle.
θ_0	Design pitch angle.
$\theta_{a.c.}$	Pitch angle due to active control systems
Π	Total potential energy.
σ	Stress vector field.
ε	Strain vector field.

Roman symbols

$[K]$ Stiffness matrix.

$[E]$ Material elastic matrix.

$[G]$ Gyroscopic matrix, shear modulus

$[M]$ Mass matrix.

$\dot{m}$ Mass flow rate.

a Axial induction factor.

B Number of blades.

c Chord.

C_P Power coefficient.

C_p Pressure coefficient.

E Young's modulus.

E_f Composite fibre Young's modulus.

EI Bending stiffness.

F Force.

GJ Torsional stiffness.

h Thermal expansion vector.

k_b Bending curvature.

k_t Rate of twist.

M_b Bending moment.

M_t Torsional moment.

P Power.

p_0 Atmospheric pressure.

q Nodal displacement vector.

R Rotor radius.

r Rotor radial position.

S Blade wetted surface.

T Torque, Temperature.

U Free-stream wind speed.

u Displacement vector field.

V Fraction in volume, velocity in a flow field in an arbitrary point .

V_{rel} Relative velocity.

Subscripts

a Aerodynamic.

f Composite fibre.

g Gravity.

l.e. Leading edge.

m Composite matrix.

n.l. Non-linear.

t.e. Trailing edge.

Superscripts

G Global reference frame.

k Iteration number.

S Surface.

T Transpose.

t Thermal.

V Volume.

Glossary

BEM Blade Element Method is a 2D classical method to determine aerodynamic coefficients and forces applied on a blade annular element.

BTC Bend-Twist Coupling is the elastic coupling between bending and torsion in composite structures, similar to beams, governed by the anisotropic properties of composite materials.

CFD Computational Fuid Dynamics is the computational fluid mechanics field that uses numerical tools in to solve fluid flow problems.

CSM Computational Structural Mechanics is the structural engineering field that applies numerical methods to solve structural problems, either static or dynamic.

FEM Finite Element Method is a numerical method to find approximate solutions of partial differential equations dividing the domain in smaller parts called finite elements.

FSI Fluid-Structure Interaction is the interaction of deformable or moving bodies emerged in a fluid flow creating steady or oscillatory perturbations.

HAWT Horizontal-Axis Wind Turbines are the most common configuration of wind rotors, where the rotation axis is parallel to the ground.

Chapter 1

Introduction

1.1 Motivation

Along the History, the way humanity has been looking at wind energy has suffered several mutations. During many centuries, the use of wind energy was limited to charge low-power systems at home, but as soon as electrical grid became available, wind energy was quickly replaced. Nevertheless, there were some sparse applications of wind turbines, essentially in Europe, where some avant-garde scientists wanted to be noticed in this area and contributed with their ideas. Until the last quarter of the twentieth century, there was in general, little interest to invest in this area.

Since then, several factors have contributed to the way in which we look at wind energy. The dramatic rise of oil price forced all entities to seek for alternatives. Wind energy seemed to be a logical investment, since it had been used in the past in farms (windmills were used to transform wind energy into mechanical energy), and given that wind is available anywhere on Earth. Furthermore, in that time developments were made in the technological field, as well as in others, that were significant enough to sustain the investment and revolutionize wind turbines. These factors, associated with adequate government policies, contributed to proliferate these devices throughout Europe and North America.

The 1900s enhanced the concern about global warming, from which resulted in a strong demand for wind power generation. The wind turbines of that time had some technical issues, which were limiting production quality, but actually there was not a big concern to correct them. The increasing size of wind turbines caused new advances in many scientific areas, such as aerodynamic, material sciences and energy conversion, in order to supply the electrical needs of the 21st century. The production costs dropped in such a way that it became very competitive in comparison with conventional energy sources.

Nowadays, wind turbines are more reliable and cost effective, however, the development in this area is not over and there are still many opportunities to explore, with the consciousness that the expansion will bring more issues to overcome.

With design focus on turbine mass and cost for a given performance, it is important to include passive and active techniques to load control, thereby achieve an overall benefit to the system through improvements in turbine performance and mitigating both stress and load on the structure.

The present work aims to give an additional relevant contribution to the wind energy area and, in particular, to understand how it is possible to give a response - from a structural point of view - to the increasing size of the wind turbine blades. In this context, this report will try to give some clues on what parameters contribute the most to the structural performance of wind turbine blades and, whenever possible, change them in order to improve the structural performance, specially in situations with high wind speeds, such as gusts or wind storms.

1.2 Wind Energy Overview

1.2.1 Historic Perspective

It is unanimous that windmills served as an inspiration source to develop wind turbines. There are a few descriptions about the usage of windmills B.C., although they are not sufficiently documented. In fact, windmills came to North Europe for the first time between the 10th and 12th century, they all had an horizontal axis and were used in almost every mechanical task, but mainly for water pumping, grinding grain and as mechanical tools [9]. An example is illustrated in figure 1.1.

Figure 1.1: Windmill from the 18th century in Northern Holland [6].

Until the industrial revolution, wind was the main source of energy, and only in Europe were installed about 200 000 windmill, with Germany and Netherlands leading. From technical and technological developments those devices had already some aerodynamic sophistications. Blades acquired airfoil like shapes and twist was included. Moreover, rudimentary system of yaw control were implemented. One of the biggest developments occurred in 18th century, when the British John Smeaton discovered three basic rules that are still updated in wind energy projects [9].

- The speed of the blade tips is ideally proportional to the wind speed;
- The maximum torque is proportional to the wind speed squared;
- The maximum power is proportional to the wind speed cubed.

After the industrial revolution, coal progressively assumed the role played by windmills. It had great advantages regarding transportation, since it is possible to move coal to anywhere needed. Furthermore, coal gives the chance to adapt output power according to the actual load, contrasting with what

happens in wind energy where there is a direct dependence between output power and wind speed. The trend of decrease in number of windmills was reinforced with the appearance of the electric grid. The factories considered that wind energy was an obsolete source of energy and the maintenance costs of windmills made people invest in steam engines and electricity as main sources of energy.

In the end of the 19th century, a Danish Professor called Paul La Cour gave a great contribution to wind energy, by converting wind kinetic energy into electrical energy for the first time, based on principles he developed himself [9]. He inclusively developed his own model, show on figure 1.2.

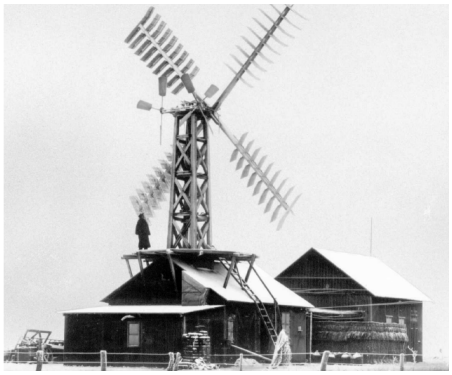

Figure 1.2: Wind turbine from Paul La Cour [7].

The oil crisis during the 1st World War became an excellent opportunity to spread wind turbines in Europe. Turbines had up to 20 m height and the output power varied between 10 and 35 kW. However, the investment dropped some years later due to the decrease in price of diesel, until the 2nd World War. Even though, this gap in investment allowed an accumulation of technical knowledge, that resulted in a quite important publication in 1925 by the physicist Albert Betz, where he proved that in a simple representation of a turbine by a shaped disk, the maximum power coefficient possible to achieve is 59.3 % [13]. This result is still valid in the present days . This kind of progress allowed improvements in rotors aerodynamics, combined with advances in material science done in aircraft industry.

In the 1950s another stable period in oil prices reigned, which along with intensive programs adopted by governments to spread electricity in rural areas, discouraged the investment in wind energy. Nevertheless, countless attempts in Europe and United States were made, particularly huge structures, but the limited hours of operation associated with rudimentary systems, due to lack of funds, conducted to an unsuccessful period in experimental area.

In the 1970s, environmental impacts of fossil fuels, launched a wide public debate at government level to seek alternatives aiming to a significant reduction of a dependency on these kind of fuel. Renewable sources, such as solar and wind energy were considered investment priorities by the companies, mainly from aerospace sector associated with NASA initiated programs of research. In Europe, Denmark, Sweden and Germany also made efforts in order to increase levels of ”clean” energy. Public funds were almost exclusively to build large wind turbine, in Megawatt range. Each country implemented its own research and experimental programmes, particularly in Canada where several trials were made with large vertical-axis wind turbines. A 64m diameter rotor still emerged but after a few years, that idea was abandoned because it was not proved that this design could overcome the efficiency verified by

the conventional one. This rotor configuration does not provide a favourable tip speed ratio and present additional problems on self-starting. However, this design cannot be completely ignored because it does not need yaw control systems and the generator can be mounted on the ground, thereby reducing the overall tower weight [20].

Already in European Union scope one seek synergies to further technological developments and tax benefits were offered in change of electrical supply by wind energy. In the United States, the State of California also reduced taxes to boost the renewable energies, however they did not have the accumulated knowledge to build turbines in series at competitive price, as the Europeans, namely the Danish. Therefore, Denmark expanded their production in order to supply the United States needs. The particular meteorological conditions of California were crucial to the installation of dozens of wind farms, in such a way that towards the end of the 20th century, approximately half of all wind energy captured in USA were mainly in California state.

In the beginning of the 21st century, concerns about wind energy competitiveness arised and the decrease energy production costs happened with construction of bigger structures. That created a new set of issues that must be solved in order to make the investment in wind energy worth in the next few decades.

1.2.2 Modern Wind Energy Context

Actual wind turbines are quite large, situated in the range of 1.5-5 MW, and are located in wind farms directly connected to electrical grid. They convert the torque generated by lift, into mechanical power, which is later converted in electrical energy by a generator. It is not possible to store that energy, and given the fact that power varies with wind speed, it is only possible to control output power and, in case of extreme wind, limit it. In some way, any system connected to wind turbine should account this fluctuations in energy supply. Despite theoretically larger wind turbines result in higher efficiency coefficients, several concerns must be taken into account.

- Noise - bigger blades have higher tip speed, thereby are noisier;
- Transportation - bigger blades are more difficult to transport on trucks;
- Manufacturing - composite molds and tools are more complex;
- Mechanical demand - larger blades create more stress on mechanical and gear components.

These issues did not avoid the increasing size of wind rotors, and further, it is expected in the future bigger blades than those that are being built presently, as illustrated in figure 1.3.

According the rules already described, there is a great dependency between wind speed and output power, therefore, an effort has been made to place wind turbines in areas with high wind speed, since doubling the wind speed means achieving eight times more power. High towers are used to take advantage from the increase of wind speed with height.

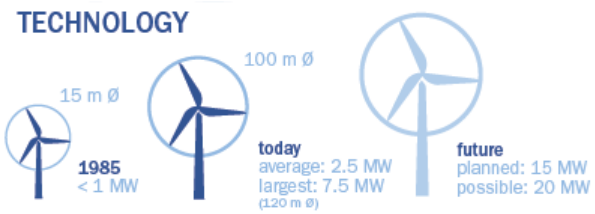

Figure 1.3: Wind turbine size evolution [8].

The effort made towards the end of the 20th century by developed countries resulted in rapid growth of installed wind turbines, which means greater power capacity. Data collected from *European Wind Energy Agency* [8] in figure 1.4, show the evolution since 1996 until 2012, and it is evident the continuously increasing wind power capacity year after year.

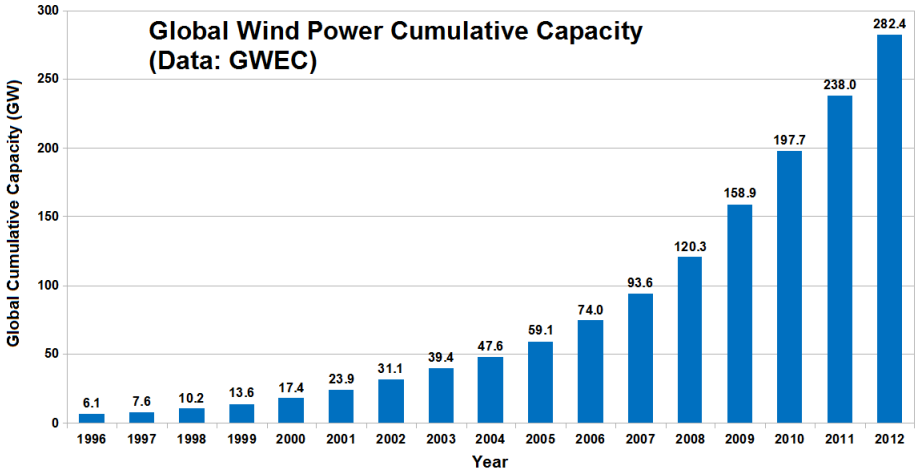

Figure 1.4: Global wind energy capacity [8].

Most part of the blades are built with glass fibre, although manufacturers are investing in new materials such as high strength carbon fibres, as they are stiffer and reduce significantly the total weight of the structure. Other parameters, as composite layer orientation and thickness distribution, are under deep discussion, but so far, there is not an optimum solution to answer these questions [21], [22].

Recently, the sea is being explored to install offshore wind turbines, because it seems to present many advantages when comparing with conventional wind turbines: the winds are stronger, more consistent and provide low turbulence [23]. Moreover, the space is not anymore a problem and it is possible to build big structures without any visual impact. However, technology to hold towers in deep sea is not fully developed yet, and further investigation should be made in this field in order to explore the sea without any kind of constraint. Furthermore, sea wind turbines maintenance cost is higher than onshore wind turbines and require special treatment to avoid corrosion episodes and non-scheduled maintenance [24].

1.3 Objectives

The present work has the objective of identifying and understanding the modern load control techniques available in wind turbine blades and their different approaches. From the assumptions of previous works, one will try to characterize the parameters that might contribute the most to the structural response of wind turbine.

An aerodynamic model will be developed to represent the aerodynamic load exclusively exerted by wind interaction in the blade structure. Similarly, a structural framework will be developed to study the static behaviour of computational model, under an aerodynamic load for a prescribed wind speed. Both models will run as a coupled interactive process in order to analyse the simultaneous response of aerodynamic load by the deformation of the structure and vice-versa.

Through a parametric study one pretend to observe which variables, due to the fluid-structure interaction, most contribute to the response of the structure, based on structural parameters, such as displacements and stresses.

Finally, from those findings, one will try to synthesize a blade configuration with corrections in parameters of interest that can provide a relief on aerodynamic load.

1.4 Thesis Outline

In chapters 2 and 3, a thorough contextualization to the work will be made. The former, will give some fundamentals about wind turbines in general and will introduce some design aspects to take into account. In the latter, it will be explained the importance to control aerodynamic load in a turbine blade, the physic mechanisms of load control and the existing approaches, with their advantages and disadvantages.

Chapters 4, 5 and 6 are the support chapters, where it is introduced all theoretical and computational bases to develop the work. In chapter 4 all aerodynamic theory is presented, beginning with simple mathematical models, until reaching computational models where it is applied the theoretical basis presented previously. The last section ends with an explanation of a simple aerodynamic model developed in this work that synthesizes all the background presented in the chapter. Chapter 5 presents the same structure, with a presentation of both theoretical and computational methods of structural mechanics and a structural model is developed with inputs from aerodynamic model, namely the load distribution. The coupling between structural and aerodynamic models is addressed in chapter 6, where is explained how it is transferred the fluid force, reflected by the pressure distribution, into a structural load distribution.

Chapter 7 includes a parametric study with a catalogued blade, aiming the characterization of the parameters which most contribute to its structural response and the understanding about a possible configuration that may actually yield an aerodynamic load mitigation.

An enhanced blade design is designed and analysed in chapter 8, based on the findings of the parametric study. This chapter qualitatively evaluate the aerodynamic load mitigation obtained with this design, and whether possible, quantify it. The final remarks are described in chapter 9.

Chapter 2

Horizontal-Axis Wind Turbines

2.1 Generic Overview

Wind turbines (WT) are devices that convert kinematic energy from wind to electrical power and have connection to an electric grid. They respond immediately to the amount of wind available but they do not allow to store any energy. They are mainly used to reduce fuel dependence [9].

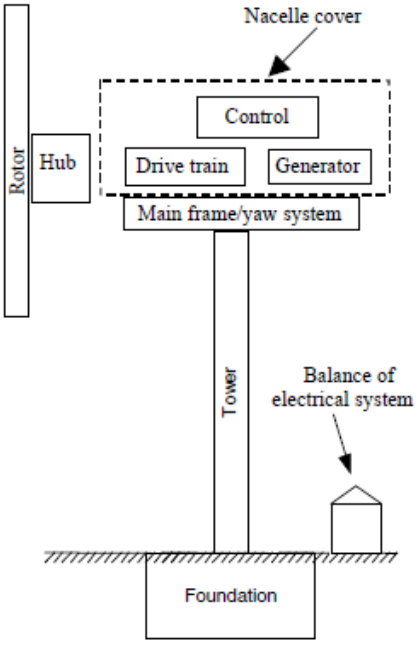

Figure 2.1: Main components of a wind turbine blade [9].

There are two possible designs to build wind turbines: horizontal and vertical axis wind turbines, although it will only be considered HAWT (rotor axis is parallel to the ground), which is the most common configuration.

The main components of wind turbines, as illustrated in figure 2.1 are listed below:

- Rotor, consisting of blades and hub;

- Drive train, consisting of the rotating parts (excluding rotor);
- Nacelle which includes, main frame, and yaw system;
- Tower and foundation;
- Control systems;
- Electrical systems, which includes cables, switch gears and transformers.

2.2 Sources of Load on Blades

The total load that the blades are subjected have different natures. They can be divided in four distinct natures:

- Aerodynamic Loads: steady and uniform wind speed with constant rotor speed generates a time-independent load, which can be calculated from blade element theory 4.1.4, that allows the estimation of lift, drag and power coefficients. Additionally, wind turbulence yields a non-periodic and stochastic component of aerodynamic, which can only be estimated with advanced numerical models [7];
- Gravitational Loads: result from a periodic spanwise bending moment. The maximum is reached when blade is horizontally positioned;
- Inertial Loads: including centrifugal loads which generates a fluctuating tensile stress, that can only be solved by non-linear methods. Moreover, the yaw movement of the rotor induces a perpendicular load to the plane of rotation, known as gyroscopic load;
- Operational Load: arising from control systems.

2.3 Power and Torque Characteristics

Power and torque are relevant input variables in the design stage, they define the overall component dimensions. These quantities are usually made non-dimensional, resulting in power and torque coefficients respectively, therefore, mathematical treatment becomes simpler, as they become a function of wind speed:

$$P = \frac{1}{2} C_P \rho U^3 S, \tag{2.1}$$

$$T = \frac{1}{2} C_T \rho U^2 S R, \tag{2.2}$$

where S is the area swept by the rotor, U_∞ is the free-stream wind speed, C_P and C_T are power and thrust coefficients respectively, and ρ is the air density. Both coefficients can be calculated from

aerodynamic models, as Blade Element Method (BEM) for a given tip speed ratio. For the correct dimensionalisation in equation (2.2), the rotor radius R, is introduced.

The main rotor features that directly influence C_P are [13]:

- Number of rotor blades;
- Chord distribution of blades;
- Aerodynamic airfoil characteristics;
- Twist distribution.

2.4 Blade Design and Properties

2.4.1 Blade Section

The blade structure should be able to support both flexural and torsional loads without compromising aerodynamic performance. The blade skin itself, would not withstand these solicitations and still maintain the same aerodynamic features. For this reason, the blades structure is reinforced with one or more shear webs, as shown in figure 2.2. This solution provides a significant structural improvement in what concerns supporting out-plane loads.

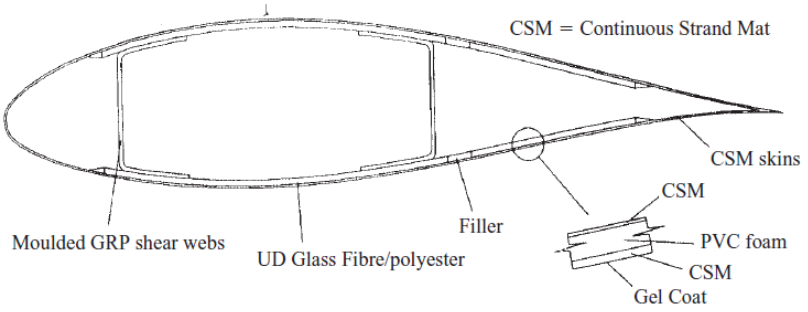

Figure 2.2: Example of blade internal structure with two shear webs[7].

Even so, the blade root does not give a relevant contribution to the total lift, whereby this zone has circular section to easily enable the inclusion of pith control bearings. This region also should be reinforced because reaction moments are concentrated in the interface between hub and blade. Then, a smooth transition zone is designed to avoid stress concentration points until about 15% of span. Airfoil sections initially are quite thick (about 40-50% of chord thickness), but that feature is mitigated along the blade span.

2.4.2 Blade Material Properties

In the past, the initial stage of rotor blade design was a discussion about the most appropriate design. Nevertheless, blade design is largely conditioned by materials criteria, and actually create barriers, mainly in manufacturing process [7]. From this assumption, it does not really make sense to select

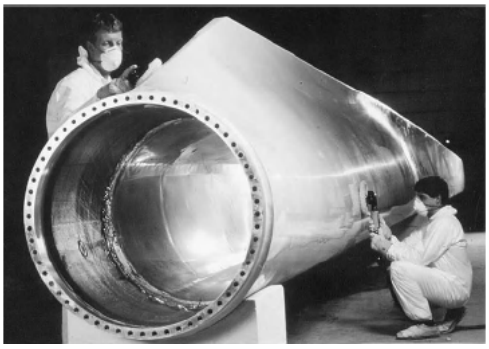

(a) Blade's root section [7]

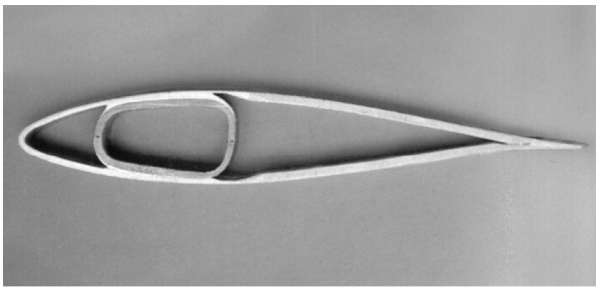

(b) Blade airfoil section

Figure 2.3: Blade sections.

materials as starting point. From the acquired experience in aircraft materials, it was possible to collect some potential materials of interest, which may be suitable to apply on a blade structure:

- Aluminium;
- Titanium;
- Steel;
- Wood;
- Fibre composite material, e.g. glass and carbon fibre.

The applied materials should satisfy demanding criteria in order to guarantee structural integrity of the structure and further, an extended fatigue life. The main factors to take into account are [13]:

- Strength-to-weight ratio;
- Fatigue strength;
- Stiffness-to-weight ratio;
- Stability parameter, $\frac{E}{\sigma_{UCS}}$.

Glass and carbon fibre composites have the best strength-to-weight ratio when compared with other materials, however since there are layers oriented in different directions, the overall strength in axial direction is significantly decreased, despite shear load resistance is improved. This kind of material verifies excellent properties in fatigue strength, namely carbon-fibre support about 30% of ultimate compressive strength [13].

The stability parameter, defined as E/σ_{UCS} is inversely proportional to buckling resistance. Since these composites have a low Young Modulus, they are not specially suited to resist to buckling. On the other hand, wood components have excellent properties in this particular point, although its low strength does not allow their implementation in blade structure, due to high stresses in operation [13].

Some rudimentary blades built in Germany and Sweden in the 1980's incorporated steel components, but they were not succeeded, mainly due their huge weight. Steel-spar blades, where only spars

and bearings were made of steel, were also developed and manufactured. These blades despite their low price, have a low strength-to-weight ratio and present corrosion issues [7]. Additionally, machining process with steel becomes particularly problematic, mainly when producing twisted sections, whereas composites can be moulded to obtain the desired form, which make them very interesting [13]. These two factors make steel usage almost infeasible.

Globally, carbon composites present the most suitable properties to implement in blades but, unfortunately, they are also the most expensive option. Therefore, often one seeks an intermediate solution with either glass/epoxy or wood/epoxy composites, that still assure good structural performance. They have excellent performance in fatigue strength, but only when they are combined with other materials to compensate their low Young's modulus.

2.4.3 Airfoil Optimization

Standard NACA airfoils employed in aircraft were used in rotor blades for a long time. After years of investigation, the conclusion was that a potential gain could be obtained, just with new airfoils developed exclusively to implement in WT, as seen in figure 2.4. These airfoils do not carry extra cost in development and can improve the aerodynamic efficiency and ultimately reduce energy cost yielded [7]. Blades sections present significant differences in root, and in the tip where it incorporates optimized shapes.

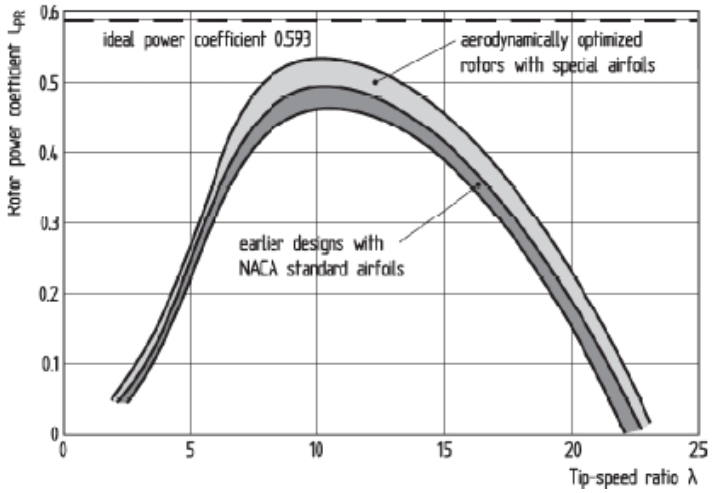

Figure 2.4: Evolution in power efficiency [7].

2.4.4 Number of Blades

The number of blades are still a subject of large discussion, even though it is possible to estimate the output power of a rotor, regardless of its configuration. Therefore, it means that the influence of the number of blades is sufficiently small to be neglected during these kind of calculations. A simple argument to support this assumption is that a rotor with less blades is able to rotate faster, thus can compensate the fact of having a reduced wet area [7].

Figure 2.5 clearly explains itself why rotors usually do not have more than 3 blades. The theoretical

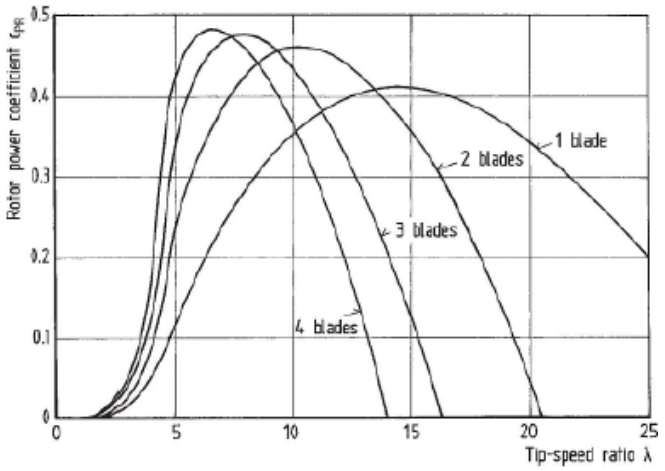

Figure 2.5: Power efficiency vs. tip speed ratio for different number of blades [7].

overcome obtained with the addition of one blade is not worth the increase in cost to make it. On the other hand, rotor single or double-bladed rotors require high tip-speed ratios, which cause high noise emissions [7].As a fact, preclude the implementation of these design in many regions.

2.4.5 Blade Twist Design

Since the flow velocity increases towards blade tip, the angle of attack also changes along the span. In order to keep lift coefficient within acceptable values, the geometric shape is twisted, and so maintain angle of attack constant.

Unfortunately, for constant speed rotors, it is only possible to reach an optimized shape for one wind speed, which obviously bring losses to other wind speed conditions. From the manufacturing point of view, it is legitimate to question about whether it is really necessary to build a twisted blade, as it implies a more expensive design.

Figure 2.6, shows that the aerodynamic benefits underlying this design cannot be neglected, and as such all WT have some twist in their design.

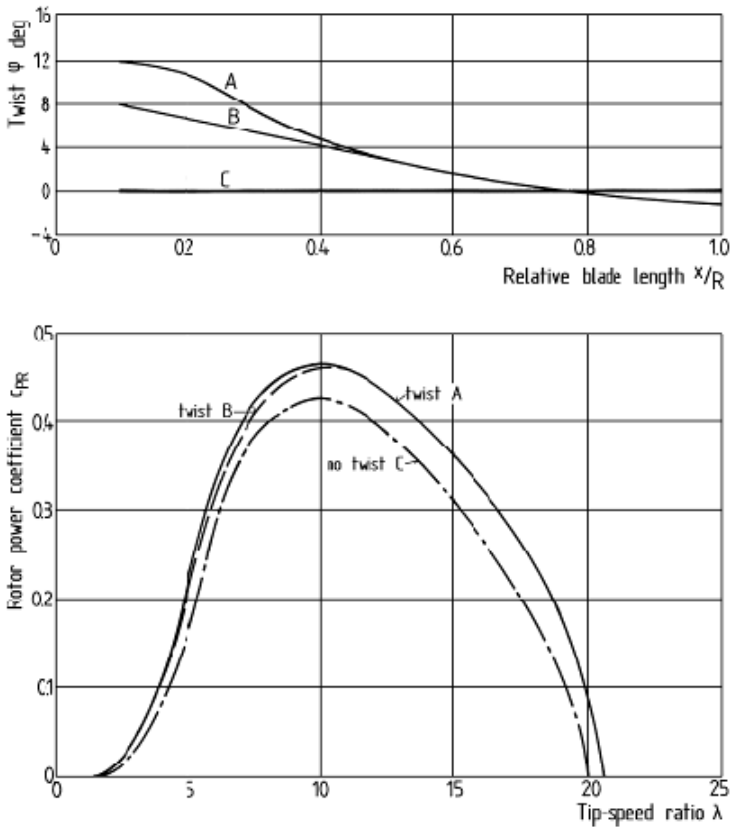

Figure 2.6: Twist vs Relative blade length ; power coefficient vs tip speed ratio for three different twisted blades [7].

2.4.6 Blade Thickness

Whereas in aerodynamic field one seeks thinner airfoil shapes to achieve better aerodynamic performances, structural requirements not rarely impose thicker shapes with penalties on the structure weight. Thus, a trade-off between aerodynamic efficiency and structure stiffness is crucial to obtain an optimum design. In particular, spar caps thickness represent the major challenge to build a light blade, but yet sufficiently robust and further with good performance fulfilling the output energy that was designed [7].

2.4.7 Tip-Speed Ratio

The first wind turbines had the rotor speed as close as possible to an electric generator. Otherwise, heavy gearboxes with high gear ratios were needed, which were also costly. Gradually, they could be manufactured at much lower price and working more efficiently. Such progress prevented the blades to have high tip speed ratios[1], although eventually some useless weight were added to the blade. Actually, high tip speed ratios are appreciated and desired because they can avoid the rotor to achieve excessive rotational speeds [7]. In addition, solidity ratio is mitigated. This quantity is the fraction of volume covered by the blades, meaning that less material is spent in the manufacturing process, so might be possible to achieve savings in this point.

[1] see the definition of tip speed ratio on section 4.1.3

Chapter 3

Aerodynamic Load Control

Whenever a turbine blade is subjected to adverse atmospheric conditions, when extreme wind speeds might occur, the load for which it is designed can be far exceeded. This assumption is reinforced when one is dealing with large blades. Thus, arises the concern of mitigating these loads in order to preserve the structure integrity.

In this context, through aerodynamic load control, it is possible to manage the amount of load carried by the structure, reduce the fatigue damage and, thereby, enhance the overall efficiency. The final idea is to change the blade aerodynamic features simultaneously, according the atmospheric conditions, namely wind speed. The load control can be classified in active or passive, as detailed in the following sections.

3.1 Active Load Control

In the beginning of wind energy industry, turbines operation was simple due their small dimensions. Blades were designed to regulate power exclusively by passive stall control. However, the continuous growth in size of wind turbines challenges the possibility of passive control as they were in the past. The loads on the outer surface of the blade, under extreme conditions revealed to be very penalizing, even when compared with pitch-controlled blades, causing this model to become economically unsustainable on its own [7].

Active control is a response to implementing effective load relief systems. The major advantage of this approach is that it is possible to adapt the aerodynamic properties of the blade in real time through sensors and actuators, as function of multiple variables, mainly concerning atmospheric conditions, such as wind speed, air density and blade surface roughness.

The aerodynamic load can be significantly mitigated with this control technique and, in fact, it has been completely spread in all wind turbine projects, although it loses effectiveness with increasing blade size [7]. Even though, an effective load control can prevent sudden ruptures, some studies indicate that also may extend the fatigue life of the structure [25].

3.1.1 Variable Pitch Angle Blades

There are two major distinct methods to load control through the adjustment of angle of attack. The continuous increase of the blade pitch angle, until the flow separates from the blade surface, leading to a sudden loss of lift [26]. This aerodynamic phenomenon is know as *stall*, and as consequence can limit the power output. With small variations in pitch angle is possible to achieve stall conditions, but it has been proven that flow separation brings dynamic instabilities, whose modelling becomes too heavy and amplifies the uncertainty in calculations [7]. On the other hand, a decrease in angle of attack towards *feather*, leads to a smoother and steadier solution, and is widely used in large wind turbine blades, rather than pitch control by stall. Both stall and feather are illustrated in figure 3.1.

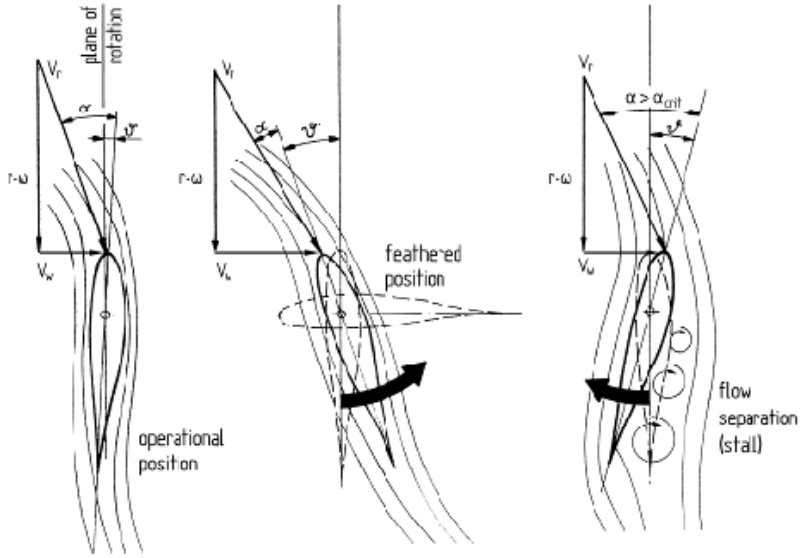

Figure 3.1: Pitch towards feather and stall [7].

From the aerodynamic point of view, it is advantageous to introduce pitch control in the full blade length. In practice, some double-bladed rotors implemented a partial pitch-control from 25-30% of span, since it still guarantees a good aerodynamic efficiency. Moreover, the manufacturing process is simplified because it becomes possible to build them in one single piece. However, in periods of extreme wind speeds, it is not possible to park all the blade in the feathered position, which eventually may cause troubles in preserving the structure integrity. Additionally, since not all of the blade span is subject to pitch variation, the variable pitch region needs a wider range compared to a full-pitched span blade.

3.1.2 Active Flow Control Techniques

Active control techniques are not just limited to the variation of wind incidence as it is illustrated in figure 3.2, and in recent years great efforts have been made to implement simple flap and tab systems, similarly to what happens in aircrafts.

Donald Lobitz, Dale Berg and Jose Zayas [27], [28] have published studies regarding the influence of these auxiliar systems, aiming to achieve significant reductions in the energy cost. They affirm that

Figure 3.2: Partial active pitch-controlled blade [7].

materials costs are growing and higher wind speed sites are located far from the urban areas, which increase the cost of energy transportation. Primarily, they theoretically concluded that ailerons positioned in the trailing edge are much more effective than in the leading edge, supported by thin airfoil theory (see appendix A) and globally all devices that change effective camber are most suitable to achieve an aerodynamic unloading . They focused their work in the study on microtabs, which are devices whose deflection is of the same order of magnitude as the boundary layer thickness. This type of devices presents definite advantages compared to the conventional size devices, since they have a quicker response and the associated aerodynamic load is greatly decreased. The most important fact is that they present similar results to the conventional design.

In a very extensive research leaded by Scott Johnson [26] are synthesized the most part of aerodynamic control techniques. Despite all techniques being able to contribute to a better performance, not all of them can effectively reduce the aerodynamic load. Nevertheless, other benefits may be achieved:

- Lower cut-in speeds;
- Reduce noise by prolonging the laminar boundary layer;
- Avoid stall conditions.

Beyond the traditional passive and active methods, namely blade pitch control, tabs and flaps, there are also cutting edge techniques of blow and suction that prevent boundary layer separation and increase the stall angle, however they will not be further investigated in this report.

3.2 Passive Load Control

3.2.1 Stall Regulation

This approach is very common in small rotor blades and load relief is done through stall conditions with increasing wind speed. Both blade geometry and rotor speed should be thoroughly chosen below optimum conditions, to guarantee that for a fixed wind speed, the flow in fact separates.

Passive approach is privileged over active control, since it provides an effective blade unloading without any additional moving parts, contrasting with what happens in active control. The obvious conclusion is that is possible to achieve significant savings in weight. Additionally, all active control systems require further attention in maintenance, because they are rather more susceptible to fail than a passive control blade design [10]. Hence, these two factors give a definitive contribution to a lower cost of energy with lower cost of manufacturing [29], [30].

However, this approach presents unpleasant issues in starting situations, that can only be overcome by using higher rotor torques. Furthermore, passive techniques do not respond to local variations, whereas active load approach can independently adapt to each blade and be more beneficial to the rotor performance [27].

3.2.2 Aerolastic Tailoring

For a long time wind turbine blades have been built with composite materials, which brings a new set of opportunities regarding the anisotropic properties of those materials. Even so, the research in this field is not sufficiently developed, specially what regards simulation tools [31].

The baseline idea of aeroelastic tailoring is to take advantage of the blade twist and passively adapt it to the incident wind loading. Goeij [10] gave an elegant definition of aeroelastic tailoring in his work: ”the incorporation of directional stiffness into a structural design to control aerolastic deformation, whether static or dynamic, in such a fashion as to affect the aerodynamic and structural performances of that structure in a beneficial way”. This design is quite interesting, since it may provide lower fatigue loads with changes in angle of attack due to sudden wind gusts. Moreover, the angle of attack may be adjusted to each wind speed to obtain an optimal torque.

3.2.3 Bend-Twist Coupling

At the end of the last century, Goeij and his colleagues [10] studied, for various box beam configurations, the implementation of bend-twist coupling (BTC) on the blade to reduce the maximum loads. The initial assumptions behind their work is that the blade deforms as a reaction to the wind incidence, so it both bends (pure bending) and twists around the rotor axis. It can twist either in the direction of stall, meaning that there is an increase in the angle of attack, or towards feather, representing a decrease in the angle of attack. It was concluded that conventional designs with single spar box beams present problems when the fibre orientation is unidirectional, and the authors suggest adding different orientations to increase the fatigue resistance. A double spar box beam design is presented. The induced twist of this configuration is necessarily lower than a conventional design, although the objective maximum load reduction may still be valid.

BTC can be obtained with a base design that includes sweep along the blade. This design creates a moment that induces twist on the blade. Another possible solution is to deviate the composite fibres away from the principal axis sufficiently to generate twist motion and decrease the load applied, taking advantage from the non-isotropic properties of composite materials.

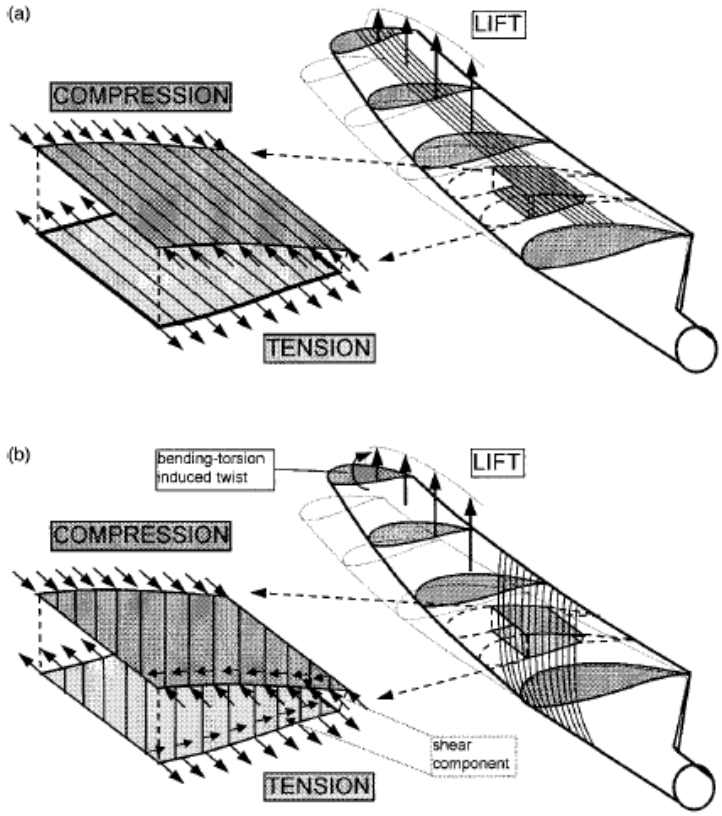

Figure 3.3: Comparison of a) conventional blade; b) bending-twist coupled blade [10].

A very recent study [5], working under the latter assumption, investigated different methods to obtain bend-twist coupled blades. The initial assumption is that this aeroelastic behaviour can be achieved with an unbalanced symmetrical stack of composite layers. The results obtained show that more unbalanced stacks cause higher levels of BTC. The BTC can be quantified from the simplified reduced cross section stiffness matrix [32],

$$\begin{bmatrix} EI & -S \\ -S & GJ \end{bmatrix} \begin{bmatrix} k_b \\ k_t \end{bmatrix} = \begin{bmatrix} M_b \\ M_t \end{bmatrix}, \tag{3.1}$$

where EI and GJ are bending and torsional stiffness, respectively, k_b is the bending curvature, k_t is the rate of twist, M_b and M_t are bending and torsional moment, respectively and S is the coupling stiffness. The normalized BTC coefficient β can be estimated by:

$$\beta = \frac{-S}{\sqrt{EI \cdot GJ}} \quad 0 < \beta < 1. \tag{3.2}$$

In the case of $S = 0$, the structure show the conventional response, given by

$$k_b = \frac{M}{EI}. \tag{3.3}$$

The BTC can be modified by changing laminate properties, in such a way that the stack becomes unbalanced. This can be done, either by changing the layer orientation, its thickness, or by further

changing the materials. The results show that BTC is improved when combining the three methods above, it means that BTC is proportional to the amount of unbalance applied on composite laminate [24].

Ashvill [33] states that bend-twist coupling can reduce fatigue and limit operating loads. He also concludes that the potential improvement is quite attractive, namely on the structural properties that can be obtained. Nevertheless, further technological improvements, such as CFD and 3D validation tools, should be achieved to justify this design manufacturing.

The comparison between stalled and feathered regulated wind turbine blades with bend-torsion coupling were also investigated [34]. For both cases, the elastic strains are greater than usual and eventually exceed the elastic limit of composite material. Twist towards feather continuously increases the turbine output power and may conduct to unstable phenomena. Twist towards stall increases the output until close to the rated value and then starts a negative trend. However, the output power above the rated wind speed may compromise the economic viability of this passive control.

BTC design in fixed-speed and variable speed rotors was explored, resulting in an equivalent power production to the uncoupled blades and significant reductions in fatigue loads. However this kind of study should be followed by aeroelastic stability studies in order to identify the limits of stable operation [25].

,

Chapter 4

Aerodynamic Model

4.1 Incompressible Potential Flow Fundamentals

This kind of flow is also known as *irrotational flow*, essentially because is assumed that the fluid particles do not rotate or distort, therefore the *vorticty* is zero. For this reason, the flow is also *inviscid*, as viscous effects are deeply related with the rotation of fluid particles. Figure 4.1 exemplifies an irrotational flow, where the local reference axis does not rotate in relation to a global reference frame.

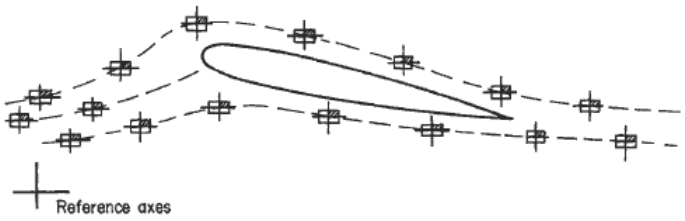

Figure 4.1: Circulation [11].

It can be demonstrated that in a velocity field, the velocity is equal to the vorticity [12]:

$$\eta = \nabla \times V \tag{4.1}$$

Thus, two situation may occur:

- $\nabla \times V \neq 0$: at every point in a flow leads to a *rotational* flow. The fluid elements have a finite angular velocity;
- $\nabla \times V = 0$: at every point in a flow leads to a *irrotational* flow. The fluid elements move in pure translation.

The total amount of vorticity in any plane region within a flow field is called *circulation*, Γ. This quantity can be seen as the vorticity flux in a region A, expressed as:

$$\Gamma = \int\int_A \nabla \times V \; dA \equiv \oint_C V \cdot ds. \tag{4.2}$$

Thus, circulation is equal to the integration in a line segment ds around a closed curve C (illustrated in figure 4.22) in the flow, whose an arbitrary point has a velocity V. Despite the lack of prediction of viscous effects on a real flow, potential flow is still extremely useful to study slender bodies at low angles of attack with attached boundary layers until the trailing edge. These conditions should be guaranteed in order to achieve accurate results, otherwise low a pressure wake is formed and the friction drag component greatly increases, which is not predicted by potential flow.

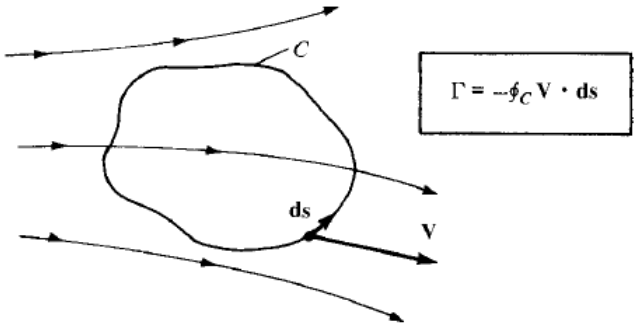

Figure 4.2: Schematic representation of a vortex [11].

From the reasoning already made, it is clear that not only drag depends on the viscous effects, but also lift only exists if viscosity is not neglected, since that is the condition to vorticity being different from zero, and therefore the presence of circulation. Thus, how to calculate lift in a inviscid flow? The *Kutta Condition* is the solution to that apparent paradox, and states that the flow should leave the trailing edge smoothly, so the velocity should be finite. That is ensured placing one or more vortices with such a strength that generates enough circulation to satisfy Kutta condition.

Recalling equation (4.1) for an irrotational flow, and considering a scalar function ϕ, then

$$\nabla \times (\nabla \phi) = 0 \tag{4.3}$$

the curl of the gradient of that function is equal to zero. From equations (4.1) and (4.3), yields

$$v = \nabla \phi, \tag{4.4}$$

which states that, for an irrotational flow, there exists a scalar function ϕ, with a velocity given by the gradient of ϕ

Futhermore, in an imcompressble flow, the time rate of change of volume of a fluid element per unit volume is zero, since in such flow the volume is constant, yielding:

$$\nabla \cdot V = 0. \tag{4.5}$$

Combining equations (4.4) and (4.5)

$$\nabla \cdot (\nabla \phi) = 0 \tag{4.6}$$

is possible to get a very familiar equation:

$$\nabla^2 \phi = 0, \tag{4.7}$$

known as the Laplace's equation.

For an incompressible flow also exists a function $\psi(x, y) = constant$, denoted by *streamline*. In cartesian coordinates:

$$u = \frac{\partial \psi}{\partial y} \tag{4.8}$$

$$v = -\frac{\partial \psi}{\partial x} \tag{4.9}$$

It also can be demonstrated that equation (4.7) can also be satisfied for stream function [12]:

$$\frac{\partial^2 \psi}{dx^2} + \frac{\partial^2 \psi}{\partial y^2} = 0. \tag{4.10}$$

The demonstration assumes that any irrotational and incompressible flow have both potential and stream function in two dimensional flow that both satisfy Laplace's equation. Conversely, any solution of Laplace's equation represents the velocity potential or stream function for any irrotational and incompressible flow. The Laplace's equation is linear, second-partial differential equation, therefore any solution of linear differential equation is also a solution of the equation.

4.1.1 Boundary Conditions

Far away from the body it is assumed that velocity is alligned with x-axis, as shown in figure 4.3, therefore it has only one component non-zero:

$$u = U, \tag{4.11}$$

$$v = 0. \tag{4.12}$$

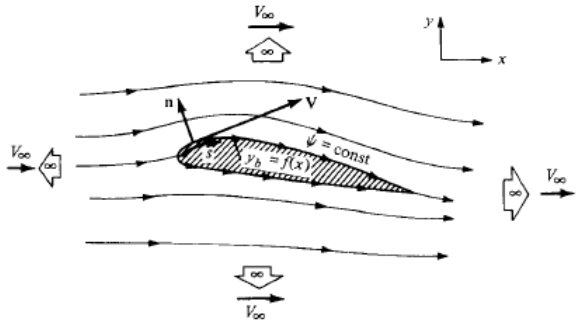

Figure 4.3: Infinity and wall boundary conditions [12].

Moreover, the fluid cannot penetrate the body; the velocity it has only tangential component on the surface, yielding

$$(\nabla\phi) \cdot n = 0, \tag{4.13}$$

where n is a unitary normal vector of the surface. This leads to the conclusion that the body surface itself is a flow streamline.

4.1.2 Vortex Flow

There are several possible flow fields to model a steady flow, however only the two-dimensional vortex will be explained with more detail, because it is part of the aerodynamic model developed. This flow can be seen as a chain of rotating particles spinning around a common axis. Potential and stream function ϕ and Φ respectively, are defined as

$$\phi = \frac{\Gamma}{2\pi}\theta \tag{4.14}$$

$$\Psi = -\frac{\Gamma}{2\pi} lnr \tag{4.15}$$

The flow has a singularity when $r = 0$, however in real situations, the viscous effects would prevent the flow velocity going to infinity and induce the flow to rotate as a solid body. The velocity only has a tangential component and the streamlines are concentric circles, as show in figure 4.4 depending only on the circulation, that measures the velocity of the flow around the origin.

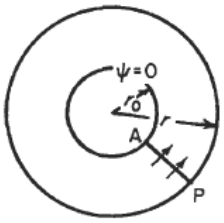

Figure 4.4: Vortex [11].

4.1.3 Actuator Disk Concept

This model was initially very useful in the beginning of last century, in the calculation of performance parameters about ship propellers. In wind energy field is frequently applied to determine limits of operation of wind turbine rotors [9]. In this mathematical concept a control volume is defined, whose boundaries are two cross section and the surface of stream flow. The rotor is represented by an ”actuator disk” like figure 4.5 , that creates a discontinuity of pressure in the stream flow that is crossing it. Several assumptions are done to perform this analysis [14]:

- Homogeneous, incompressible, steady state flow;
- No friction drag;

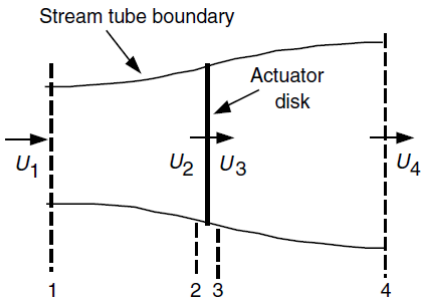

Figure 4.5: Schematic representation of 1-D wind turbine blade [9].

- Uniform thrust over rotor area;
- Static pressure far upstream and downstream of the rotor equals the ambient static pressure;

Applying the momentum conservation equation on the control volume, one can relate the total thrust with upstream and downstream velocities as

$$T = U_1(\rho AU)_1 - U_4(\rho AU)_4 = \dot{m}(U_1 - U_4), \tag{4.16}$$

where ρ is the air density, A the cross sectional area, U_i the air velocity and $\dot{m}$ the mass flow rate.

Thrust can also be expressed from the pressure difference in the actuator:

$$T = A_2(p_2 - p_3) = \frac{1}{2}\rho A_2(U_1^2 - U_4^2). \tag{4.17}$$

Reminding that $\dot{m} = \rho A_2 U_2$, it is possible to infer about velocity across the disk,

$$U_2 = \frac{U_1 + U_4}{2}. \tag{4.18}$$

Hence, in this simple model, the velocity in rotor plane is the average of upstream and downstream velocity.

The fractional decrease in wind speed velocity between upstream and rotor plane is called *axial induction factor*, and is given by

$$a = \frac{U_1 - U_2}{U_1}. \tag{4.19}$$

In a rotating wind turbine rotor, the torque imposed to the flow, induces a rotation in the opposite direction, as a reaction to the force exerted.

The rotational kinetic energy, represented in 4.6, influences negatively the total energy production and, in general, wind turbines with high torques experience more rotational kinetic energy. In this case, it is convenient to define another quantity, known as *angular induction factor*,

$$a' = \frac{\omega}{2\Omega}, \tag{4.20}$$

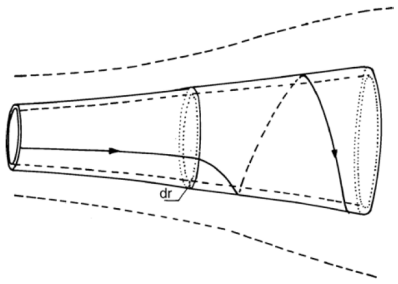

Figure 4.6: Wake rotation [13].

where ω is the flow rotational speed and Ω is the rotor rotational velocity. Thus, in general, a' is very small because upstream flow has angular velocities much smaller when compared to the rotor.

The *tip speed ratio* quantifies the ratio between tip speed and free-stream velocity as

$$\lambda = \frac{\Omega R}{U}, \tag{4.21}$$

where R is the rotor radius. If one wants to determine the speed ratio in some intermediate section, *local speed ratio* is defined as

$$\lambda_r = \frac{\Omega r}{U} = \frac{\lambda r}{R}. \tag{4.22}$$

4.1.4 Classical Blade Element Method Theory

Since all definitions to understand BEM were introduced, it is possible to determine steady loads as function of wind speed and pitch angle. The BEM applies the momentum equations to the interest region of the blade, by discretizing the stream tube in N annular elements with length dr, without flow crossing the elements.

In BEM model, some assumptions are made [14]:

- No radial dependency; what happens in one element does not influence the vicinity;
- The force applied on the flow is constant in each annular element, which corresponds to a rotor with infinite number of blades (later on it will be discussed how remove this physic impossibility).

The thrust in the control volume of figure 4.7, can be calculated from integral momentum equation as

$$dT = (U - u_1)d\dot{m} = 2\pi r \rho u (U - u_1) dr, \tag{4.23}$$

where u is the velocity at rotor plane and u_1 the downstream velocity. From ideal rotor equations, axial velocity can be expressed as function of axial induction factor,

$$u_1 = (1 - 2a)U. \tag{4.24}$$

Therefore, thrust is computed as

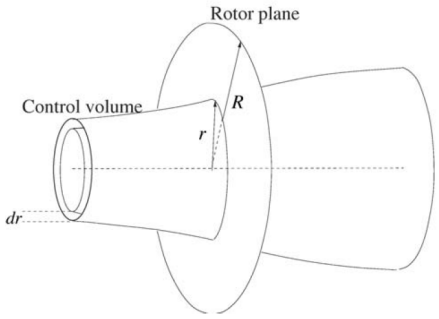

Figure 4.7: Domain control volume [14].

$$dT = 4\pi r \rho U^2 a(1-a)dr. \tag{4.25}$$

The velocity component V_{rel} in an annular section, is the vectorial combination between tangential and axial velocity in that element. Figure 4.8 makes a schecmatic representation of all velocity components and their decomposition.

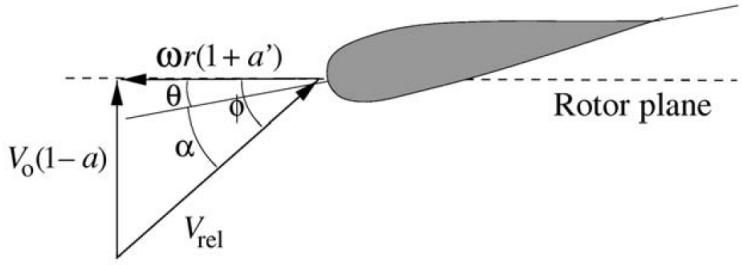

Figure 4.8: Schematic represetation of aerodynamic angles [14].

θ is the blade local pitch angle, which is the sum of design pitch angle, θ_0 and local twist angle, β. The former is measured between tip chord and rotor plane and the latter is measured relative to tip chord. ϕ is the angle between the plane of rotation and relative velocity, V_{rel}. Thus, the local angle of attack is defined as

$$\alpha = \phi - \theta. \tag{4.26}$$

From trigonometric properties, ϕ is given by:

$$tan\phi = \frac{(1-a)V_0}{(1+a')\omega r}. \tag{4.27}$$

Maintaining the same notation, then $V_0 = U$. It is also necessary to define σ, *solidity*, which is fraction of the control volume covered by the blades:

$$\sigma(r) = \frac{c(r)B}{2\pi r}, \tag{4.28}$$

where B is the number of blades, $c(r)$ is the local chord and r is radial position. From now on, $B = 1$.

4.2 Numerical Models

4.2.1 Panel Method

This well known method, was very popular among the scientific community in the 1970s, since it allows the calculation of aerodynamic properties of bodies with different shapes, thickness and orientation [12]. The main idea behind panel method is to cover the body of a vortex sheet and wrap it, as it may work as streamline of the flow [11]. A schematic representation of 2D panel method is shown in figure 4.9.

The body surface is divided in n panels, where for each one exists a vortex of strength γ_j, usually dimensionalised by a length unit, and has an unknown value.

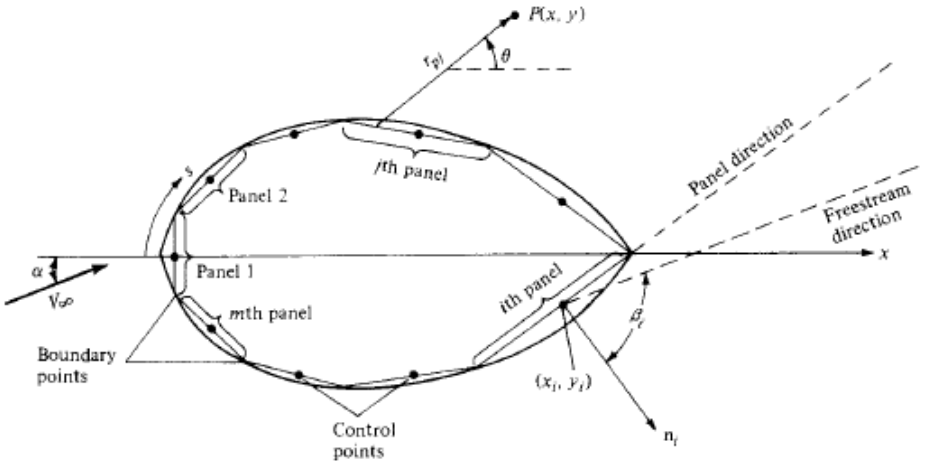

Figure 4.9: Surface discretization by panels [12].

An arbitrary point P located at a (x, y) position has an induced potential velocity due to the influence of a jth panel is given by:

$$\phi_j = -\frac{1}{2\pi}\int_j \theta_{p_j}\gamma_j ds_j, \tag{4.29}$$

where θ_{p_j} is the angle in relation to x axis of r_{p_j}, that is the distance between point P and jth panel.

$$\theta_{p_j} = atan\left(\frac{y - y_j}{x - x_j}\right). \tag{4.30}$$

The influence of all panels in potential velocity at point P is the summation of equation (4.29) over all panels:

$$\phi(p) = \sum_{j=1}^{n}\phi_j. \tag{4.31}$$

At the control points, which are in the mean position of a panel, the normal velocity is zero. This velocity is the superposition of uniform flow velocity and the induced velocity by all vortex panels. The normal component of U_n in the ith panel is given by

$$U_n = U_n cos\beta_i. \tag{4.32}$$

The normal component of induced velocity at point a (x_i, y_i) position on the vortex panel is given by

$$V_{n,i} = \frac{\partial}{\partial n_i}[\phi(x_i, y_i)] = -\sum_{j=1}^{n} \frac{\gamma_j}{2\pi} \int_j \frac{\partial \theta_{i,j}}{\partial n_i} ds_j. \tag{4.33}$$

However, the boundary condition states that the summation of the components of velocity must be zero, yielding

$$U_n + V_n = 0 \Leftrightarrow V_\infty cos\beta_i - \sum_{j=1}^{n} \frac{\gamma_j}{2\pi} \int_j \frac{\partial \theta_{i,j}}{\partial n_i} ds_j = 0. \tag{4.34}$$

Equation(4.34) generates a linear algebraic system of equations in order to determine n unknowns $\gamma_1, ..., \gamma_n$. In figure 4.10, the Kutta condition must be satisfied. This can be done in a couple different ways. The easiest solution is just equal the velocities in the points that form the trailing edge, but for an accurate solution, the gap between should be relatively close [19]. Therefore, one more equation is added to the system of equations, yielding

$$\gamma_j = -\gamma_{j-1}. \tag{4.35}$$

Therefore, the total number of equation is now $n + 1$ for n unknowns. One equation should vanish and be replaced by equation (4.35), so one control point is ignored to turn the linear system possible to solve.

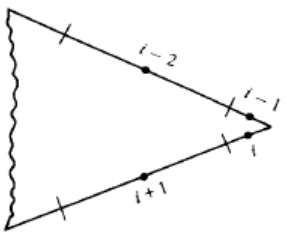

Figure 4.10: Numerical incompatibility in trailing edge [12].

Another possible solution would be the extrapolation of velocities from upper and lower surface to estimate the trailing edge velocity [19].

4.2.2 BEM Iterative Solution

This section is fundamental to understand how aerodynamic interaction affects the structure, since with BEM is possible to estimate the steady load applied on the structure, by implementing the iterative procedure that will be presented.

As any iterative solution, it is necessary to guess some initial values. In this case, both axial and angular induction factor, a and a' respectively, will be set to zero. Another possible guess would be using equations of optimum blade design [9], that will not be presented.

As shown in equation (4.36), the angle ϕ depends on a and a':

$$tan\phi_k = \frac{U(1-a_k)}{\Omega r(1+a'_k)} = \frac{1-a_k}{(1+a'_k)\lambda_r}, \tag{4.36}$$

where k is kth iteration.

It is usual apply the Prantl's tip correction factor [13] in order to take into account the pressure loss on that region:

$$F_k = \left(\frac{2}{\pi}\right) cos^{-1}\left[exp\left(-\frac{(1/2)[1-(r/R)]}{(r/R)sin\phi_k}\right)\right]. \tag{4.37}$$

Other corrections can be introduced, such as Gluaert's correction, which applies an adjustment in momentum equation due to discrepancies in torque coefficent in case of high axial induction factors, tipically grater than 0.4, where the wake is predominantly turbulent [35]:

$$C_{T_k} = \frac{8}{9} + \left(4F_k + \frac{40}{9}\right) + \left(\frac{50}{90} - 4F_k\right) a_k^2. \tag{4.38}$$

One more correction is frequently applied to the lift coefficient at inner sections of the blade. In that region, the centrifugal forces are especially strong and boundary layer thickness is significantly reduced, thereby delaying the separation phenomena [35]. Thus, the correction in lift coefficient yields:

$$C_{L_{3D}} = C_{L_{3D}} + \frac{3.1\lambda}{1+\lambda^2} g \left(\frac{c}{r}\right)^2 \left[\left(\frac{dC_{L_{2D}}}{d\alpha}\right)_{linear} sin(a_k - a_1) - C_{L_{2D}}\right], \tag{4.39}$$

where g is the blending factor that guarantees a smooth geometrical transition of polar curves.

According to equation 4.26, the local angle of attack is computed as follows:

$$\alpha_k = \phi_k - \theta_{T_k}. \tag{4.40}$$

From airfoil data, is possible to extract an interpolated C_l value and conclude the iterative process updating new values for axial and angular induction factors, closing the loop with the following expressions:

$$a_{k+1} = \frac{1}{1 + \frac{4F_k sin^2(\phi_k)}{\sigma Cl_k cos\phi_k}}, \tag{4.41}$$

$$a'_{k+1} = \frac{1}{\frac{4F_k cos(\phi_k)}{\sigma Cl_k} - 1}. \tag{4.42}$$

This set of routines should be executed until a prescribed convergence criterion is reached. Then, it is possible to access the corresponding C_p data regarding the converged angle of attack.

In the fluxogram of figure 4.11, it is possible to have a general overview about the set and sequence of routines usually applied in any BEM code.

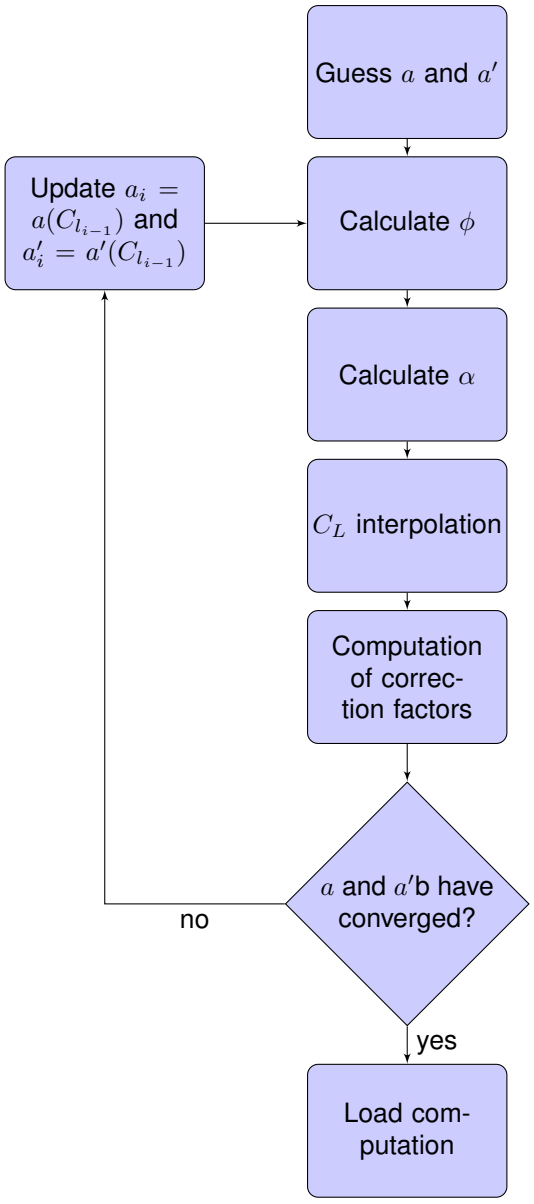

Figure 4.11: Fluxogram about BEM iterative solution.

4.3 Description of Aerodynamic Routine Program *aero_load.m*

4.3.1 Purpose and Objectives

During the course of this work, it became of particular interest automate the aerodynamic force computation regarding a fixed wind speed, therefore was developed a numerical tool in the commercial tool $MATLAB^{®}$. The algorithm obtains a pressure distribution in a blade surface, following the principles of panel method and BEM, that were briefly revisited in sections 4.2.1 and 4.2.2.

4.3.2 Input Variables

The code receives previously the mesh computed by structural model, and additionally needs an estimated value for λ .

4.3.3 Pressure distribution

From the input variables, the algorithm developed runs in the background an auxiliary software *XFoil*. This tool applies a 2-D panel method, in inviscid and incompressible flow conditions [36],[37]. It is open source, that is why it is very common in early design tests, since provides satisfactory results with very low computational effort. The software receives input variables regarding flow conditions, such as free-stream wind speed, air density, Reynolds number and Mach Number. Additionally, the airfoil section coordinates are necessary in order to perform an aerodynamic analysis. The airfoil can be created either by *XFoil* NACA airfoil generator, or from an output file containing the (x, y) coordinates of the aiorfoil. Whenever the latter option is chosen, it is necessary to pay special attention to the trailing edge coordinate. The two nearest points of trailing edge should be sufficiently distant in order to *XFoil* itself, apply the boundary conditions to meet Kutta condition. Then, the software executes the analysis and save the C_p output files, one per angle of attack. Once the blade operational angle of attack is initially unknown, this range should be sufficiently large to include the converged value obtained by BEM later on.

At the root section, it was created an exception in the C_p calculation due to numerical problems in *XFoil*. This region does not have an aerodynamic shape and *XFoil* does not converge the solution for a large number of angles of attack. Nevertheless, another simplistic solution was adopted. It was assumed that this region only contains circular sections and applying the potential flow theory, it is possible to demonstrate that for any circular section, the C_p distribution is given by [38]

$$C_{p_{r,j}} = 1 - 4sin^2\theta_{T_r}, \tag{4.43}$$

where the subscript r represent the blade radial position and j is the jth panel. Since *XFoil* is limited to 2-D C_p distributions, the C_p for all blade surface was estimated through bi-linear interpolations.

4.3.4 BEM Computation

The implementation of BEM is followed step by step as presented in section 4.2.2, so a and a' are set to 0 in the first iteration. The relative angle ϕ, depends on the tip speed ratio, λ, which depends on the blade geometry and is usually available in WT catalogues. The BEM iterative method reaches a converged solution very quickly due to the simplicity of the equations. Trials demonstrated that, typically, with less than six iterations is possible to reach a converged solution.

Recalling equation (4.40), it is important explain in detail the components of θ_{T_r}. The total pitch has three origins:

$$\theta_{T_r} = \theta_{0_r} + \theta_{a.c._r} + \beta_r, \tag{4.44}$$

where θ_{0_i} is the designed twist angle and section property, so its value remains always constant; $\theta_{a.c._i}$ is the active control pitch angle. It also remains constant during all iterations but should be set in the beginning of the simulation. This term might be useful to have an insight about coupling between

passive and active control systems; β_i is the twist of structural reaction. In each solution of BEM, θ_i remains constant, however later on when this model is combined with the structural model, in a coupled iteration, where both aerodynamic and structural models are working, β_i will change, due to surface deformation.

The converged value of angle of attack allows the access of the C_p database created by *XFoil*, and pressure distribution may be addressed to all blade surface. It should be noted that in case of two or more different airfoils are used in the blade geometry, the same number of independent BEM calculations are done, and, consequently, the number of operational angles of attack is equal to number of airfoils loaded. Since the span is discretized in a large number of sections, in a region where the same airfoil is applied (regardless of the maximum chord), an interpolation between two BEM solutions is performed to compute the remaining values of angle angle of attack.

4.4 Aerodynamic Load Computation

The aerodynamic load is directly obtained from the pressure distribution. The non-dimensional parameter of this quantity in the jth panel is given by:

$$C_{p_{r,j}} = \frac{p_{r,j} - p_0}{\frac{1}{2}\rho U^2} \tag{4.45}$$

where the p_j is the pressure in the jth panel of a radial position r, p_0 is the atmospheric pressure. The pressure due to the fluid-interaction is given by dropping p_0, thus yielding:

$$p_j = C_{p_j}\frac{1}{2}\rho U^2. \tag{4.46}$$

4.4.1 Program Routine

In the next fluxogram is given a global insight about the set of routines implemented in the code developed by the author.

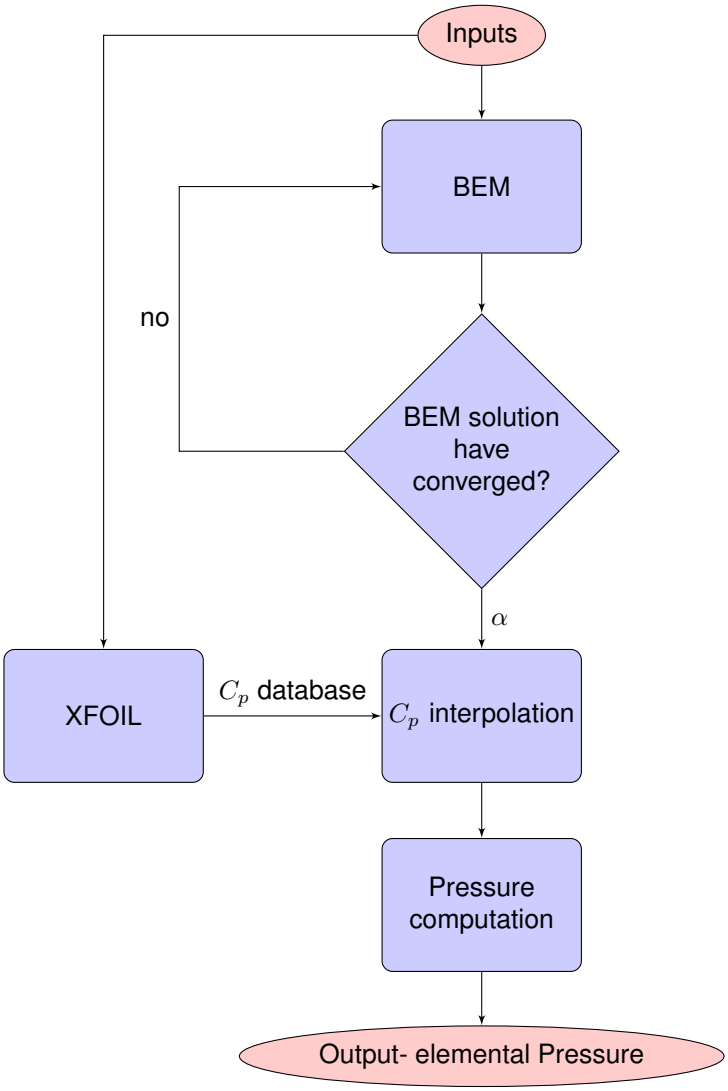

Figure 4.12: Fluxogram about aerodynamic model framework.

Chapter 5

Structural Model

5.1 Linear Elasticity Foundations

Any body subjected to a force and temperature field experiences a displacement field [39]. Applied loads, boundary conditions, temperature field and material stress law are necessary to determine a body displacement field. Corresponding stress and strains are interesting quantities to determine.

The x, y, z displacements can be computed is a displacement vector $\{u\}$, yielding

$$\{u\} = \{u\ v\ w\}. \tag{5.1}$$

The strain vector can have up to six independent components:

$$\{\varepsilon\} = \{\varepsilon_x\ \varepsilon_y\ \varepsilon_z\ \gamma_{xy}\ \gamma_{yz}\ \gamma_{zx}\}. \tag{5.2}$$

Thus, assuming small displacements, the strain vector $\{\varepsilon\}$ can be determined directly from the displacement vector as

$$\{\varepsilon\} = [D]\{u\}, \tag{5.3}$$

where [D] is the matrix differentiation operator given by [39]

$$[D_i] = \begin{bmatrix} \partial/\partial x & 0 & 0 \\ 0 & \partial/\partial y & 0 \\ 0 & 0 & \partial/\partial z \\ \partial/\partial y & \partial/\partial x & 0 \\ 0\ \partial/\partial z & \partial/\partial y & 0 \\ \partial/\partial z & 0 & \partial/\partial x \end{bmatrix}. \tag{5.4}$$

Similarly, the stress vector $\{\sigma\}$ has six diffferent components:

$$\{\sigma\} = \{\sigma_x\ \sigma_y\ \sigma_z\ \tau_{xy}\ \tau_{yz}\ \tau_{zx}\}. \tag{5.5}$$

From the Linear Elastic Theory results the Hook's Law [39], which relates simultaneously stress and strain components as

$$\{\sigma\} = [E](\{\varepsilon\} - \{\varepsilon^t\}), \tag{5.6}$$

with

$$\{\varepsilon_t\} = \{\delta T\ \delta T\ \delta T\ 0\ 0\ 0\}, \tag{5.7}$$

where $\{\varepsilon^t\}$ represents the part of strain due to temperature, δ is the coefficient of thermal expansion, T is the temperature. The term $\{\varepsilon\} - \{\varepsilon^t\}$ includes the elastic component of strain only. $[E]$ is the elastic matrix,

$$[E] = \begin{bmatrix} \lambda + 2\mu & \xi & \xi & 0 & 0 & 0 \\ \xi & \xi + 2\mu & \xi & 0 & 0 & 0 \\ \xi & \xi & \xi + 2\mu & 0 & 0 & 0 \\ 0 & 0 & 0 & \mu & 0 & 0 \\ 0 & 0 & 0 & 0 & \mu & 0 \\ 0 & 0 & 0 & 0 & 0 & \mu \end{bmatrix}, \tag{5.8}$$

where ξ and μ are constants depending on the elastic modulus E and the poisson ratio ν, given respectively by

$$\lambda = \frac{\nu E}{(1+\nu)(1-2\nu)} \tag{5.9}$$

and

$$\mu = \frac{E}{2(1+\nu)}. \tag{5.10}$$

5.2 Finite Element Matrix Formulation

The structural model implemented follows the linear finite element formulation applied to 4-node *shell* elements. They have six degrees of freedom per node, three translations and three rotations. This kind of element support a very large range of strain and rotation, dealing with linear and non-linear problems. Is also possible to model composite shells and sandwich forms, governed by first shear deformation [16].

Considering an arbitrary three dimensional nodal displacement vector,

$$\{q\} = \{u_1\ v_1\ w_1\ u_2\ v_2\ w_2 ...\}, \tag{5.11}$$

the finite element displacement is found by

$$\{u\} = [N]\{q\} \tag{5.12}$$

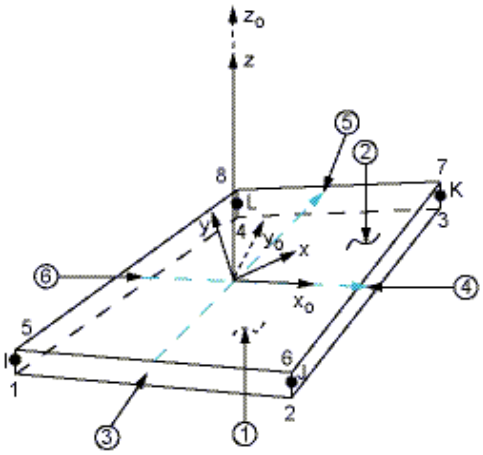

Figure 5.1: 4-nodded shell element [15].

.

where $[N]$ is the matrix that contains functions of form. The strains can also be obtained directly by

$$\{\varepsilon\} = [B]\{q\}, \tag{5.13}$$

where $[B]$ is called the displacement differentiation matrix and is expressed as

$$[B_i] = \begin{bmatrix} \partial N_i/\partial x & 0 & 0 \\ 0 & \partial N_i/\partial y & 0 \\ 0 & 0 & \partial N_i/\partial z \\ \partial N_i/\partial y & \partial N_i/\partial x & 0 \\ 0\ \partial N_i/\partial z & \partial N_i/\partial y & 0 \\ \partial N_i/\partial z & 0 & \partial N_i/\partial x \end{bmatrix}. \tag{5.14}$$

The solution of finite elements seek to find the minimum total potencial energy Π [39]

$$\Pi = \frac{\partial}{\partial q}\left(\int_V \frac{1}{2}\{\varepsilon^e\}^T\{\sigma\}dv - \int_V \{u\}^T p^V dV - \int_S \{u\}^T\{p^S\}dS\right) \tag{5.15}$$

Computing the strains and stress relations and substituting in equation (5.15) yields

$$\Pi = \left(\int_V \frac{1}{2}\left([B]\{q\} - \{\varepsilon^t\}\right)^T [E]\left([B]\{q\} - \{\varepsilon^t\}\right) dV - \int_V \left([N]\{q\}^T\right)\{p^V\}dV - \int_S \left([N]\{q\}^T\right)\{p^S\}dS\right) \tag{5.16}$$

The differentiation relative to nodal displacement q, yields

$$\int_V [B]^T[E][B]dV\{q\} - \int_V [B][E]\{\varepsilon^t\}dV - \int_V [N]^T\{p^V\}\int_S [N]^T\{p^S\}dS = 0 \tag{5.17}$$

Each integral has a significant meaning:

$$[k] = \int_V [B]^T [E][B] dV \{q\} \tag{5.18}$$

$$\{p\} = \int_V [B][E]\{\varepsilon^t\} dV + \int_S [N]^T \{p^S\} dS \tag{5.19}$$

$$\{h\} = \int_V [N]^T \{p^V\} = 0 \tag{5.20}$$

Where $[k]$ is called the *element stifness matrix*, $\{f\}$ is the *load vector* and $\{h\}$ is the *thermal vector*, modelling forces originated by thermal expansion.

Usually, for one element it is applied the following notation:

$$[k]\{q\} = \{f\}, \tag{5.21}$$

$$\{f\} = \{p\} + \{h\}. \tag{5.22}$$

Once obtained all element equations, it is necessary to assemble them in one single system of equations to reach the final solution. Therefore, the global system of equations is

$$[K^G]\{Q^G\} = \{F^G\}, \tag{5.23}$$

and the total minimum potential energy is simply the sum of element potential energies:

$$\Pi^G = \sum_{i=1}^{num.\ elem} \Pi_i. \tag{5.24}$$

5.3 Composite materials

Composite materials combine two or more materials on a macroscopic scale to achieve better properties than the conventional materials, for instance, stiffness, strength, weight reduction, corrosion resistance, thermal properties and fatigue life [16]. Most part of composite materials are made from two materials: a reinforcement material called *fibre* and a base material, called *matrix*. There are various types of composites materials, but one is interested in one in special: *laminated composites*. They are made of layers of different material, and the fibres and matrix can be either metallic or non-metallic [16]. A *ply* is a typical sheet of composite material. A *laminate* is a set of plies, stacked to achieve the desired stiffness and thickness. For example, unidirectional plies can be stacked, so that the fibres in each ply are oriented in the same or different directions, as shown in figure 5.2. The sequence of several orientations of a composite layer in a laminate is known as *stacking sequence*.

The micromechanics field developed a set of equations that allow the determination of the elastic constants of a composite material, assuming [16]:

- Perfect bonding between fibres and matrix;
- Fibres are parallel, and uniformly distributed;

- The matrix is free of voids or micro-cracks, and initially is in a stress-free state;
- Both fibres and matrix are isotropic and obey Hooke's law;
- The applied loads are either parallel or perpendicular to the fibre direction

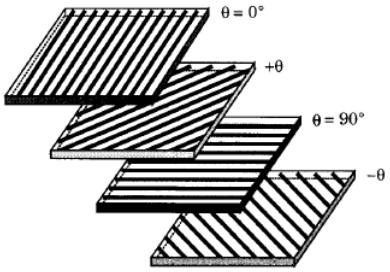

Figure 5.2: A stack with various unidirectional layers [16].

The constants of a lamina are given by

$$E_{11} = E_f V_f + E_m(1 - V_f), \tag{5.25}$$

$$E_{22} = \frac{E_f E_m}{E_f(1 - Vf) + E_m V_f}, \tag{5.26}$$

$$\nu_{12} = \nu_f V_f + \nu_m(1 - V_f), \tag{5.27}$$

$$G_{12} = \frac{G_f G_m}{G_f(1 - V_f) + G_m V_f} \tag{5.28}$$

where E_{11} is the longitudinal modulus, E_{22} is the transversal modulus E_f is the fibre modulus, E_m is the matrix modulus, V_f and is the fibre volume fraction, ν_m is the matrix Poisson's ratio, ν_f is the fibre Poisson's ratio, ν_{12} is the major Poisson's ratio and G_{12} is the shear modulus. Matrix and fibre shear modulus, G_m and G_f, respectively, are given by

$$G_m = \frac{E_m}{2(1 + \nu_m)}, \tag{5.29}$$

$$G_f = E_f 2(1 - \nu_f). \tag{5.30}$$

5.4 Description of Structural Mesh Generator *WTB_struct_model.m*

5.4.1 Purposes and Objectives

The numerical code developed in $MATLAB^{®}$ builds from a set of inputs defined by the user, a structured [1] mesh of a wind turbine blade. An output file with *APDL* code is created and computed in the

[1]The elements of a structured mesh can be all indexed by three index variables i, j, k, whereas in an unstructured mesh, the connectivity between the elements is not express in such simple manner. The connectivity between elements must be explicitly stored, therefore usually the storage requirements and computation times are more demanding [40].

FEM tool $ANSYS^{®}$ that performs a static simulation and gives an insight about the structural response of the structure.

5.4.2 Input Variables

The initial inputs necessary to compute the mesh are the number of divisions of blade chord, span and webs. Additionally, the user may change the web position (in percentage of chord). Furthermore, all coordinates concerning airfoil sections should be computed in percentage of chord and located in a *.txt* file.

5.4.3 Nodes Assembly

The first action taken by $MATLAB^{®}$ is compute the blade sections. The code reads the airfoil coordinate files and draws them like is illustrated in figure 5.3.

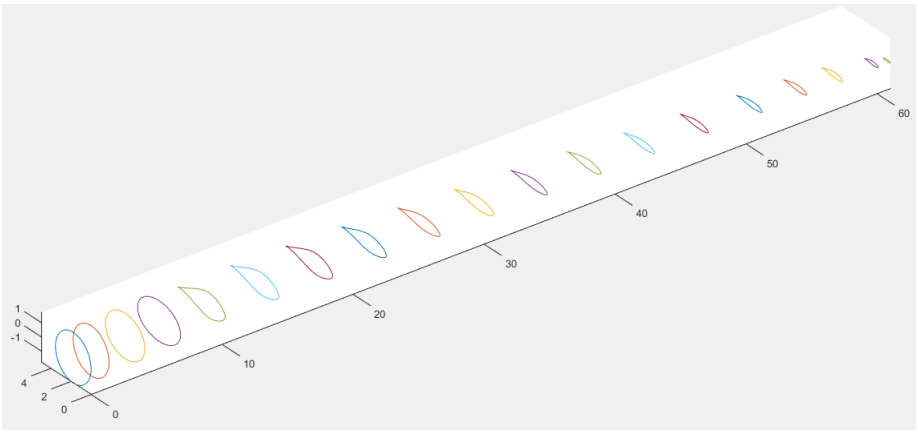

Figure 5.3: Airfoil section computation.

The amount of data collected to build the blade geometry assumes a special relevance, namely about the number of airfoil sections collected to build it. The accuracy in the interpolation is improved if more sections are loaded previously, otherwise trailing edge position can suffer significant deviations. Identically, it is also important to have a sufficiently large number of points in each section, as that may affect negatively the interpolation of intermediate chord coordinates.

Nevertheless, the user has the freedom to choose the number of divisions in chord, span and webs, then from the set of computed airfoil sections, all nodes are generated by linear interpolations of two neighbour sections. A blade nodal representation is illustrated in figure 5.4.

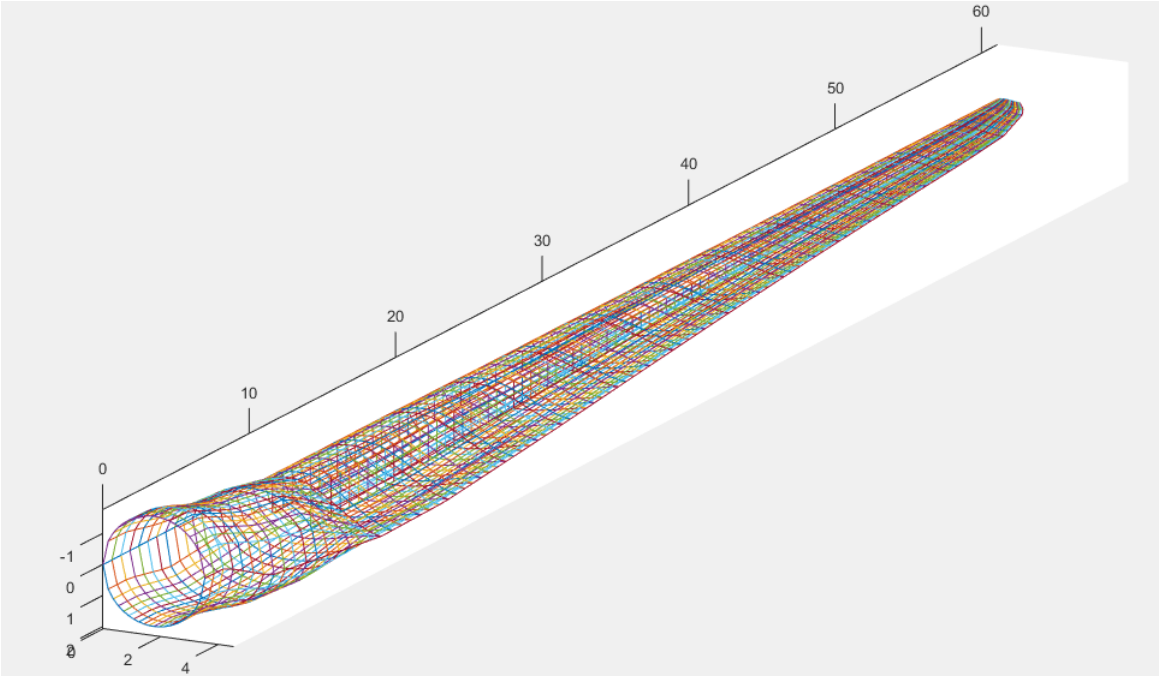

Figure 5.4: Mesh example.

5.4.4 Elements Assembly

Following the nodes data, $ANSYS^{®}$ needs to know which are the nodes that form each finite element. Therefore, a routine to assemble all the elements was developed. The element chosen was *SHELL181*, that is the one most suitable to shell structures [15]. It is constituted by four nodes, so starting in the leading edge of root section in suction side, a sweep is done towards trailing edge to compute a line of elements:

$$e_1^{(k)} = mesh(i, j), \tag{5.31}$$

$$e_2^{(k)} = mesh(i+1, j), \tag{5.32}$$

$$e_3^{(k)} = mesh(i+1, j+1), \tag{5.33}$$

$$e_4^{(k)} = mesh(i+1, j+1), \tag{5.34}$$

where an element k is computed by the four nodes (e_1, e_2, e_3, e_4) in the vicinity, in the anti-clockwise direction. The direction in which the nodes are computed is not arbitrary, since the unitary normal vector in $ANSYS^{®}$ follows the right hand rule, this way the routine implemented guarantees that it is always pointing toward the posite Y-axis. That fact is determinant to apply surface loads, once a positive pressure load is applied in the opposite direction of the element unitary normal vector. Furthermore, in case of using composite materials, the stack sequence is oriented according the orientation of this vector. As soon as the sweep towards trailing edge is done, an increment in span coordinate is done and the same routine is applied two times the number of span divisions defined by the user. The total

number of elements covering the blade surface is then, two times the product between the divisions in chord and span. The same set of routines is applied to compute the webs elements.

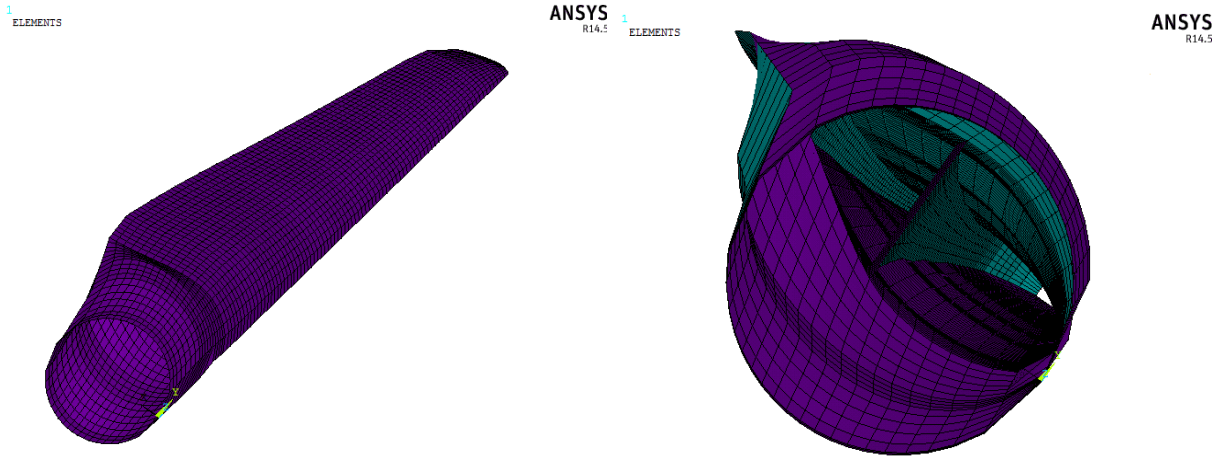

(a) Blade surface. [7]

(b) Shear webs. structure

Figure 5.5: Assembled elements.

5.5 Load and Nodal Constraints Computation

It was considered that blade is fully constrained in its root, therefore no nodal displacements nor rotations are allowed there. The load is computed in each element surface from an APDL code computed by $MATLAB^{®}$ (see full APDL code in appendix B.1), then $ANSYS^{®}$ calculate the respective force to apply in each mesh node.

Chapter 6

Fluid-Structure Interaction

Until now, aerodynamic and structural analyses have being treated separately. These two distinct fields have different domains, however, they share boundaries and, in fact, a well defined region exists where the information between both domains can be exchanged. In that region, a three-dimensional surface, a structural-field interface is defined [41]. On one side, the structural mesh undergoes a displacement field, that constantly induces changes in the fluid domain, since by definition this fluid must occupy all space available and fulfil all gaps that might exist due to deformations of the structural mesh. On the other side, the fluid mesh is sensitive to variations in fluid stress, namely due to pressure and shear, that will transmit through the interaction surface by means of external load to the structural domain. Thus, a clear reciprocity is made here, and it makes all sense to couple both models and study the simultaneous aerodynamic and structural response, as schematically shown in figure 6.1.

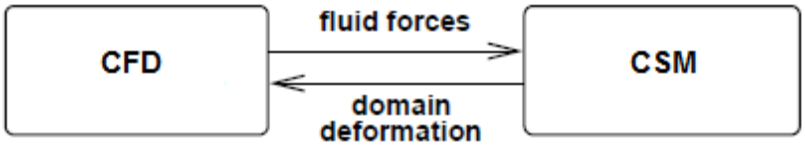

Figure 6.1: Exchange domain between aerodynamic and structural models.

The main concern about this topic lies on the correct definition of both mesh boundaries, since it is not feasible in many situations to represent accordingly the interaction surface. In these cases, questionable situations appear and it is the competence of the engineer to make the coupled system work properly and understand ambiguous situations to maintain a valid transfer between displacement and forces.

6.1 Fluid Structure Interaction Methods

In the technical literature three major techniques of fluid-structure interaction (FSI) are presented, where the main differences lie the on sequence to solve both aerodynamic and structural models. The computational most demanding technique is the fully coupled method, where both aerodynamic and structural

models are solved simultaneously in one single module, which causes convergence issues, whereby the most part of problem that include fully-coupled equations are resumed to two dimensions, due to clear limitations in grid size [42], [43].

The closely coupled model is the most common model in FSI solvers because it presents good accuracy in non-linear problems. Aerodynamic and structural models are solved independently and then coupled in one interface module. The aerodynamic load is mapped on the structure, the structural displacement is transferred to the fluid solver and a new aerodynamic should be coupled in the a deformed structural mesh of the previous iteration [44].

The last model is known as loose coupling and both aerodynamic and structural model are solved independently until convergence, and the information is exchanged just after that. Obviously, this method loses accuracy in comparison to others because the information until convergence is completely lost. However, it might be enough in small perturbation problems.

The figure 6.2 shows the relation between programming effort and coupling level of each method.

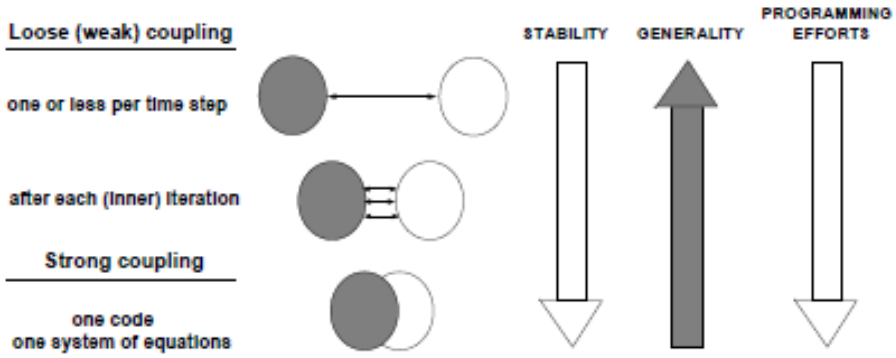

Figure 6.2: FSI coupling level [17].

6.2 Loose Coupling FSI Schemes

The critical point of fluid structure interaction is the transfer of information between aerodynamic and structural grids, in particular, transfer the aerodynamic load to the structural grid and the displacement to the aerodynamic grid. The main criterion that should be guaranteed is that both aerodynamic and structural meshes are flawlessly connected,

$$\{u_{s_k}\} = \{u_{a_k}\}, \tag{6.1}$$

where u_{s_k} is the position vector of an arbitrary node of the structural grid and u_{s_k} is the similar regarding the aerodynamic grid.

The structural solver should be able to solve the equation of motion

$$[M]\{\ddot{q}\} + [G]\{\dot{q}\} + [K]\{q\} = \{F\}, \tag{6.2}$$

where $[M]$, $[G]$, and $[K]$ are the mass, gyroscopic and stiffness matrices. $\{F\}$ is the force vector and $\{q\}$ is the displacement vector. Under steady axial flow conditions, the blade has a constant aerodynamic load and the equation of motion resumes to equation 5.23. Vector $\{F\}$ contains forces from different natures:

$$\{F\} = \{F_0\} + \{F_g\} + \{F_{aero}\} + \{F_{n.l.}\} \tag{6.3}$$

where $\{F_0\}$ is the constant force, $\{F_g\}$ is the gravitational load, $\{F_{aero}\}$ is the aerodynamic load and $\{F_{n.l.}\}$ is the non-linear component. Let us assume that the unique constant force is $\{F_{aero}\}$, and neglect $\{F_{n.l.}\}$ and $\{F_g\}$. The static equilibrium is given by

$$[K]\{q\} = \{F_{aero}\}, \tag{6.4}$$

which has the same meaning of equation (5.21). F_{aero} is obtained from the aerodynamic module.

Dong Ok Yu and Oh Joon Kwon [18] presented in their research two different loose coupling methods of FSI. The first method consists on a static FSI model running in sequence the structural and aerodynamic model, the latter on a CFD tool basis. The structural mesh is initially undeformed and the CFD tool calculates the aerodynamic load for the undeformed structure.

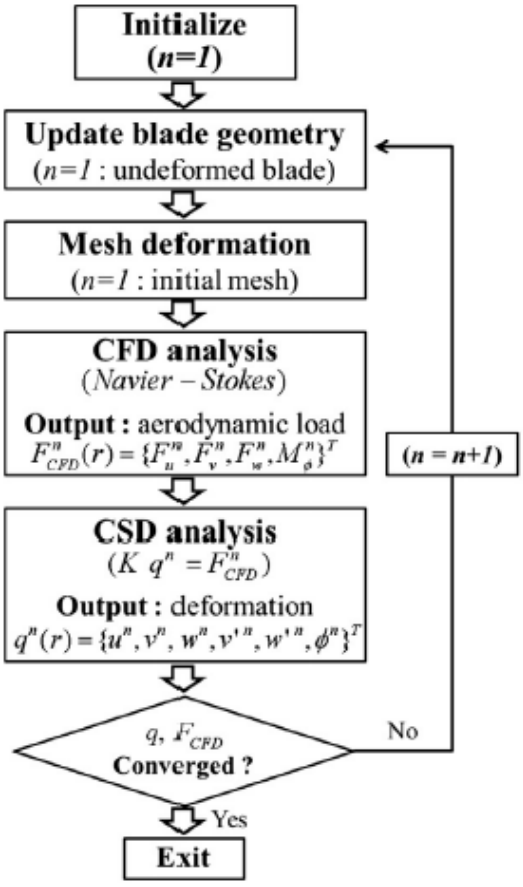

Figure 6.3: Static loose coupling FSI model [18].

Then, the output of the CFD solver is coupled to the FEM tool, that will apply the aerodynamic load on the deformed mesh and give a new output relatively to an updated deformed mesh, which will be introduced again in CFD solver. The iterative process is repeated until the convergence of $\{F_{aero}\}$ and displacement vector $\{q\}$ have been verified. The computation sequence is shown in figure 6.3. The second method is more suited to unsteady loads and time-varying response, avoiding more demanding methods as fully-coupled ones. In the first iteration, $\{F_{aero}\}$ is computed by a BEM code and the displacement field is calculated in relation to the undeformed mesh. In its turn, the CFD solver receives the deformed mesh, and performs the aerodynamic load calculation, regarding the deformed mesh, and returns it to the CSM solver. This time, the total aerodynamic load in the current iteration k is given by the CFD solution and the difference between current and previous BEM solutions as

$$\{F^k_{aero}\} = \{F^k_{CFD}\} + (\{F^k_{BEM}\} - \{F^{k-1}_{BEM}\}). \tag{6.5}$$

With this method the convergence only depends on the force.

6.3 Simplified Coupling Procedure

The last step of numerical development in the scope of this research was focused on a loose coupling FSI model. Usually these models incorporate a CFD solver to determine the aerodynamic load which is interacting with the structure. In this work, it is exaggerated to make that statement but, even so, it was developed a simplified aerodynamic model which can estimate the aerodynamic load. Since the objective of this work is to observe a mitigation in load due to the bend-twist coupling (BTC), in this model only twist is coupled, whereas in a conventional FSI coupling model, both displacements and rotations are returned to CFD solver. Thus, the load mitigation will be achieved exclusively by the variation in twist.

The coupling initiates with the structural model. The aerodynamic load is treated in $ANSYS^{®}$ as a pressure load on the elements, and both aerodynamic and structural meshes are coincident, as is illustrated in figure 6.4.

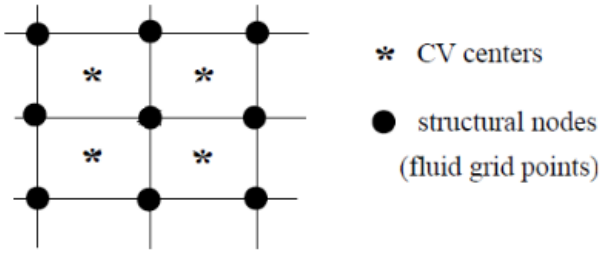

Figure 6.4: Sobreposition between aerodynamic and structural grid [17].

$ANSYS^{®}$ simulation consists in a steady static analysis of the structure and the nodal displacement field is returned to $MATLAB^{®}$. From the nodal displacements is possible infer about the amount of twist that the blade is subjected. The correct calculation of twist would be calculating β in relation to the

elastic axis, however it is not possible to determine precisely where it is located. Therefore this angle is calculated taking into account the displacement of leading and trailing edges in each span coordinate:

$$\beta_i = arctan\left(\frac{y_{i_{t.e.}} - y_{i_{l.e.}}}{x_{i_{t.e.}} - x_{i_{l.e.}}}\right). \tag{6.6}$$

where $y_{i_{l.e.}}$ is the y position of the leading edge, $y_{i_{t.e.}}$, is the y position of the trailing edge. The same notation is applied to $x_{i_{l.e.}}$ and $x_{i_{t.e.}}$.

β_i is the variable updated in BEM solver, which initially is set to zero and will make the aerodynamic load change in each iteration. The updated F_{aero} is then introduced in $MATLAB^{®}$ and the iterative process is consecutively executed until F_{aero} converges. Theoretically, the computation times should not be exaggerated, since non linear effects are not being considered during the simulations.

The generic coupling sequence is represented in figure 6.5 and it shows the framework of all numerical models developed during the course of this work.

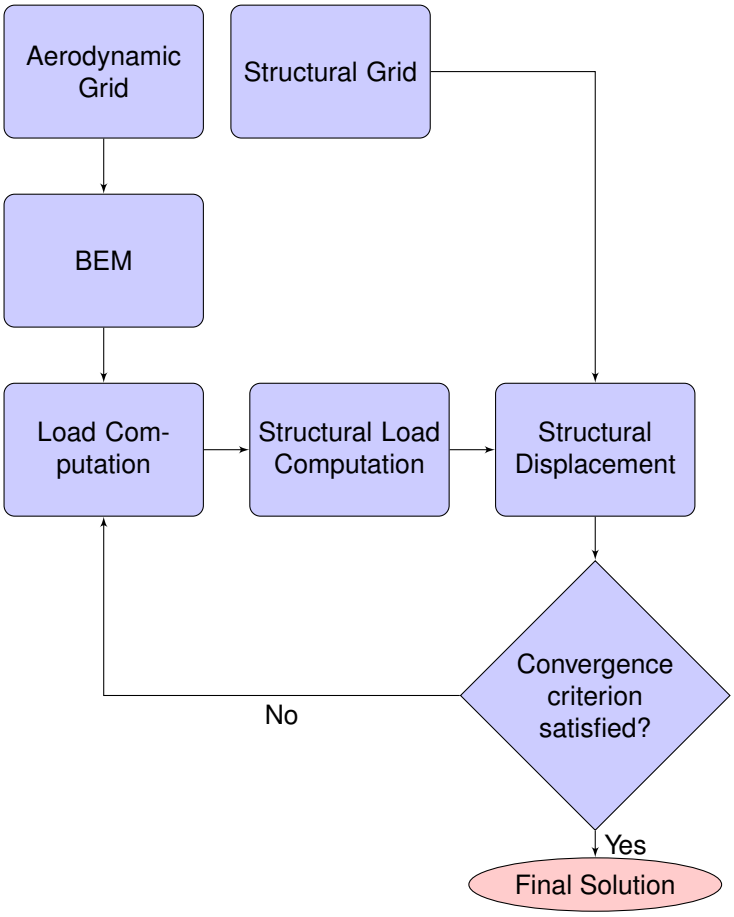

Figure 6.5: Fluid-structure interaction iterative solution.

Chapter 7

Parametric Study

In this chapter will be introduced a baseline configuration that will serve as comparison to perform a parametric study. It will be computed and analysed four different and independent parameters: fibres laminate orientation, thickness distribution, shear webs number and location and material reinforcement. The results of each study will be discussed and summarized in the end.

7.1 Wind Turbine NREL 5 MW Data

The computational model developed in the present work has been used to characterize both the aerodynamic and structural performance of a wind turbine blade. The blade under test is part of a quite common wind turbine in offshore applications developed by the National Renewable Energy Laboratory, NREL [45]. This USA entity intended to gather more knowledge to build sites in american deep waters and worldwide. From the experience of other companies, it was concluded that a wind turbine becomes cost-effective on an offshore application when the output power is between 5 and 20 MW. A baseline 5 MW wind turbine was chosen, since there are several publications about this conceptual design, and the largest wind turbine prototypes in 2009 had this rating [45]. Table 7.1 presents the wind turbine baseline properties.

The blade is constituted by a mixture of TU Delft and NACA airfoil shapes, while the root region contains circular sections. The transition region is not clearly documented. In table 7.2 it is possible to consult the different airfoils used in the NREL 5MW blade. It was not possible to find any data about TU Delft airfoils, and they were replaced by identical airfoils from NACA series, as shown in table 7.3. The location of maximum thickness and camber were maintained equal to the values used in tip airfoil.

It was collected additional geometrical data to develop the blade geometry, listed in table 7.4.

Rating	5 MW
Rotor orientation, configuration	Upwind, 3 blades
Control	Variable speed, collective pitch
Drivetrain	High speed, multiple-stage gearbox
Rotor, hub diameter	126 m, 3 m
Hub-height	90 m
Cut-in, rated, cut-out wind speed	3 m/s, 11.4 m/s, 25 m/s
Cut-in, rated rotor speed	6.9 rpm, 12.1 rpm
Rated tip-speed	80 m/s
Overhang, Shaft tilt, pre-cone	5 m, 5°, 2.5°
Rotor mass	110,000 kg
Nacelle mass	240,000 kg
Tower mass	347,460 kg
Coordinate location of overall CM	(-0.2 m, 0.0 m, 64.0 m)

Table 7.1: NREL MW wind turbine specifications [1].

Airfoil	Thickness $[\%t/c]$	Initial span position z $[m]$)	Airfoil ID
Cylinder 1	100	1.8	1
Cylinder 2	100	5.98	2
DU W-405	40.5	10.15	3
DU 97 W-300	35.09	15.00	4
DU 91 W2-250	30	20.49	5
DU 91-W2-250	25	26.79	6
DU 91 W-210	21	34.22	7
NACA 64-618	18	42.47	8

Table 7.2: NREL 5MW wind turbine blade airfoils [1].

NACA Airfoil	Thickness $[\%t/c]$	Location of maximum thickness $[\%t/c]$	Camber $[\%t/C]$	Airfoil ID
64-641	40	40	60	3
64-630	30	40	60	4
64-625	25	40	60	5
64-621	21	40	60	6

Table 7.3: Modified airfoil sections.

7.2 Baseline Blade Parameters

Regarding the material properties, it was implemented a mixture between glass fibre and epoxy [2] . Properties of both materials are listed in table 7.5.

The mixture of both materials is commonly known as E-glass/epoxy, which is quite frequent in wind turbines applications, whose mechanical properties are available in table 7.6.

Combining data from tables 7.5 and 7.6, it is possible to estimate the fraction in volume of each material, applying equation (5.25). The estimated value of fibre volume is $V_f \approx 59\%$. This way, it is possible to infer about the composite tensile and compressive strengths.

The composite yield strength, σ_y was not found, but it is also possible to have a reference value. This parameter is quite relevant in the design stage, because the blade should not be subjected in

[2]Epoxy is a resin with excellent mechanical, thermal, and chemical properties, making it widely used in high performance applications. It provide low shrinkage, and high adhesive strength. Furthermore, it is very resistant to corrosion and other chemical reactions [46], [47].

Span position z $[m]$	Twist°	Chord Length $[m]$	Airfoil ID
2.8667	13.31	3.54	1
5.6	13.31	3.85	1
8.33	13.31	4.17	2
11.75	13.31	4.56	3
15.85	11.48	4.65	4
19.95	10.16	4.46	4
24.05	9.01	4.25	5
28.15	7.80	4.01	6
32.25	6.54	3.75	6
36.35	5.36	3.50	7
40.45	4.19	3.26	7
44.55	3.13	3.01	8
48.65	2.32	2.76	8
52.75	1.53	2.52	8
56.17	0.86	2.31	8
58.17	0.86	2.31	8
58.90	0.37	2.09	8
61.63	0.11	1.42	8

Table 7.4: Blade geometrical data [2].

	Glass fibre	Epoxy
Density ρ $[Kg/m^3]$	2550	1110
Tensile modulus E $[GPa]$	70	5
Tensile strength σ_{ut} $[MPa]$	3510	80
Poisson ratio ν	0.2	0.4
Compressive strength σ_{uc} $[MPa]$	910	133
Yield strength σ_y $[MPa]$	—	20.4

Table 7.5: Mechanical properties of fibre glass and epoxy [3], [4].

Density ρ $[kg/m^3]$	1920
Longitudinal modulus E_{11} $[GPa]$	43.2
Transversal modulus E_{22} $[GPa]$	12.6
Poisson coefficient ν	0.38
Distortion modulus G $[GPa]$	4.2

Table 7.6: E-glass/Epoxy composite mechanical properties [5].

any moment to a stress near this value. The composite yield strength is the stress indexed to the first material constituting the composite laminate, achieving plastic deformations. In general, the matrix Young's modulus is inferior than the fibres, thus it is the first achieving the plastic regime. Therefore, the composite's yield strength is given by [48]

$$\sigma_{y_c} = E_{11}\frac{\sigma_{y_m}}{E_m} \approx 176.6\ MPa. \tag{7.1}$$

The baseline configuration contains laminates with constant thickness, 8 layers oriented in the blade plane, +45 degrees in relation to the edgewise axis. Figure 7.1, it is plotted the laminate stack.

The free-stream wind velocity was set to 25 m/s, equal to catalogued rotor cut-out speed, and crosses the blades from the leading to the trailing edge, as usual. Figure 7.2 illustrates the surface load applied

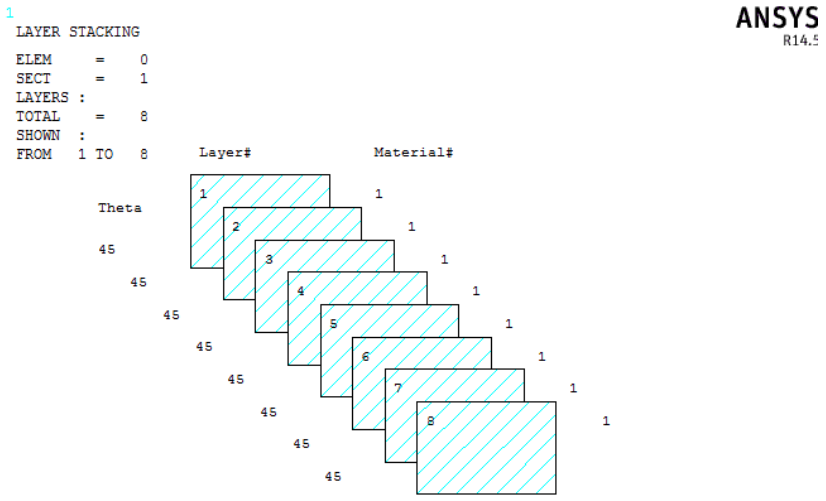

Figure 7.1: Fibres orientation.

on the blade at the suction and pressure sides.

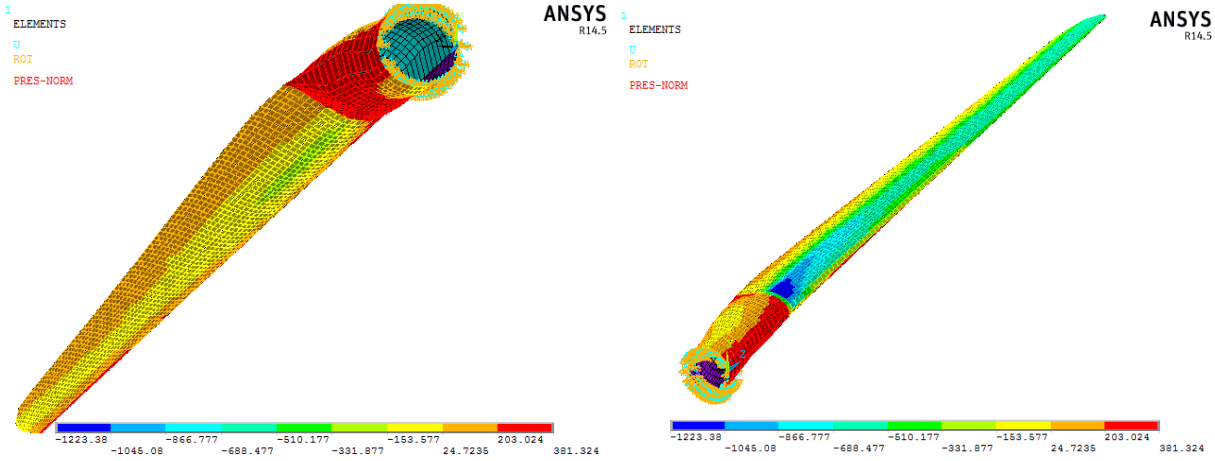

(a) Lower surface.

(b) Upper surface.

Figure 7.2: Pressure distribution on blade surface.

The suction pressure is concentrated in the thicker airfoils region of upper surface, whereas high pressure is distributed by all blade lower surface. In the leading edge, the stagnation points are concentrated, which means, velocity tends to zero and high pressure peaks are formed.

Furthermore, it was considered an initial position of shear webs at 45% and 75% of chord. The simulations performed in the parametric study did not couple the effective blade twist due to the amount of time that would be spent to study each parameter. At this stage, it is more important to understand how each parameter affect the structural response and, one iteration is enough to trace this trend. A structural mesh with a total of 4770 elements was computed, 4000 elements model the skin surface, the remaining elements model shear webs.

7.3 Baseline Results

7.3.1 Structural Performance

The structural analysis shows expected trends in the results, as both edgewise and flapwise displacements continuously increase towards blade tip (in absolute values). The shear webs deformation, in figure 7.3(b) follows the same pattern of the exterior surface, in figure 7.3(a).

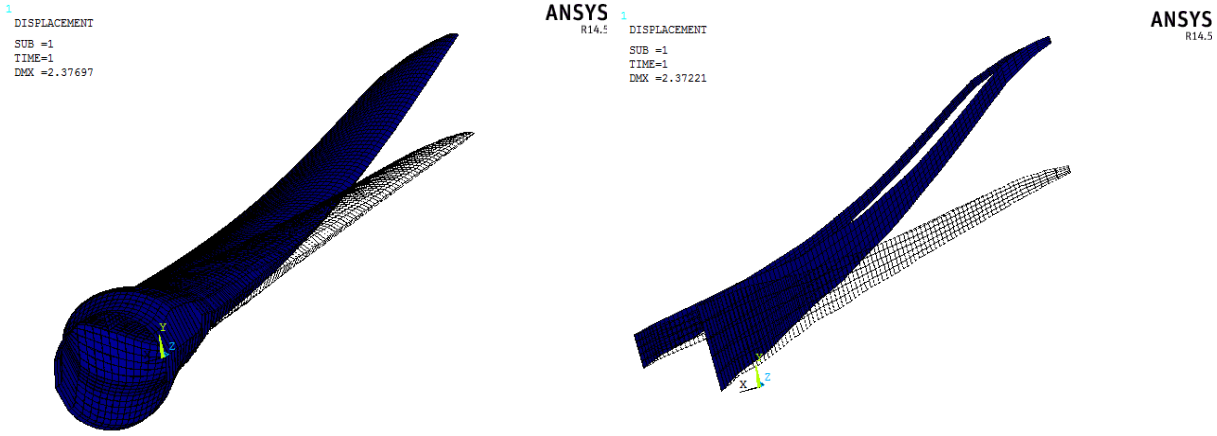

(a) Blade surface (b) Webs

Figure 7.3: Baseline deformation.

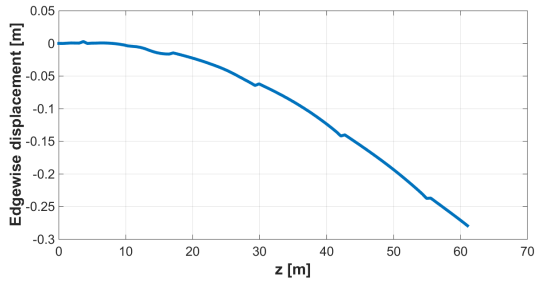

(a) Edgewise displacement at $(x/c) = 25\%$

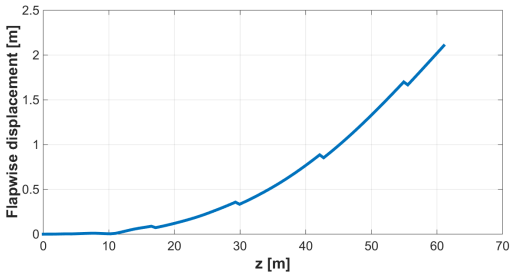

(b) Flapwise displacement at $(x/c) = 25\%$

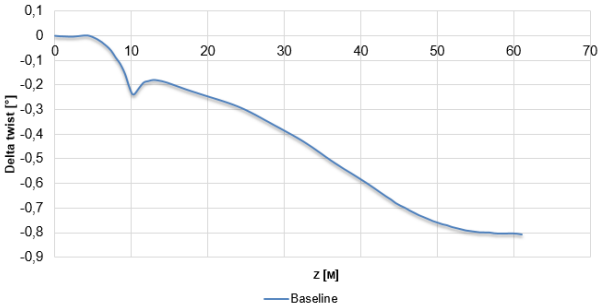

(c) Twist distribution

Figure 7.4: Baseline displacement and twist distribution.

With respect to twist in figure 7.4(c), it starts a pronounced curve until $10\ m$, that is slightly attenuated by the presence of shear webs since then. The general trend is increase of twist through the span, which is exactly the opposite desired behaviour. This situation would conduct to a situation of an increase of blade angle of attack until it gets stalled. The following section will explain more in detail this question through two contrasting situations. The sudden change in twist reported previously, is the major source of stress, as shown in figure 7.5, as the maximum is obtained in the same span position illustrated by 7.4(c). An enhanced configuration should take into account an eventual overstress in this region. Nevertheless, by now, absolute values fulfil the von Mises failure criterion (that is presented in Appendix A.1), as confirmed in table 7.7.

Layers θ [°]	$y_{max}\ [m]$	$x_{max}\ [m]$	$\lvert\beta_{max}\rvert$ [°]	$\sigma_{eqv,max}\ [MPa]$
$+45$	2.36	-0.31	$-0,80$	29.8

Table 7.7: Baseline maximum values.

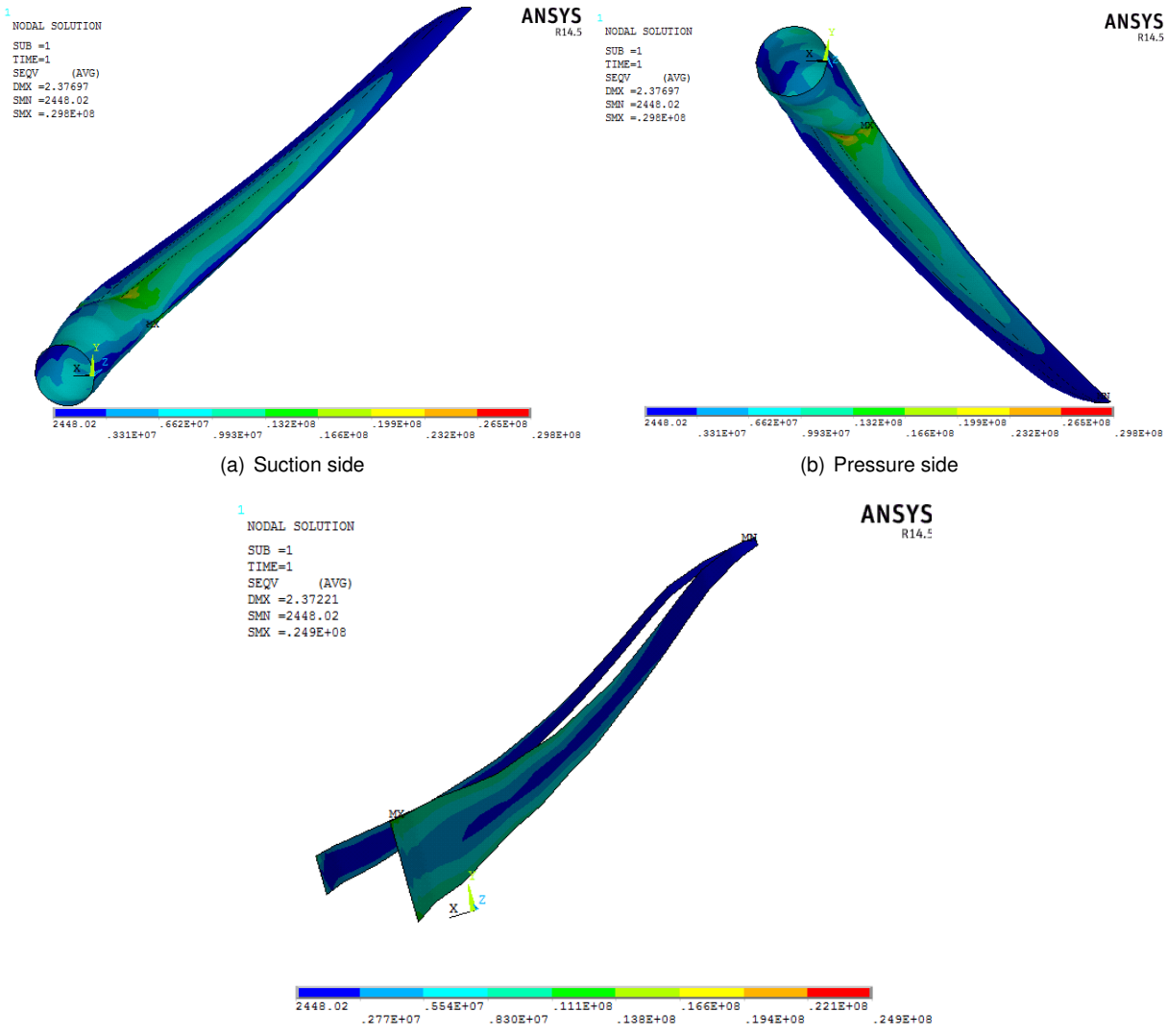

(a) Suction side

(b) Pressure side

(c) Webs

Figure 7.5: Baseline von Mises equivalent stress.

7.3.2 Aerodynamic Performance

The aerodynamic performance was evaluated from the estimation of lift and power coefficients. The latter was estimated ignoring drag coefficient, otherwise it would be necessary an improved numerical model to estimate it as function either of lift coefficient or angle of attack.

It can be demonstrated that power in a blade portion is given by [9]

$$dP = \frac{1}{2}\rho A U^3 \left[\frac{8}{\lambda} a'(1-a)\lambda_z^3 d\lambda_z\right], \tag{7.2}$$

thus, the power coefficient in a blade element (assuming blade is only discretized in the spanwise direction) is obtained by the integration of P along the element:

$$C_p = \frac{8}{\lambda}\int_{z_1}^{z_2} a'(1-a)\lambda_z^3 d\lambda_z. \tag{7.3}$$

The results of C_P, shown in figure 7.6(a), are computed applying equation (7.3), in the region covered by BEM, that does not include the root section (approximately 10m).

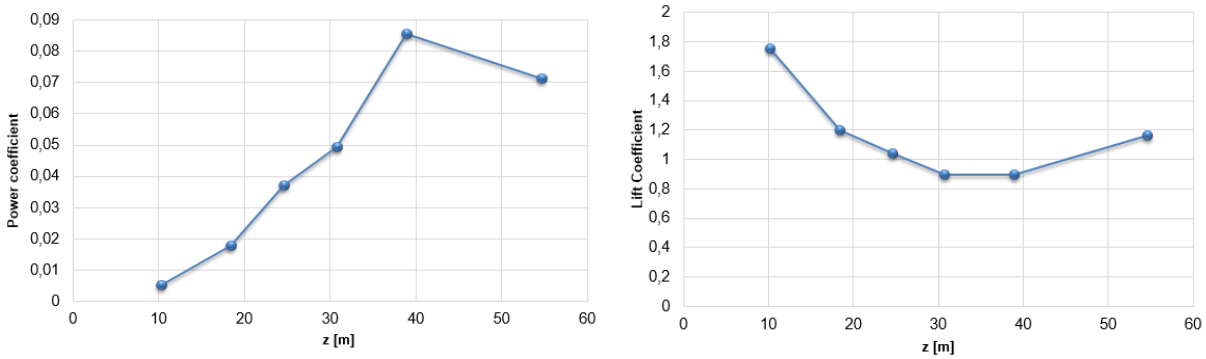

(a) Power coefficient distribution

(b) Lift coefficient distribution

Figure 7.6: Baseline aerodynamic performance.

The lift coefficient presented in 7.6(b), is directly computed in the BEM routine, by the interpolation of the reference airfoil $C_l \; vs. \; \alpha$ at the operational angle of attack. The C_l curve shows a maximum at the beginning of airfoil region, coincident with thicker sections, where the slope $\frac{\partial C_l}{\partial \alpha}$ is higher (see Appendix A.2), and according the suction pressures observed in figure 7.2(b). The power coefficient is a function of tip speed ratio, which is directly proportional to the blade span position. That trend is slightly visible in figure 7.6(a).

7.4 Fibres Orientation

The fibres orientation study was initially performed through a variation of all fibres, including webs. Three distinct angles, 0°,90° and -45° were chosen. Then, the skin fibres orientation was kept fixed, and the webs fibres orientation was changed, to observe their influence in the global response. Finally, following the procedures of other works [5], [10], two unbalanced stack configurations were built up, contrasted

with a balanced stack. The table 7.9 describe the stack employed in multi-directional laminates.

The recorded results in figures 7.7 to 7.10, evidence in first place that, the layers orientation can affect significantly the results, therefore the choice criterion should be thorough.

Skin θ [°]	Webs θ [°]	y_{max} $[m]$	x_{max} $[m]$	$\lvert\beta_{max}\rvert$ [°]	$\sigma_{eqv,max}$ $[MPa]$
0	0	2.26	-0.30	-0.17	31.9
-45	-45	2.31	-0.31	0.73	35.9
90	90	0.77	-0.12	-0.15	27.0
$+45$	0	2.36	-0.31	-0.8	30.6
$+45$	-45	2.36	-0.31	-0.8	31.8
$+45$	90	2.08	-0.28	-0.69	38.5
Balanced	Balanced	1.08	-0.14	-0.15	38.2
Unbalanced 1	Unbalanced 1	1.10	-0.15	-0.18	39.0
Unbalanced 2	Unbalanced 2	1.09	-0.15	-0.14	37.6

Table 7.8: Layers orientation; maximum values.

Laminate Label	Skin θ [°]	Webs θ [°]
Balanced	$[90_2\lvert 25\lvert 45\rvert -45\rvert -25\rvert 90_2]$	$[90_2\lvert 25\lvert 45\rvert -45\rvert -25\rvert 90_2]$
Unbalanced 1	$[90_2\lvert 25\lvert 45]_S$	$[90_2\lvert 25\lvert 45]_S$
Unbalanced 2	$[90_2\lvert -25\rvert -45]_S$	$[90_2\lvert -25\rvert -45]_S$

Table 7.9: Multi-directional Laminates stack.

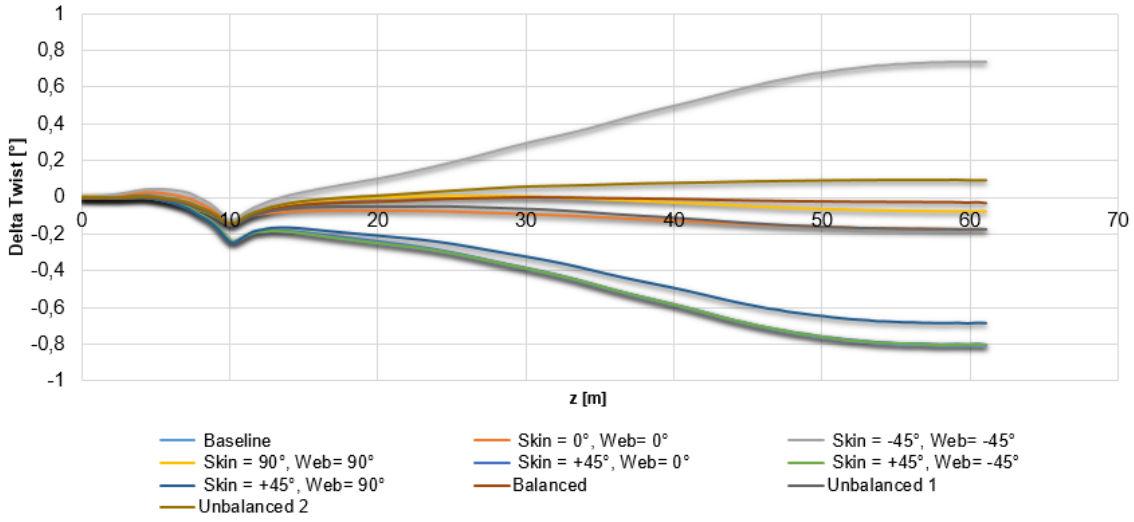

Figure 7.7: Twist distribution for different fibres orientation.

The stacks with unidirectional fibres proved to be very ineffective either in the amount of deformation caused or in the induced twist, presented in table 7.8. This table shows the maximum values, regarding both the flapwise and edgewise displacement (not necessarily at $(x/c) = 25\%$), twist and stress. Nevertheless, it should be noted that fibres oriented -45° +45°, despite the high nodal displacement, bring great benefits in the induced twist in comparison with baseline results, but only the -45° fibres induce a positive $\Delta\beta$, i.e., a reduction in angle of attack. The definitions of β in equation (6.6), and α in equation (4.26), state that only a positive $\Delta\beta$, calculated by equation (6.6) can generate a reduction in angle of

attack. The response verified by the variation in webs layers orientation is not very different from the unidirectional stack response.

The introduction of layers in different direction, yielding a multi-directional stack provided significant savings in maximum displacement, illustrated in figures 7.9 and 7.8, but did not produce desired effect in twist, as a negative $\Delta\beta$ result in an increase of the angle of attack.

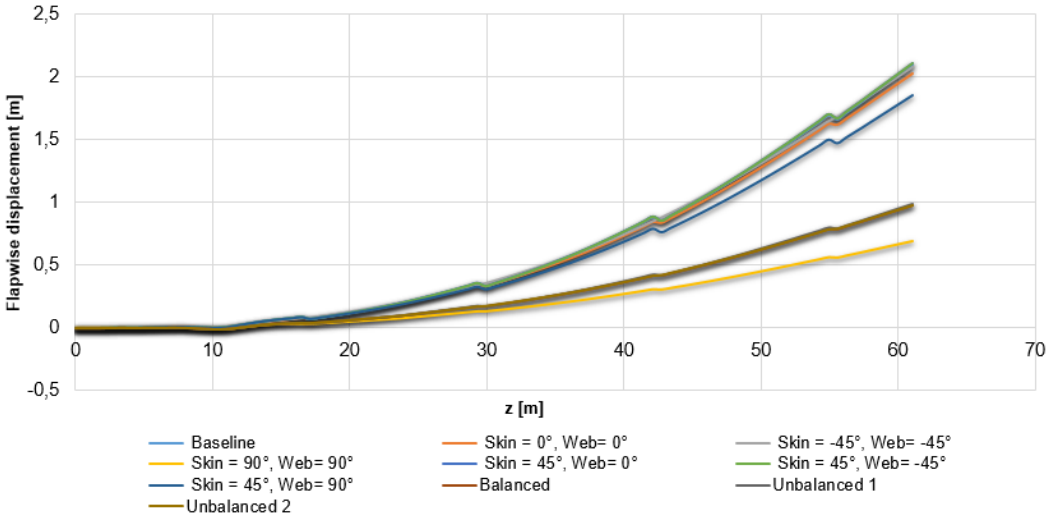

Figure 7.8: Flapwise displacement at $(^{x}/_{c}) = 25\%$ for different fibres orientation.

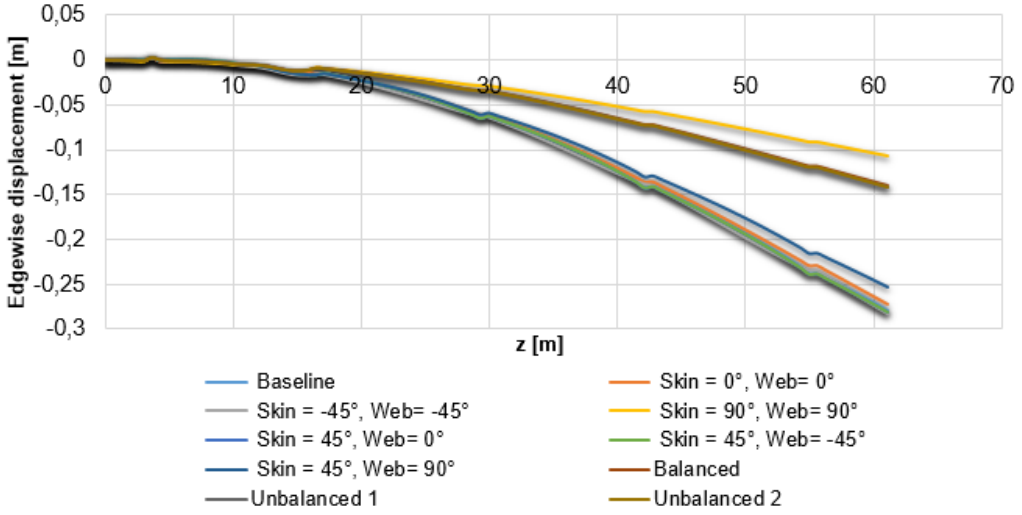

Figure 7.9: Edgewise displacement at $(^{x}/_{c}) = 25\%$ for different fibres orientation.

The stress plots in figures 7.10 and 7.11 evidence predominantly stress peaks in the shear webs insertion, which reinforces the importance of having these structures to provide a relevant source of stiffness to the structure.

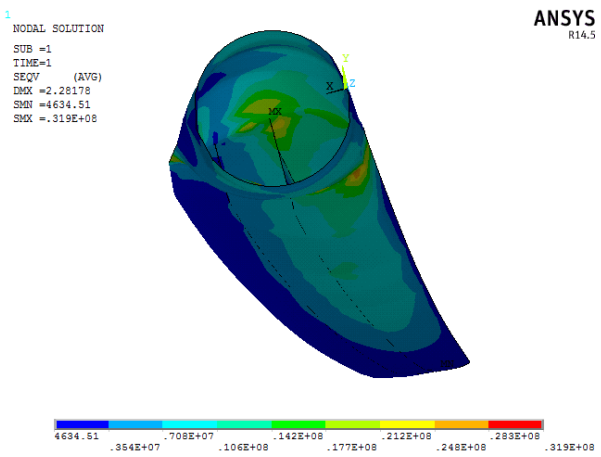

(a) von Mises equivalent stress distribution: $\theta_{skin} = 0°$, $\theta_{web} = 0°$.

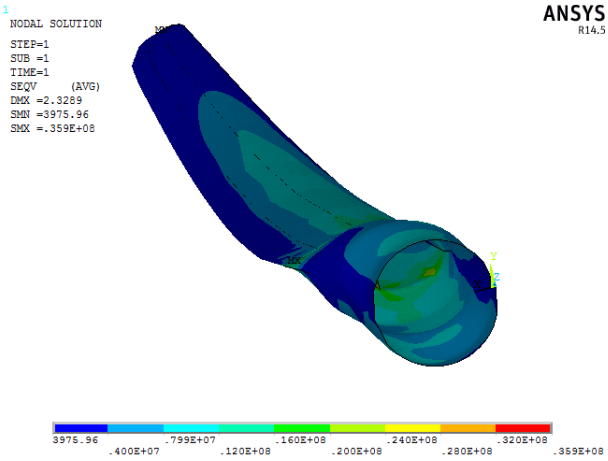

(b) $\theta_{skin} = -45°$, $\theta_{web} = -45°$ distribution

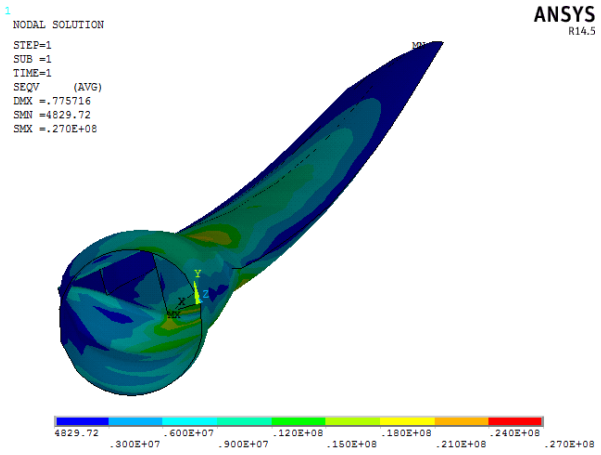

(c) $\theta_{skin} = +90°$, $\theta_{web} = +90°$

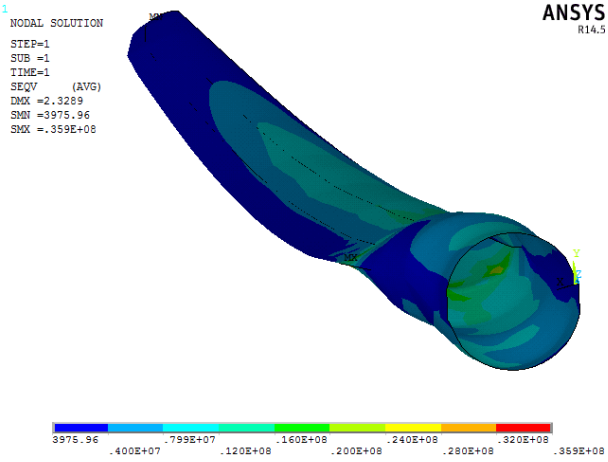

(d) $\theta_{skin} = +45°$, $\theta_{web} = 0°$ distribution

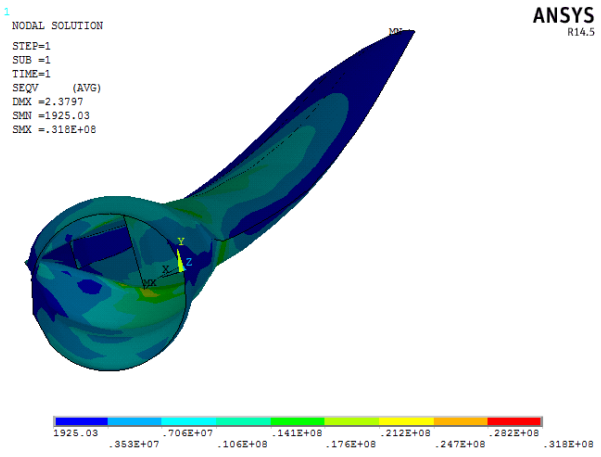

(e) $\theta_{skin} = +45°$, $\theta_{web} = -45°$

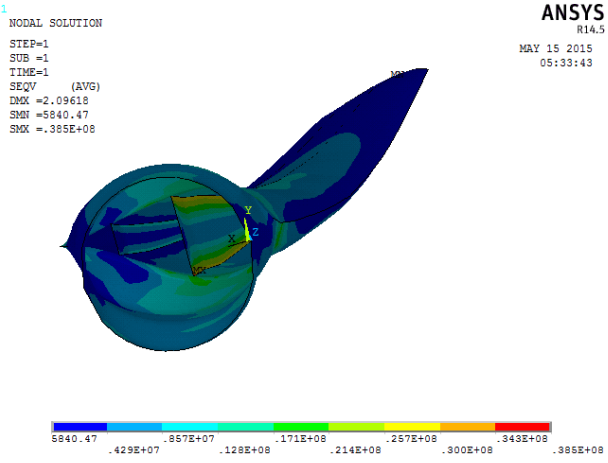

(f) $\theta_{skin} = +45°$, $\theta_{web} = 90°$

Figure 7.10: von Mises equivalent stress distribution: unidirectional stacks.

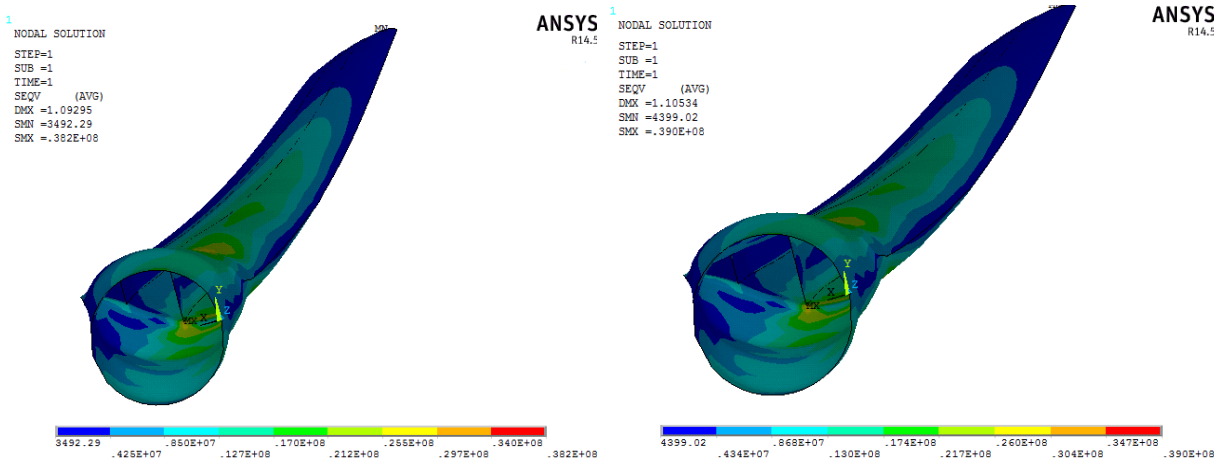

(a) Balanced stack.

(b) Unbalanced 1 stack. distribution

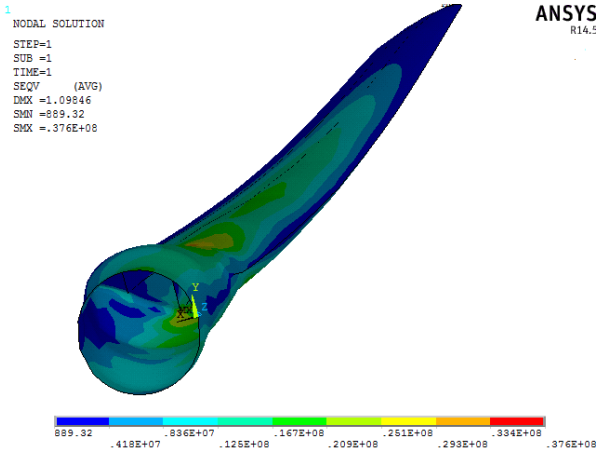

(c) Unbalanced 2 stack.

Figure 7.11: von Mises equivalent stress distribution: multidirectional stacks.

7.5 Thickness Distribution

It is known that thickness is closely related with structures stiffness, whereby making this parameter critical in design. What distinguish this parameter from many others is that by changing it, the mass is also changing, which may induce not unpredictable responses. Based on similar researches [5], two simple thickness distributions were implemented in the structural model, as illustrated in figure 7.12.

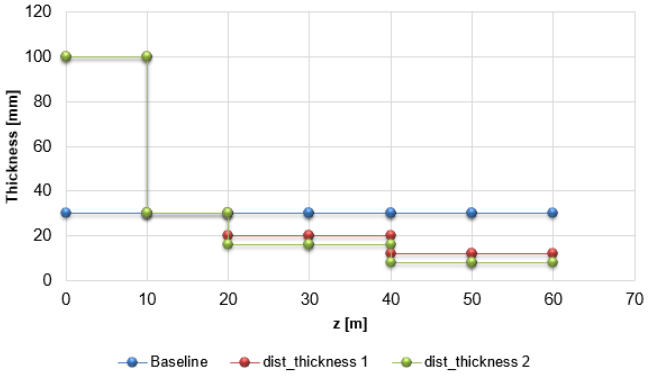

Figure 7.12: Variable thickness distributions.

Both flapwise and edgewise displacements in figures 7.13 and 7.14 are significantly increased in relation to the baseline configuration, namely in the distribution with thinnest layers. Perhaps, flapwise displacement with these distributions are unrealistic, because it is only being considered the effect of aerodynamic load. Adding other sources of load that the blades are subjected (see section 2.2), it would be possible to achieve tip displacement of about 10% of blade span, that would generate very short clearance distances to the wind turbine tower. However, looking carefully at the displacement plots is still, possible to distinguish two different trends. Until half-span, both displacements are lower than baseline, which means that this region might have a good thickness estimation. The same does not happen in the second span half, which gives a decisive contribution to the total displacement.

Thickness dist.	$y_{max}\ [m]$	$x_{max}\ [m]$	$\lvert\beta_{max}\rvert\ [°]$	$\sigma_{eqv,max}\ [MPa]$
Baseline	2.36	-0.31	$-0,80$	29.8
1	2.95	-0.32	$-1,473$	18.9
2	3.60	-0.37	-1.59	26.4

Table 7.10: Thickness distribution; maximum values

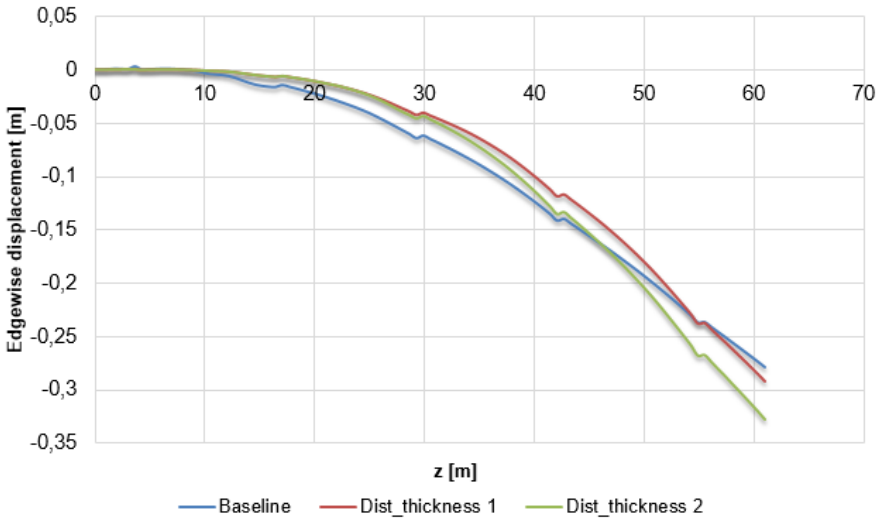

Figure 7.13: Edgewise displacement at $(^{x}/_{c}) = 25\%$ for different thickness distributions.

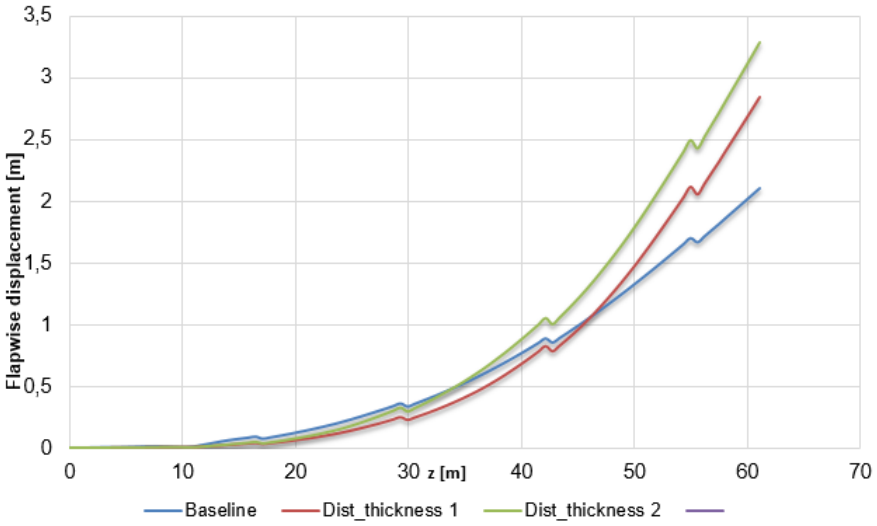

Figure 7.14: Flapwise displacement at $(^{x}/_{c}) = 25\%$ for different thickness distributions.

The induced twist, illustrated in figure 2.2 is largely benefited with variable thickness, since the reduction of thickness, not only reduce flapwise stiffness, EI, as seen in figure 7.14, but also the torsional stiffness, GJ.

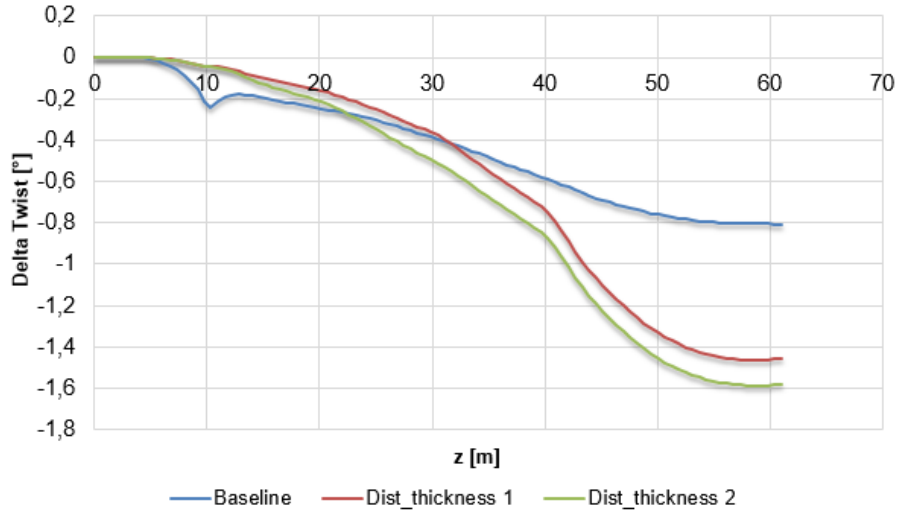

Figure 7.15: Twist distribution for different thickness distributions.

Figures 7.16(a) and 7.16(b) show that the maximum stress is now located much closer to the tip, where the thickness is significant smaller in comparison with the baseline configuration. Even so, the maximum absolute values in table 7.10 are lower than baseline.

This analysis proves that the adjustment of laminate thickness should take into account the load distribution over the blade surface, but also the tolerance to the flapwise displacement.

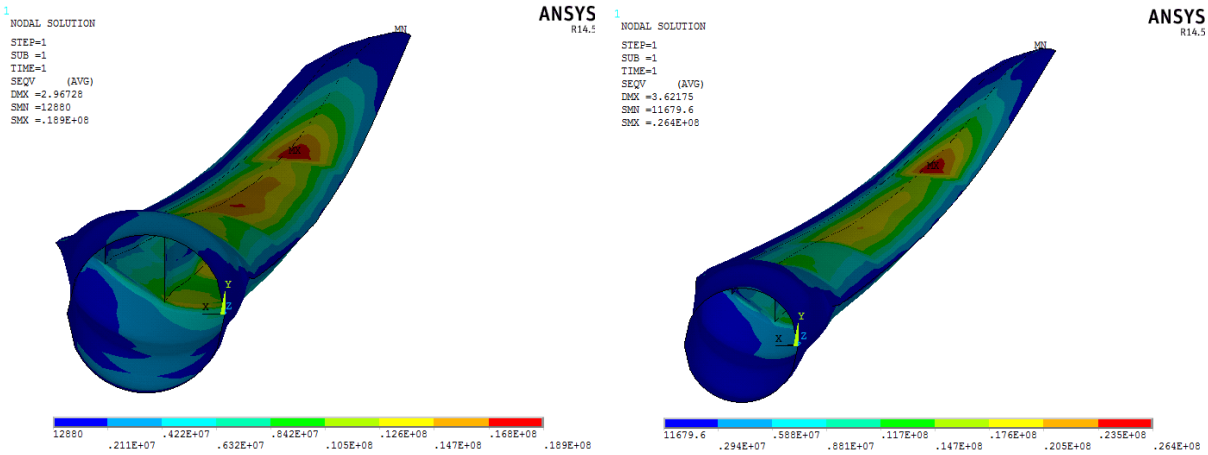

(a) Thickness distribution 1.

(b) Thickness distribution 2.

Figure 7.16: von Mises equivalent stress for different thickness distributions.

7.6 Shear Webs Location

The shear webs study seeks to observe the influence on the number of webs, but also their position in the structural behaviour of the blade. To this end, three different cases were performed; the first includes a blade with the same outer geometry but with no webs, the second has one web located at 45% of chord and the last has two webs displaced 30% towards leading edge, i.e., at 15% and 45% of chord.

The results from figures 7.17 to 7.19 are explicit about the importance of shear webs in hollow structures, since the configuration without webs presents the worst performance from all points of view. It is also interesting to observe from those figures that both displacement and twist evidence similar performances regarding the configurations with one and two webs, whereby raises the question about whether the second web is really necessary or not. The interesting point in this analysis is that the results of the configuration with one web are so close to the baseline that this latter curve is unnoticeable. This leads to the obvious conclusion that the use of the second web, where it is in baseline configuration, have revealed to be useless.

Number of webs	Web location $\%[x/c]$	$y_{max}\ [m]$	$x_{max}\ [m]$	$\beta_{max}\ [^\circ]$	$\sigma_{eqv,max}\ [MPa]$
Baseline	45;75	2.36	-0.31	-0.80	29.8
0	—	2.67	-0.40	-0.70	52.8
1	45	2.37	-0.31	-0.80	30.0
2	$15; 45$	2.25	-0.30	-0.78	25.8

Table 7.11: Number of webs; maximum values.

The stress plots in figure 7.20, show equivalent distributions for all configurations, but the absolute maximum occur, obviously, for the configuration without webs. Observing more carefully to stress values in table 7.11, one observes that from the introduction of the first web, the maximum is reduced approximately by 43.2%, whereas from the first to second web that reduction is only of 14%.

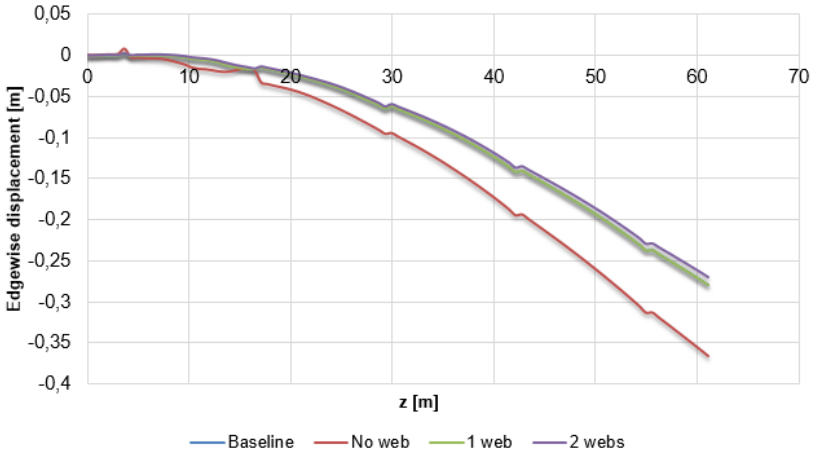

Figure 7.17: Edgewise displacement at $(x/c) = 25\%$ for different different number of webs.

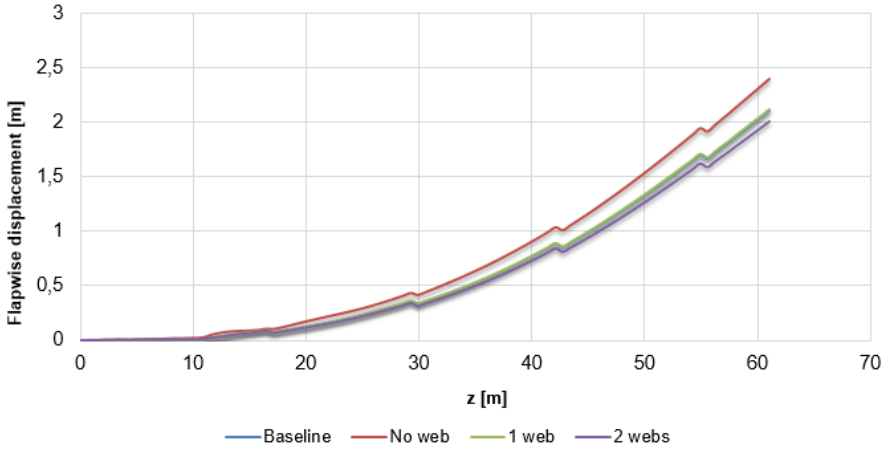

Figure 7.18: Flapwise displacement at $(x/c) = 25\%$ for different different number of webs.

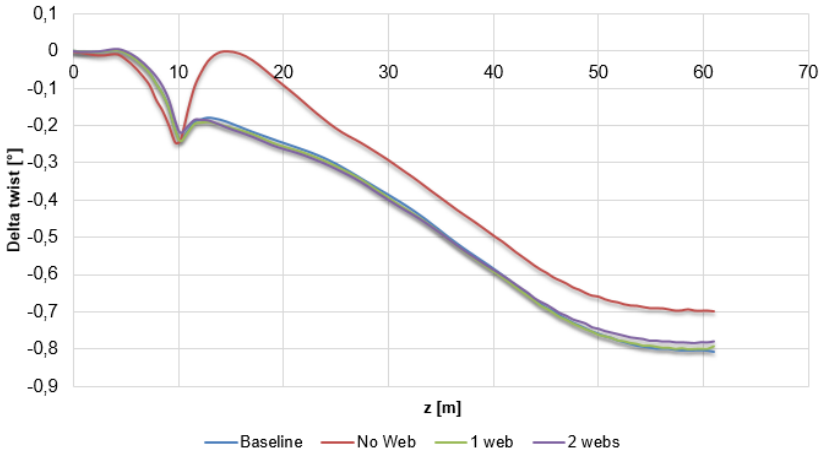

Figure 7.19: Twist distribution for different number of webs.

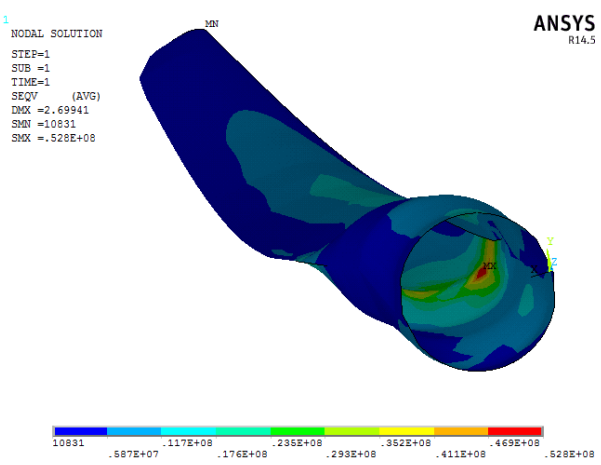

(a) Blade with no webs.

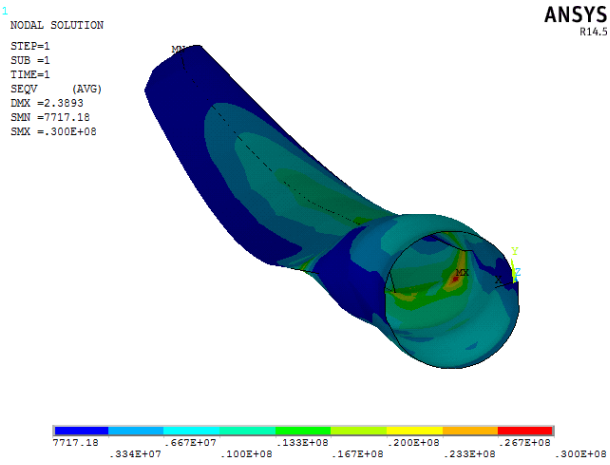

(b) Blade with one web

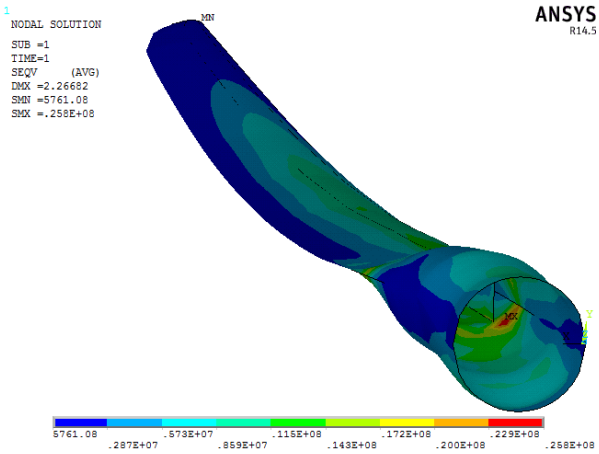

(c) Blade with two webs at 15% and 45% of chord.

Figure 7.20: von Mises equivalent stress distribution: number of webs.

7.7 Material Reinforcement

The last study focus the attention on the combination of more than one material in the blade design. It is very usual the application of carbon fibres in parts of the blade, due the excellent mechanical properties they present [5]. In table 7.12 is presented the mechanical properties of carbon (T300)/epoxy composite.

Density $\rho\ [kg/m^3]$	1590
Longitudinal modulus $E_{11}\ [GPa]$	155
Transversal modulus $E_{22}\ [GPa]$	9
Poisson coefficient ν	0.3
Distorsion modulus $G\ [GPa]$	3.5

Table 7.12: Carbon(T300)/epoxy composite mechanical properties [5].

The longitudinal modulus of this composite is largely superior than e-glass/epoxy, while the transversal and distortion modulus are slightly inferior. Carbon/epoxy composite is applied in two of the interior layers, as shown in figure 7.21.

Figures 7.23 and 7.22 have shown that provide identical displacement fields, while the twist is significantly increased, with improvements in the order of 20%, as illustrated in figure 7.24. This result can be

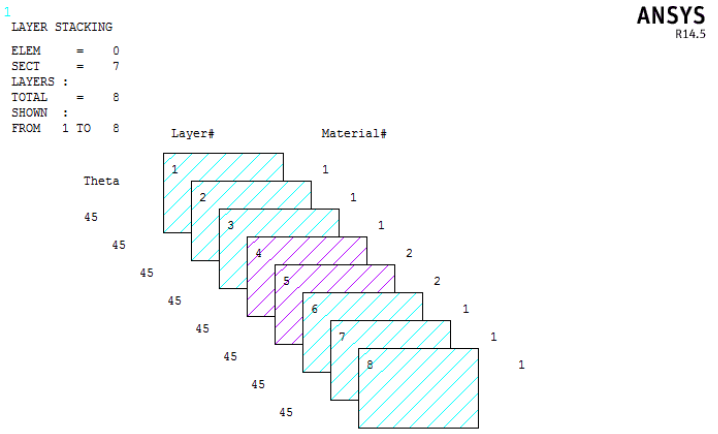

Figure 7.21: Laminate stack with carbon(T300)/epoxy reinforcement.

explained exclusively by the carbon intrinsic elastic properties, which presents a reduced transversal a distortion modulus.

Material	$y_{max}\ [m]$	$x_{max}\ [m]$	$\lvert\beta_{max}\rvert\ [^\circ]$	$\sigma_{eqv,max}\ [MPa]$
Baseline (e-glass/epoxy)	2.36	-0.31	$-0,80$	29.8
Reinforced (e-glass/epoxy + carbon/epoxy)	2.44	-0.32	-1.0	26.8

Table 7.13: Material reinforcement; maximum values

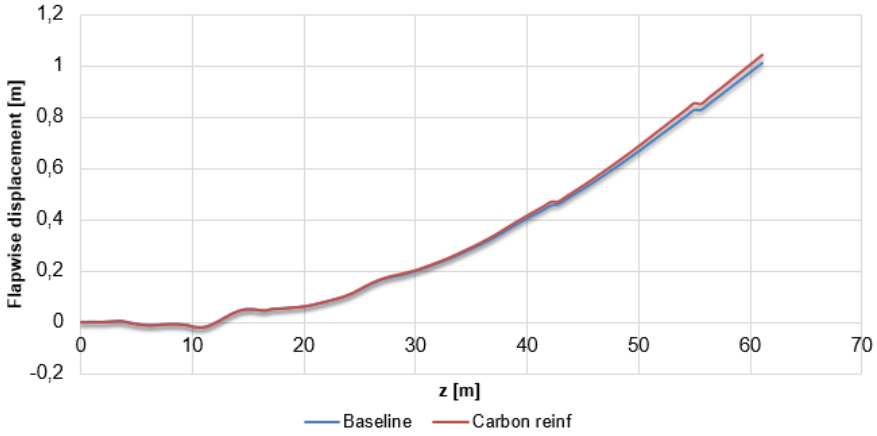

Figure 7.22: Flapwise displacement at $(x/c) = 25\%$.

Moreover, the stress distribution in figure 7.25, obtained by introducing the reinforced layers, is quite similar to the baseline, which confirms that the structural behaviour do not contribute negatively to the amount yielded amount of twist. If one takes into account that the maximum stress is lower than baseline, then it is justified to apply this solution in further designs.

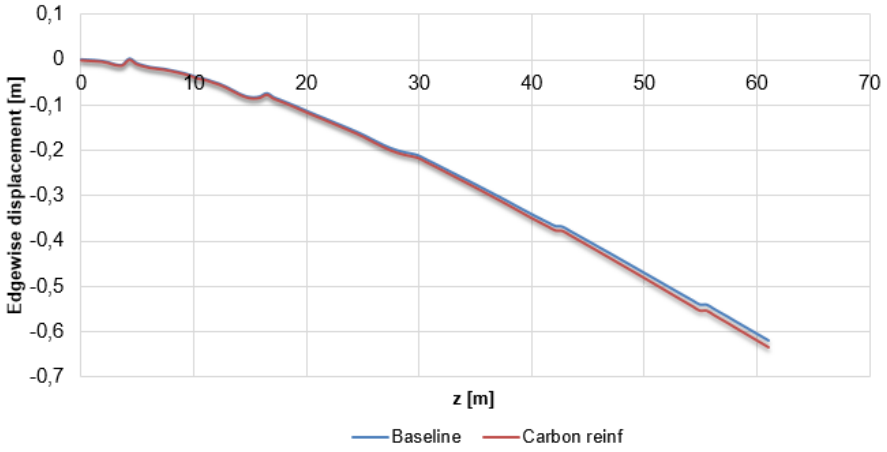

Figure 7.23: Edgewise displacement at $(x/c) = 25\%$ for material reinforcement.

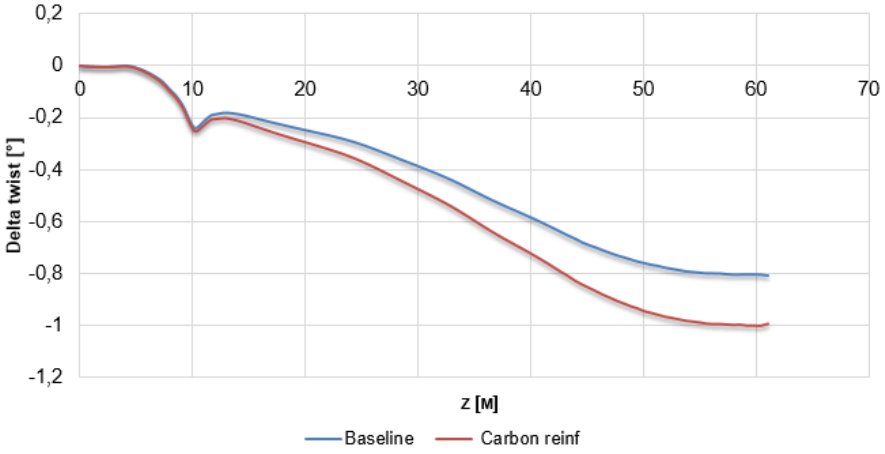

Figure 7.24: Twist distribution.

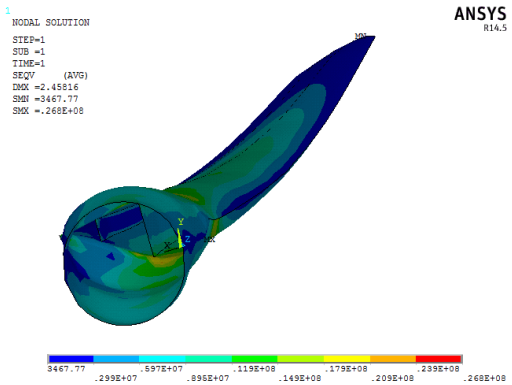

Figure 7.25: von Mises stress distribution: material reinforcement.

7.8 Parametric Study Summary

All the evaluated parameters proved to the be quite relevant to blade structural behaviour. The fibres orientation is one parameter that might be adjusted as function of the local required stiffness, and can provide significant improvements in the overall performance. It was seen that when the fibres are oriented 90°, the flapwise stiffness is greatly increased. This kind of stack is useful in regions that are subjected to high flapwise moments, which is the case of root region [49]. Obviously, this orientation avoids twist, but it was shown that the root is very resistant to torsional moments, regardless the fibres orientation, due to its geometrical properties. The remaining blade surface should integrate fibres oriented +45°, that can induce the highest amount of twist. As function of the displacement observed 90° fibres may be added to reduce the tip displacement.

The thickness is probably the most sensitive and unpredictable parameter of all studied, and its refinement should be done very carefully. The results show that thicker laminates should be used near the root to reduce the maximum flapwise displacement. Twist is sacrificed with this choice, but the structure integrity in the priority. Followed by other design options, the torsional stiffness increase can be mitigated.

Concerning the webs analysis, the reason why blades have shear webs was clear. The number of webs showed no obvious conclusions, though the global structural response is enhanced when the shear webs are introduced. The questions is whether use one or more webs. That question should be answered by trying to add more information about an optimal position of single web configuration and compare with the respective double web configuration. Anyway, theoretically, adding a second web may be always considered a conservative approach, and that is not an option to discard.

Adding another material with different elastic properties brings a new set of possibilities to improve the blade design. Looking at the mechanic properties of carbon/epoxy, it would be clever to introduce it in 90° fibres and take advantage of high longitudinal modulus of this material. Since it also provides an increase in induced twist, combined with an adequate thickness distribution, then it can be used until mid-span region, where laminate thickness is still considerable.

Chapter 8

Enhanced Blade Design

In the last chapter it was possible to collect an amount of data relative to the parameters one should take in consideration in wind turbine blade design. The parametric study was concluded with clues about an enhanced version of the blade under study, aiming a mitigation of the aerodynamic load.

8.1 Design properties

Following the sequence of parameters studied in the last chapter, the fibres orientation should be such way, that it can provide both flapwise stiffness and induced twist on the blade. Therefore, assuming that the blade root is subjected to high flapwise moments, all layers with 90° fibres (longitudinal direction) were used, so a high longitudinal stiffness can be achieved with this layup. The root laminate stack is presented in figure 8.1(a).

Ideally, the remain blade surface should be covered by layers with -45° fibres, but buckling issues might occur and for that reason, usually real blades have layers with longitudinal fibres [49]. Hence, it was applied a stack to the blade surface as illustrated in figure 8.1(c).

The region right next to the root, between 10 and 20m, has shown to be region of structural demand, thus two additional longitudinal fibres were replaced from -45°, creating an intermediate solution between root and tip stacks, as illustrated in figure 8.1(b).

The thickness distribution was maintained to the one identified as $dist\_thickness\ 1$ in figure 7.12. The author believes that the positives effects of new laminate stack, will mitigate adverse effects of having this thickness distribution, namely the loss of flapwise stiffness.

The shear webs position was changed in relation to the baseline configuration, although the double web configuration has been maintained. The argument of this modification has to do with the lack of effectiveness demonstrated by the shear web located closer to the trailing edge. Despite the good performance evidenced by the single shear web configuration, it is not clear that this performance could be consistent when a variable thickness distribution is introduced. Furthermore, in the research that supported this work, the double web configuration is rather used than single one. Further studies would have be necessary to abandon this conservative solution.

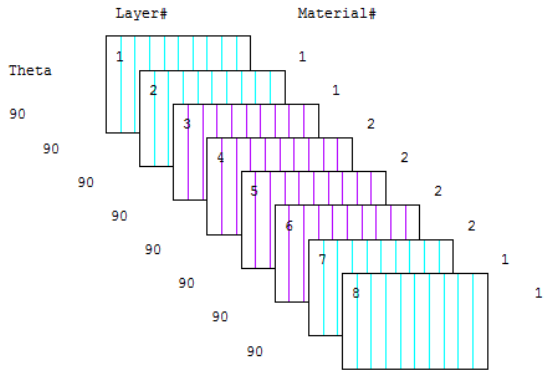

(a) Root.

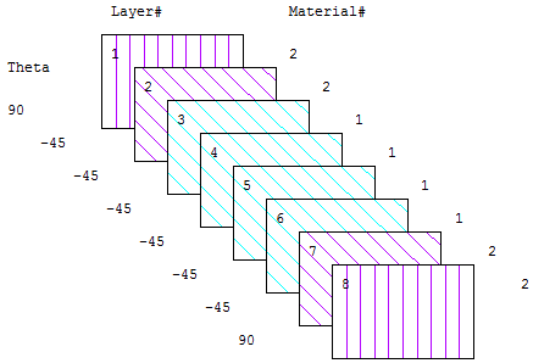

(b) Midspan.

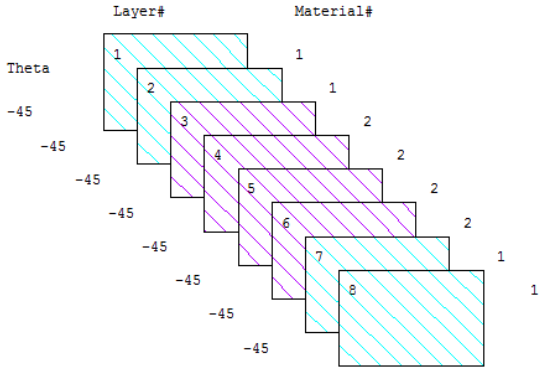

(c) Tip.

Figure 8.1: Laminate stacks in different blade regions.

Finally, regarding the reinforcement done in the previous chapter, it revealed to be successful and it was integrated in the laminates stack, as shown in figures 8.1(a) to **??** labelled by material 2. In root, the interior layers were changed to the carbon composite, and the remaining blade span, included carbon fibres not only in the longitudinal layers, but also in the interior layers containing oblique fibres.

8.2 Coupled Analysis

This analysis consisted of a iterative solution, coupling the structural twist $\Delta\beta$ into the aerodynamic model to obtain an updated surface load, as explained in detail in section 6.3. The simulation has been ran until the convergence of both displacements and forces have been verified.

8.2.1 Structural Performance

With five iterations was possible to get a converged solution, regarding nodal displacements and twist distribution.

The results show that the aerodynamic load can effectively be mitigated with this design, and produce significant reductions in both flapwise and edgwise displacement, which are visible in figures 8.2 and 8.3. The twist distribution in figure 8.4 is also lower when the solution is converged, but that difference

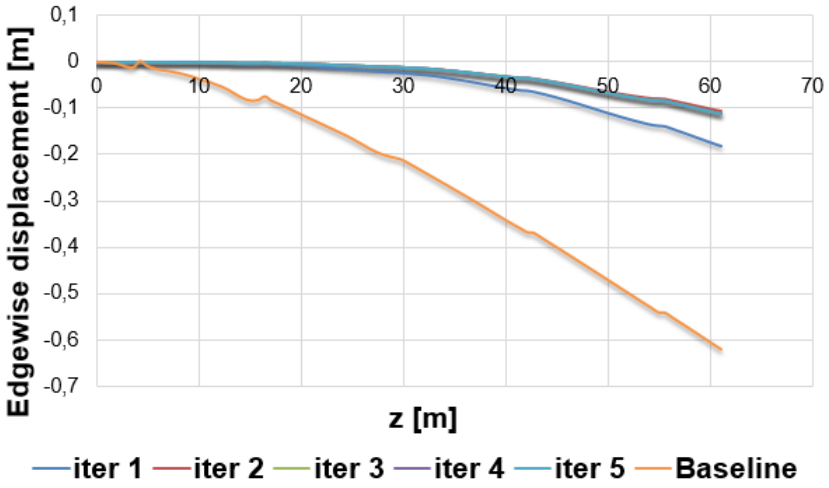

Figure 8.2: Enhanced blade: edgewise displacement at $(^{x}/_{c}) = 25\%$.

is not as noticeable, as table 8.2 confirms.

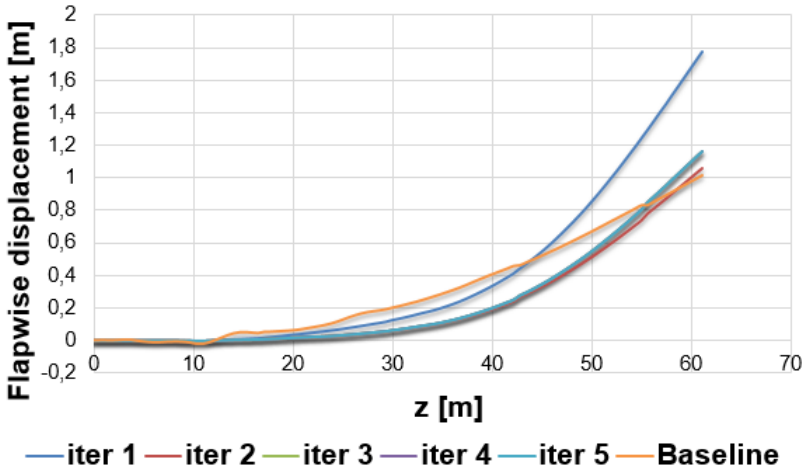

Figure 8.3: Enhanced blade: flapwise displacement displacement at $(^{x}/_{c}) = 25\%$.

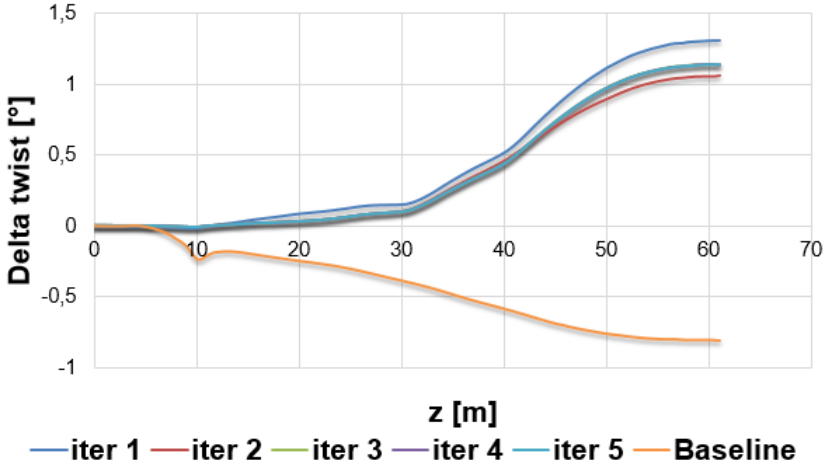

Figure 8.4: Enhanced blade: twist distribution.

The stress distribution, in figure 8.5 shows that the reinforcement applied after the root region was not sufficient to mitigate the high stress in that region, although the maximum value exhibited in table 8.1 it is clear lower than the estimated yield strength of composite in the previous chapter. Even though, since two different materials are being used, the structure will enter in plastic regime when the first of two materials enter in plastic regime. Hence, it is necessary to guarantee that the maximum stress is not higher than the carbon/epoxy yield strength. Applying once more equation (7.1), it simple to conclude that

$$(\sigma_{y_c})_2 \approx 633.4\ MPa, \tag{8.1}$$

is proportional directly proportional to the composite longitudinal modulus, as the matrix is the same. The first material to achieve eventual plastic strains is the e-glass/epoxy composite, which is not this case. Anyway, further investigations should be done in this particular point, as some researchers [10], [25] affirm that designs implemented high levels of BTC can increase fatigue loads. Therefore, the impact of this stress in fatigue lifetime should be evaluated.

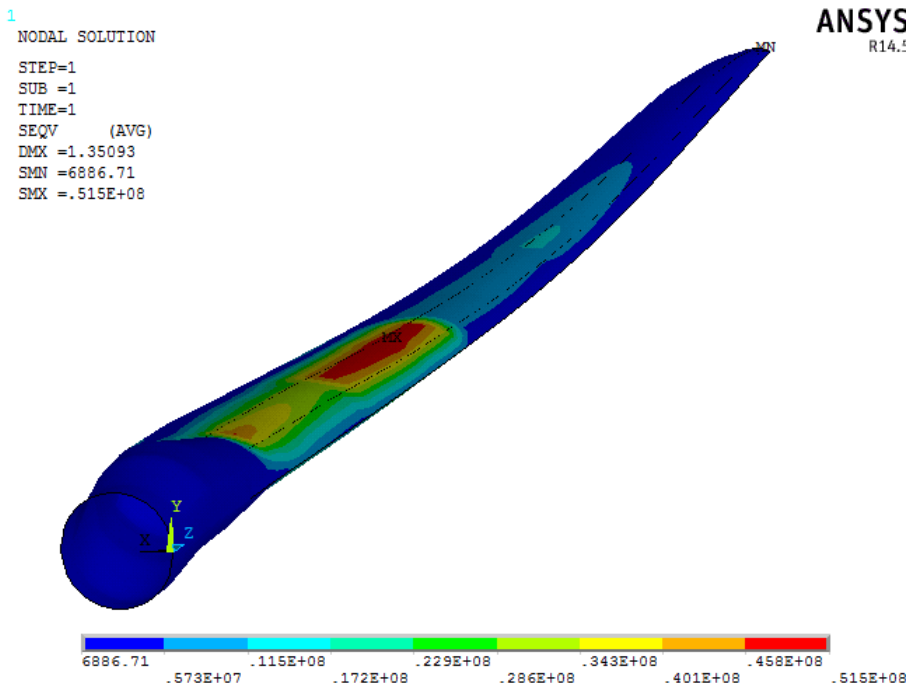

Figure 8.5: Enhanced blade: von Mises stress plot.

Iteration	$y_{max}\ [m]$	$x_{max}\ [m]$	$\beta_{max}\ [^\circ]$	$\sigma_{eqv,max}\ [MPa]$
1 to 5	2.05	−0.20	1.31	59.2
5	1.35	−0.12	1.14	50.8

Table 8.1: Enhanced blade: maximum values.

The estimated total load in upper and lower blade surfaces were

$$|F\_upper^{(1)}| = 87.3\ kN \ \ and \ \ |F\_lower^{(1)}| = 33.5\ kN$$

Iteration	Δy_{max} [%]	$\Delta\ x_{max}$ [%]	$\Delta\ \beta_{max}$ [%]	$\Delta\ \sigma_{equ,max}$ [%]
5	-35.5	-37.7	-13	-14.2

Table 8.2: Enhanced blade: parameters deviations between first and last iterations.

In the end of coupled analysis, these values were

$$|F\_upper^{(5)}| = 85.0\ kN \quad and \quad |F\_lower^{(5)}| = 33.4\ kN$$

Resulting in total aerodynamic load reduction of 2.1%. This result indicates that from modest reductions in aerodynamic load, is possible avoid extreme displacements, verified by the blade, whenever wind speed is much higher than normal. The benefits may be extended to an increase in blade lifetime.

8.3 Aerodynamic Performance

The aerodynamic parameters are not significantly affected by this enhanced design, nevertheless, it is visible in both figures 8.6 and 8.7 deviations specially in the second half of span, where the twist is more appreciable. In the former, that is a direct consequence of the reduction in the angle of attack. The latter, it is negative effect of induce twist, because the torque exerted on the blade is reduced. Instead of making the air flow rotate, it is the blade itself that is rotating, losing the rotational kinetic energy that could be extracted from wind. Therefore, the angular induction factor is lower with this design, which gives a negative contribution to power production, as can be seen by equation (7.2).

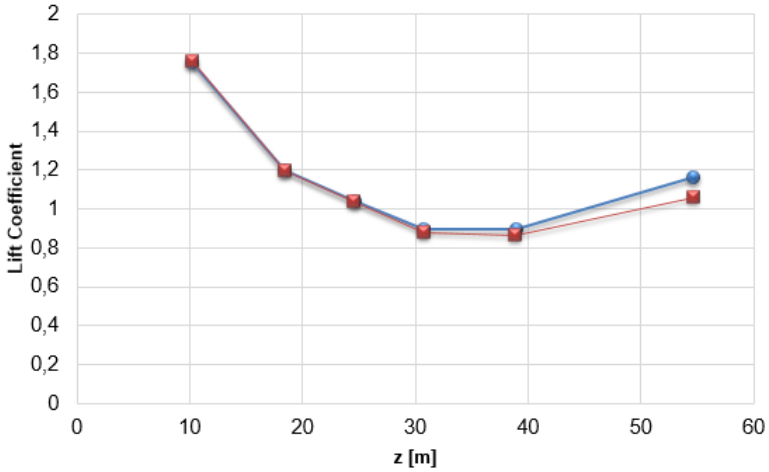

Figure 8.6: Enhanced blade: lift coefficient.

8.4 Static Analysis including Inertial Loads

This final analysis aims to give an insight about the impact of inertial loads on the blade response. This analysis followed exactly the same procedures of the previous one, but in this case it was considered an

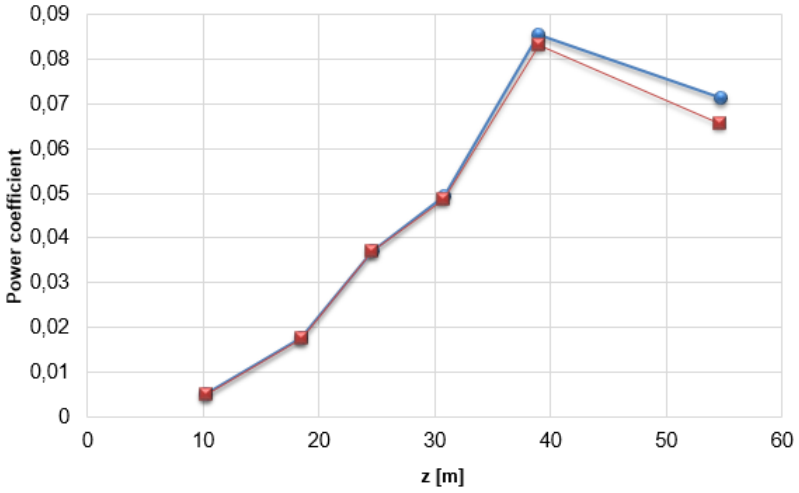

Figure 8.7: Enhanced blade: power coefficient.

extreme case, where aerodynamic, gravitational and gyroscopic loads are acting in the same direction, with the blade parallel to the ground.

The maximum tip deflection used in [49], was 8.46 m, for a rotating situation. In that work, a 70 m blade was analysed, also developed by NREL, with identical geometrical features. Thus, it is acceptable to make linear re-scaling to have a reference value about the maximum tip deflection of the blade one is working. The estimated value was 7.25 m. In [49], it is also applied a safety factor of 1.35 in all forces, but for convenience, in this analysis it was applied the same safety factor to the maximum tip deflection, yielding 5.37 m. The reference angular velocity used during the simulations is the rated rotor speed, as described in table 7.1.

The same trends verified in the previous analysis are visible in figures 8.8 to 8.10. The main differences lie on the maximum absolute values, that are quite superior due to the introduction of the additional sources of load. The reference maximum tip deflection is not reached, but it should be noted that other types of load can still be added to the ones considered so far, which may induce even higher displacements.

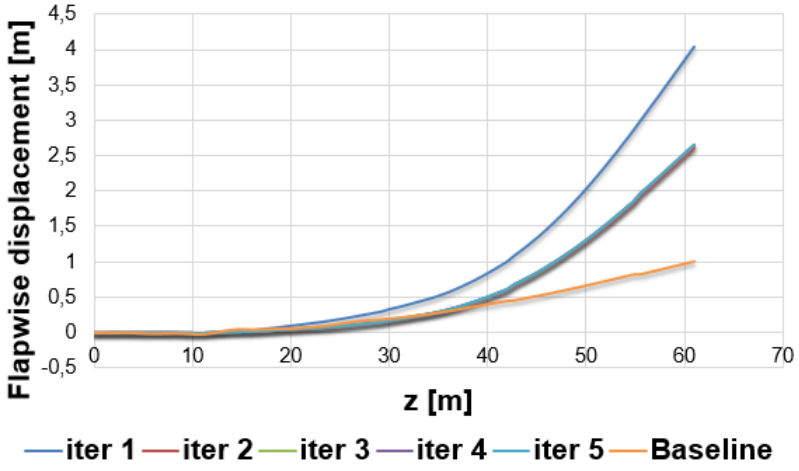

Figure 8.8: Enhanced blade including inertial loads: flapwise displacement at $(^{x}/_{c}) = 25\%$.

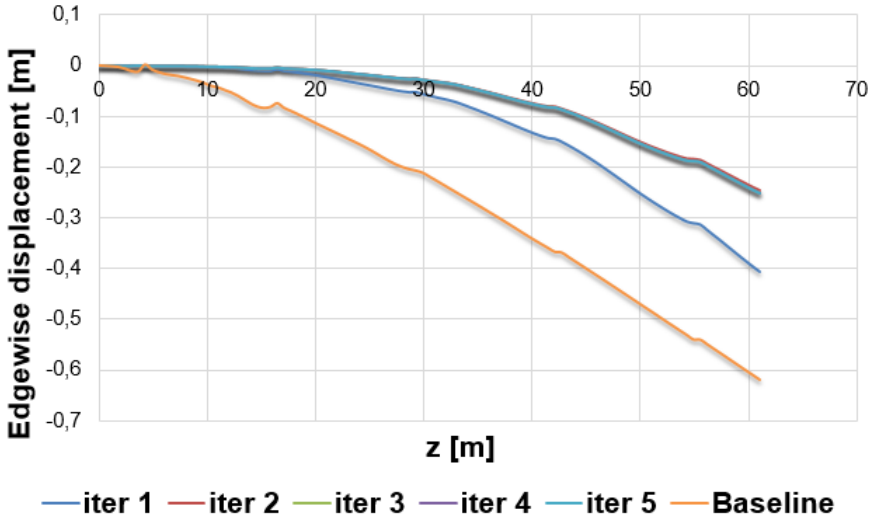

Figure 8.9: Enhanced blade including inertial loads: edgewise displacement at $({}^{x}/_{c}) = 25\%$.

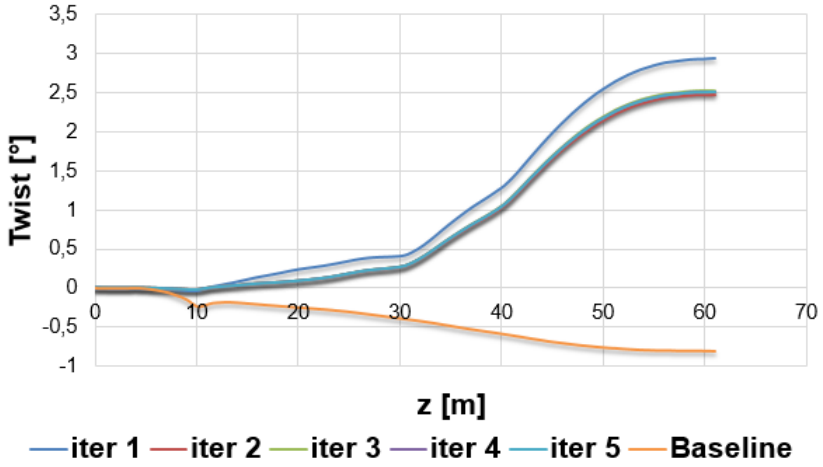

Figure 8.10: Enhanced blade including inertial loads: twist distribution.

The increase in total load is also reflected on the stress exerted on the blade. The distribution is similar to the one of analysis, but while in that one the maximum stress clearly below the estimated yield strength, the actual load yields a maximum much closer to this boundary. Furthermore, applying the same safety factor to the composite yield strength, in fact this threshold is slightly exceeded. Similarly as what happens in figure 8.5, from the stress plot in figure 8.11, it is evident an overstressed region next to the root, due not only to the insertion zone of webs, but also where high suction zones are found. Therefore, for a more conservative approach, it is prudent, to reinforce this zone either by changing some of the oblique layers by longitudinal layers or, alternatively, make a slight adjustment in the laminate thickness.

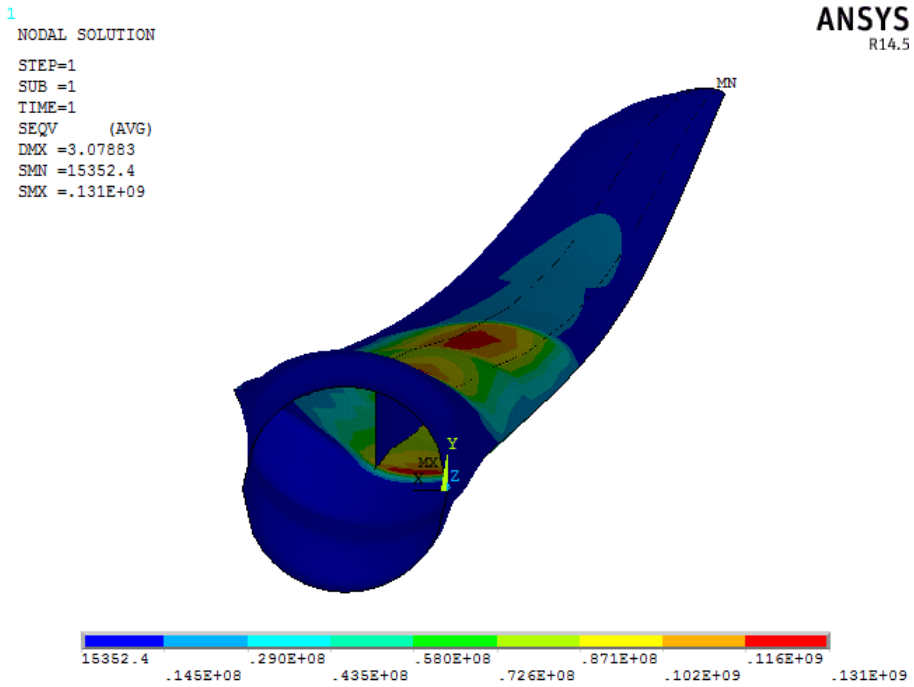

Figure 8.11: Enhanced blade including inertial loads: von Mises stress.

Chapter 9

Conclusions

Wind energy is actually one industry in steady evolution and, in the next decades, it is expected that a significant part of the total yielded clean energy is exclusively extracted from wind. In this context, wind turbines followed the technological advances and nowadays are quite complex structures, incorporating not only noble materials but also advanced control systems, aiming power outputs that can justify the production cost of such devices.

The passive control is a very efficient approach in terms of cost, that can maintain at acceptable levels the blade power output and reduce the aerodynamic load in case of high wind speeds. The bend-twist coupling is one technique of passive control that can provide that desired aerodynamic load mitigation, reducing the wind incidence on the blade. These effects are more noticeable, the greater the wind speed is.

The selected parameters in the parametric study provide several solutions to produce an enhanced blade model, and can significantly change both mechanic properties of the blade and the structural response. They can be adjusted in order to produce the desired effects in terms of the maximum displacements and in the amount of twist.

The design presented in this work focused in a blade configuration that could provide the maximum twist possible, in a such way that applying the BTC concept could achieve an effective aerodynamic load reduction. This reduction is particularly visible in lower maximum displacements and stresses in the structure.

The developed enhanced design was justified from the findings of a parametric study and confirmed its proposals. Besides the reduction of total aerodynamic load through the coupling of induced self twist, both blade flapwise and edgewise maximum deflections were reduced with this design. Taking into account the reference values and all the developed reasoning, it has been shown that the blade stiffness was correctly dimensioned, as the maximum stress ranged below the material yield strength.

The integration of inertial loads in the analysis has confirmed that these source of loads are quite relevant in the design stage, as they represent a significant part of total load exerted upon the blade. This design maintained enough sturdiness to keep maximum displacements below reference values, so a sort of static validation of this model was performed successfully.

9.1 Achievements

This research allowed a complete, but not exhaustive insight about wind energy. The knowledge about wind turbines require a lot of different engineering sciences, as aerodynamics, composite materials, structural mechanics, as many other. Deeper and stronger bases were built in these fields to produce this report.

A simple mesh generator was developed, capable to compute a parametric structured mesh relative to a WTB, regardless of its geometry.

The developed aerodynamic model, despite its simplicity, allowed an estimation qualitatively correct about the pressure distribution.

It was possible to evaluate from a set of parameters what were those who were more relevant to blade structural behaviour. From the evaluated parameters, it was computed an enhanced design of the blade under study, that fulfilled the desired goals.

9.2 Future Work

The model developed in the scope of this work should be validated through commercial codes. They typically rather evolve all WT components than exclusively the blade, therefore extrapolations to the developed model should be done.

In this work, the emphasis is given to the aerodynamic load, and a brief analysis with inertial loads was made. Further advances should be done in this field, adding others source of load, and considering non-linear components. It would be interesting to implement stochastic models, already existent representative of the non-periodic wind loads. The study of the impact of fatigue loads, in this context, will be very useful.

During the parametric study some questions were not answered. The ideal number and the position of shear webs became inconclusive, and further studies are needed to have clear picture about this particular point. A buckling analysis, crossing all the gathered data will also add value to this research

The aerodynamic model should suffer several improvements, particularly the pressure distribution in root, which the estimation is very rough. Other types of tools, as CFD codes, should be employed to have more precise load distributions.

The developed FSI model should take into account the mesh deformation in further iterations to be truly considered a loose coupling method.

Bibliography

[1] Brian R Resor. Definition of a 5MW / 61 . 5m Wind Turbine Blade Reference Model. 2013.

[2] D Otero, F L Ponta, and L I Lago. Structural Analysis of Complex Wind Turbine Blades: Flexo-Torsional Vibrational Modes. *Advances in Wind Power*, 2012. doi: 10.5772/51142.

[3] Pengwen Sun, Zhifu Liu, Yongguang Gao, and Sheng Wu. Lay-up Design and Structural Analysis of 1.2MW Composite Wind Turbine Blade. 2009. 9781424452682.

[4] Prospector Materials database. https://www.ulprospector.com/en/na. *Energy Procedia*, (1876):194–201. Visited in May 2015.

[5] Manudha T. Herath, Aaron K.L. Lee, and B. Gangadhara Prusty. Design of shape-adaptive wind turbine blades using differential stiffness bend-twist coupling. *Ocean Engineering*, 95:157–165, February 2015. doi: 10.1016/j.oceaneng.2014.12.010.

[6] Low Tech Magazine. http://www.lowtechmagazine.com/2009/10/history-of-industrial-windmills.html. Visited in February 2015.

[7] Erich au. *Wind turbines: Fundamentals, technologies, application, economics*. Springer, 3rd edition, 2006. ISBN 10.1007/3-540-29284-5.

[8] European Wind Energy Association. http://www.ewea.org/. Visited in February 2015.

[9] J. F. Manwell, J. G. McGowan, and A. L. Rogers. *Wind Energy Explained*. John Wiley & Sons LTD, 2nd edition, 2009. ISBN 978-0-470-01500-1.

[10] W.C. de Goeij, M.J.L. van Tooren, and A. Beukers. Implementation of bending-torsion coupling in the design of a wind turbine rotor blade. *Journal of Applied Energy*, 2:191–207, 1999.

[11] D M May, S J Jones, and H Crockard. Fundamental of Aerodynamics. *Journal of neurosurgery*, 85(4):566–573, 1996.

[12] John D. Anderson. *Fundamentals of Aerodynamics*. Mc Graw Hill, 3rd edition, 2001. ISBN 0-07-237335-0.

[13] Tony Burton, David Sharpe, Nick Jenkins, and Ervin Bossanyi. *Wind Energy Hand Book*. John Wiley & Sons LTD, 2001. ISBN 0 471 48997 2.

[14] Martin O. L. Hansen. *Aerodynamics of Wind Turbines*. EARTHSCAN, 2 edition, 2008. 978-1-84407-438-9.

[15] ANSYS. *Theory Reference for the Mechanical APDL and Mechanical Applications*. 12th edition, 2009.

[16] J.N. Reddy. *Mechanics of Laminated Composite Plates and Shells*. CRC PRESS, 2nd edition, 2004. ISBN 0849315921.

[17] Galina Seiber. Numerical simulation of fluid-structure interaction using loose coupling methods. Master's thesis, Technischen Universitat Darmstadt, 2002.

[18] Dong Ok Yu and Oh Joon Kwon. Predicting wind turbine blade loads and aeroelastic response using a coupled CFD-CSD method. 70:184–196, 2014. doi: 10.1016/j.renene.2014.03.033.

[19] Vasco Brederode. *Fundamentos de Aerodinâmica Incompressivel*. Edição de autor, 1997.

[20] Peter J. Schubel and Richard J. Crossley. Wind turbine blade design. *Energies*, 5(9):3425–3449, 2012. doi: 10.3390/en5093425.

[21] Wen-Hsiang Wu and Wen-Bin Young. Structural Analysis and Design of the Composite Wind Turbine Blade. *Applied Composite Materials*, 19(3-4):247–257, 2012. doi: 10.1007/s10443-011-9193-z.

[22] Wang Xudong. Shape optimization of wind turbine blades. *Wind Energy*, 12(8):781–803, 2009. doi: 10.1002/we.335.

[23] Niels Troldborg and Jn Sø rensen. Numerical validation of a finite elment thin-walled beam model of a composite wind turbine blade. *Wind Energy*, 15:203–223, 2012. doi: 10.1002/we.

[24] Wenping Cao, Ying Xie, and Zheng Tan. Wind Turbine Generator Technologies. *INTECH*, 2012. doi: http://dx.doi.org/10.577251780.

[25] Don W. Lobitz and Paul S. Veers. Load Mitigation with Bending/Twist-coupled Blades on Rotors using Modern Control Strategies. *Wind Energy*, 6(2):105–117, 2003. doi: 10.1002/we.74.

[26] Scott J Johnson, C P Case Van Dam, and Dale E Berg. Active Load Control Techniques for Wind Turbines. *SANDIA NATIONAL LABORATORIES,*, 2008.

[27] Dale E. Berg, Jose R. Zayas, Donald W. Lobitz, C. P. van Dam, Raymond Chow, and Jonathon P. Baker. Active Aerodynamic Load Control of Wind Turbine Blades. *Fluid Dynamics Conference*, pages 1119–1127, 2007. doi: 10.1115/FEDSM2007-37604.

[28] Matthew A Lackner and Mario A Rotea. Passive structural control of offshore wind turbines. *Wind Energy*, 14:373–388, 2011. doi: 10.1002/we.

[29] E Muljadi, K Pierce, P Migliore, National Wind, and National Renewable. Control strategy for varaible-speed Stall-Regulated Wind Turbines. *NREL Laboratories*, 1998.

[30] Dimitris Bourlis. A Complete Control Scheme for Variable Speed Stall Regulated Wind Turbines. *INTECH*, 2007. University of Leicester.

[31] Christian Deilmann. Passive aeroelastic tailoring of wind turbine blades - A numerical analysis -. Master's thesis, Massachussets Institute of Technology, 2009.

[32] V Fedorov and C Berggreen. Bend-twist coupling potential of wind turbine blades. *Journal of Physics: Conference Series*, 524:012035, 2014. doi: 10.1088/1742-6596/524/1/012035.

[33] Tom Ashwill. Passive Load Control for Large Wind Turbines. *51st AIAA/ASME/ASCE/AHS/ASC Structures, Structural Dynamics, and Materials Conference*, pages 1–12, 2010. doi: 10.2514/6.2010-2577.

[34] Andrew T Lee, B E Hons, and Richard G J Flay. Compliant blades for wind turbines. *IPENZ Conference*, 1998.

[35] Georgios Pechlivanoglou. *Passive and active flow control solutions for wind turbine blades*. PhD thesis, Technischen Universitat Berlin, 2013.

[36] XFOIL. http://web.mit.edu/aeroutil_v1.0/xfoil_doc.txt. . Visited in March 2015.

[37] M. Drela. XFOIL 6.94 User Guide. 2001.

[38] Aerodynamics for Students. http://www-mdp.eng.cam.ac.uk/web/library/enginfo/aerothermal_dvd_only/aero/fprops/poten/node37.html. Visited in March 2015.

[39] G. P. Nikishkov. *Introduction To The Finite Element Method*. Lecture Notes UCLA, 12 edition, 2004.

[40] CFD-Online. http://www.cfd-online.com/wiki/mesh_classification. Visited in May 2015.

[41] S A Brown. Displacement Extrapolations for CFD+CSM Aeroelastic Analysis. 97(1090):291–300, 1997.

[42] Ramji Kamakoti and Wei Shyy. Fluid-structure interaction for aeroelastic applications. *Progress in Aerospace Sciences*, 40(8):535–558, 2004. doi: 10.1016/j.paerosci.2005.01.001.

[43] Mauwafak a Tawfik, Mohammed I Abu-tabikh, and Farouk O Hamdoon. Aeroelastic behavior of a wind turbine blade by a fluid -structure interaction analysis. *Al- Khwarizmi Engineering*, 9(3):15–25, 2013.

[44] Timur Alexeev. *Computational Aeroelasticity Study of Horizontal Axis Wind Turbines with Coupled Bending-Torsion Blade Dynamics*. PhD thesis, 2013.

[45] J Jonkman, S Butterfield, W Musial, G Scott, J Jonkman, S Butterfield, W Musial, and G Scott. Definition of a 5-MW Reference Wind Turbine for Offshore System Development. 2009. doi: 10.1002/ajmg.10175.

[46] Emad S Al-hasani. Study of tensile strength and hardness property for epoxy reinforced with glass fiber layers. *Eng. & Technology*, 25(8):988–997, 2007.

[47] K Devendra and T Rangaswamy. Strength characterization of e-glass fiber reinforced epoxy composites with filler materials. *Minerals and Materials Characterization and Engineering*, 1:353–357, 2013.

[48] Barrie S. H. Royce. http://www.princeton.edu/m̃aelabs/mae324/11/11mae_21.htm. Visited in May 2015.

[49] Kevin Cox and Andreas Echtermeyer. Structural design and analysis of a 10MW wind turbine blade. *Energy Procedia*, 24(1876):194–201, 2012. doi: 10.1016/j.egypro.2012.06.101.

[50] Jorge Rodrigues and Paulo Martins. *Tecnologia Mecânica Vol 1 - Tecnologia da deformação plástica*. Plátano editora, 2010.

Appendix A

A.1 von Mises Failure Criterion

The von Mises failure is satisfied if von Mises equivalent stress σ_v is higher than the yield strength of the material. von Mises equivalente stress is given by [50]

$$\sigma_v = \left[\frac{(\sigma_1 - \sigma_2)^2 + \sigma_2 - \sigma_3)^2 + \sigma_3 - \sigma_1)^2}{2}\right]^{1/2}. \tag{A.1}$$

The von Mises failure criterion is satisfied when

$$\sigma_v \geq \sigma_y. \tag{A.2}$$

A.2 Thin Airfoil Theory

An airfoil is defined by first drawing a mean camber line. The straight line that joins the leading and trailing ends of the mean camber line is called the chord line. The length of the chord line is called chord, c. To the mean camber line, a thickness distribution is added in a direction normal to the camber line to produce the final airfoil shape. Equal amounts of thickness are added above the camber line, and below the camber line [12].

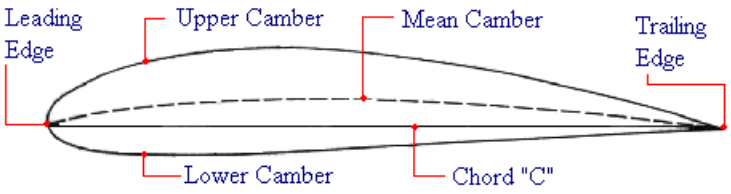

Figure A.1: Main airfoil geometric definitions (reproduced from [19]).

An airfoil with no camber (i.e. a flat straight line for camber) is a symmetric airfoil. The angle that a freestream makes with the chord line is called the angle of attack, α.

Let Y be the pressure force per unit span along the Y- axis. This force may be computed as

$$Y = \int_{lower} pdx - \int_{upper} pdx = \int (p_{upper} - p_{lower})dx. \tag{A.3}$$

We can now yield a non-dimensional form, from the above dimensional expression, by dividing the pressure by the dynamic pressure, and the distances by the chord c. Then:

$$C_Y = \frac{Y}{\frac{1}{2}\rho U^2 c} = \frac{\int[(p_{upper} - p_0) - (p_{lower} - p_0)]}{\frac{1}{2}\rho U^2 c} d\frac{x}{c} = \int (C_{P,upper} - C_{P,lower}) d\frac{x}{c}. \tag{A.4}$$

We can likewise find the component of force acting along the x- axis. This force and its non-dimensional form are given by

$$X = \int p_{upper} \left(\frac{dY}{dx}\right)_{upper} dx - \int p_{lower} \left(\frac{dY}{dx}\right)_{lower} dx, \tag{A.5}$$

$$C_X = \frac{X}{\frac{1}{2}\rho U^2 c} = \int \left[C_{P,upper} \left(\frac{dY}{dx}\right)_{upper} - C_{P,lower} \left(\frac{dY}{dx}\right)_{lower} \right] d\frac{x}{c}. \tag{A.6}$$

The X and Y- forces act along the x- and y- axes, respectively. Lift is defined as the component of pressure force that is normal to the freestream direction, and drag is defined as the component of pressure force along the freestream direction. If the airfoil was initially located so that the chord line is along the x- axis, then the angle between the freestream direction and the x- axis is the angle of attack α.

Lift and drag are related to the X- and Y- forces as

$$L = Y cos\alpha - X sin\alpha, \tag{A.7}$$

$$D = X cos\alpha + Y sin\alpha, \tag{A.8}$$

$$C_l = C_Y cos\alpha - C_X sin\alpha, \tag{A.9}$$

$$C_d = C_X cos\alpha + C_Y sin\alpha. \tag{A.10}$$

The quantities Cl and Cd are called the lift, and drag coefficients, respectively. By convention, the lower case subscripts are used in 2-D flows, while upper case subscripts are used to denote lift and drag coefficients of three-dimensional configurations such as wings.

We can also define the pitching moment about any point on the chord line. Nose up moment is considered positive. About a general point on the x- axis whose co-ordinates are given by (a,0), the pitching moment per unit span is given in dimensional and non-dimensional forms respectively by

$$M = \int (p_{lower} - p_{upper})(x - a)dx, \tag{A.11}$$

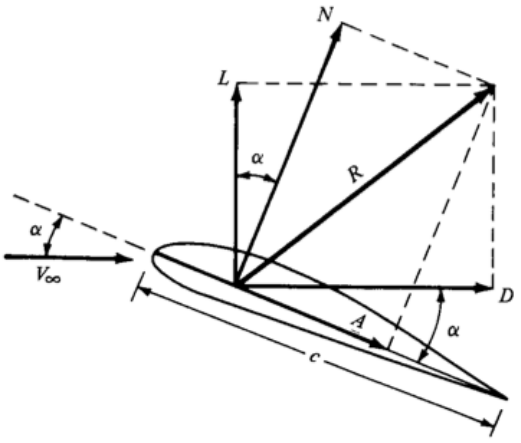

Figure A.2: Aerodynamic forces: lift and drag (reproduced from [19]).

$$C_m = \int (c_{P,lower} - C_{P,upper})(\frac{x}{c} - \frac{a}{c})d\frac{x}{c}. \tag{A.12}$$

While the pitching moment can be defined about any point in space, it is customary to compute the pitching moment M and the pitching moment coefficient Cm about the quarter chord, i.e. a location 25% downstream of the leading edge.

The centre of pressure is defined as the point about which the pitching moment is zero. As the flow conditions change (example, angle of attack α changes), the centre of pressure will change.

The aerodynamic centre is defined as the point where the pitching moment (or the pitching moment coefficient) is independent of α. That is, if we computed the pitching moment about the aerodynamic centre:

$$\frac{\partial M}{\partial \alpha} = \frac{\partial C_m}{\partial \alpha} = 0. \tag{A.13}$$

The thin airfoil theory yields the following results:

$$C_l = 2\pi(\alpha - \alpha_0), \quad \frac{\partial C_l}{\partial \alpha} = 2\pi, \tag{A.14}$$

$$C_d = 0, \tag{A.15}$$

$$\frac{\partial C_m}{\partial \alpha} = 0, \ at\ 25\%\ of\ chord. \tag{A.16}$$

The quantity α_0 is called the angle of zero lift.. In real flows, C_l, C_d and C_m will differ from this theory, due to viscous effects. As may be expected, symmetric airfoils will have zero lift at zero angle of attack. Thus, α_0 is zero for symmetric airfoils. For cambered airfoils α_0 can have positive or negative, depending on whether they have a positive (curved up) or negative camber (curved down).

Appendix B

B.1 Matlab APDL Code Generator

```
%%%%%%Output File%%%%%%%%%%

clc;


%%
%%Material Properties

Ex=43.2e9;
Ey=12.6e9;
Ez=12.6e9;
Gxy=4.2e9;
Gxz=4.2e9;
Gyz=4.2e9;
vL=0.28;
dens=1920;

fid = fopen('output_MATLAB.txt','wt');

%title
fprintf(fid,'! Edgar Carrolo\n! Wind Turbine Blade FEM\n');

%White screen
fprintf(fid,'FINISH\n /CLEAR,ALL \n /PREP7 \n /RGB,INDEX,100,100,100, 0 \n
    /RGB,INDEX, 80, 80, 80,13 \n /RGB,INDEX, 60, 60, 60,14 \n /RGB,INDEX, 0,
     0, 0,15 \n/REPLOT\n');

```

```
26
27
28  fprintf(fid,'MPTEMP,,,,,,,,  \n MPTEMP,1,0 \n MPDATA,EX,1,,%f \n MPDATA,EY
        ,1,,%f  \n MPDATA,EZ,1,,%f \n MPDATA,PRXY,1,,%f \n MPDATA,PRYZ,1,, \n
        MPDATA,PRXZ,1,, \n MPDATA,GXY,1,,%f \n MPDATA,GYZ,1,,%f \n MPDATA,GXZ
        ,1,,%f \n MPTEMP,,,,,,,, \n MPTEMP,1,0 \n MPDATA,DENS,1,,%d \n ',Ex,Ey,
        Ez,vL,Gxz,Gyz,Gxy,dens);
29
30  %%
31  %Element Properties
32  fprintf(fid,' ET,1,SHELL181\n KEYOPT,1,1,0\n KEYOPT,1,3,2 \nKEYOPT,1,8,2 \
        nKEYOPT,1,9,0\n');
33
34  %% Thickness distribution
35  t1=0.0125;
36  t2=0.0025;
37  t3=0.005625;
38  t4=0.00375;
39  t5=0.00375;
40  t6=0.0025;
41  t7=0.0025;
42
43  fprintf(fid,'\n t1=0.0125\n t2=0.0025 \n t3=0.005625 \n t4=0.00375 \n t5
        =0.00375 \n t6=0.0025 \n t7=0.0025');
44
45
46  %%
47  %%Composite stack and fibre layer orientation
48
49  fprintf(fid,'\nsect,1,shell,,root \n secdata,t1,1,90,3 \n secdata,t1,1,90,3
         \n secdata,t1,1,25,3 \n secdata,t1,1,-45,3 \n secdata,t1,1,-45,3 \n
        secdata,t1,1,25,3 \n secdata,t1,1,90,3 \n secdata,t1,1,90,3 \n
        seccontrol,0,0,0,0,1,1,1 \n secoffset,MID');
50  fprintf(fid,'\nsect,2,shell,,web \n  secdata,t2,1,90,3 \n secdata,t2,1,90,3
         \n secdata,t2,1,25,3 \n secdata,t2,1,-45,3 \n secdata,t2,1,-45,3 \n
        secdata,t2,1,25,3 \n secdata,t2,1,90,3 \n secdata,t2,1,90,3 \n \n \n
        secoffset,MID \n seccontrol,0,0,0,0,1,1,1 \n');
51  fprintf(fid,'\nsect,3,shell,,sec1  \n secdata,t3,1,90,3 \n secdata,t3
        ,1,90,3 \n secdata,t3,1,25,3 \n secdata,t3,1,-45,3 \n secdata,t3,1,-45,3
```

```
\n secdata,t3,1,25,3 \n secdata,t3,1,90,3 \n secdata,t3,1,90,3 \n
    secoffset,MID \n seccontrol,0,0,0,0,1,1,1');
fprintf(fid,'\nsect,4,shell,,sec2 \n secdata,t4,1,90,3 \n secdata,t4,1,90,3
    \n secdata,t4,1,25,3 \n secdata,t4,1,-45,3 \n secdata,t4,1,-45,3 \n
    secdata,t4,1,25,3 \n secdata,t4,1,90,3 \n secdata,t4,1,90,3 \n secoffset
    ,MID \n seccontrol,0,0,0,0,1,1,1');
fprintf(fid,'\nsect,5,shell,,sec3 \n secdata,t5,1,90,3 \n secdata,t5,1,90,3
    \n secdata,t5,1,25,3 \n secdata,t5,1,-45,3 \n secdata,t5,1,-45,3 \n
    secdata,t5,1,25,3 \n secdata,t5,1,90,3 \n secdata,t5,1,90,3 \n secoffset
    ,MID \n seccontrol,0,0,0,0,1,1,1');
fprintf(fid,'\nsect,6,shell,,sec4\n secdata,t6,1,90,3 \n secdata,t6,1,90,3
    \n secdata,t6,1,25,3 \n secdata,t6,1,-45,3 \n secdata,t6,1,-45,3 \n
    secdata,t6,1,25,3 \n secdata,t6,1,90,3 \n secdata,t6,1,90,3 \n secoffset
    ,MID \n seccontrol,0,0,0,0,1,1,1');
fprintf(fid,'\nsect,7,shell,,sec5 \n secdata,t7,1,90,3 \n secdata,t7,1,90,3
    \n secdata,t7,1,25,3 \n secdata,t7,1,-45,3\n secdata,t7,1,-45,3 \n
    secdata,t7,1,25,3 \n secdata,t7,1,90,3 \n secdata,t7,1,90,3 \n secoffset
    ,MID \n seccontrol,0,0,0,0,1,1,1 \n');


%%
%Node generation

[y,b]=size(mesh);
fprintf(fid,'! Keypoints List\n!\n');
for l=1:1:y
        fprintf(fid,'N, %d, %f, %f, %f ! \n',l,mesh(l,2),mesh(l,3),mesh(l,4))
            ;
end

%%
%Element generation

[y,b]=size(A);
fprintf(fid,'!\n!Elements List \n!\n');

for l=1:1:y
        fprintf(fid,'E, %d, %d, %d, %d ! \n',A(l,1),A(l,2),A(l,3),A(l,4));
end
```

```
76
77 %%
78 %Assignement of the material properties to the respective set of elements
79  fprintf(fid,'ESEL,ALL\n');
80  fprintf(fid,'EMODIF,ALL,SECNUM,2\n');
81
82  fprintf(fid,'\nESEL,ELEM,1,%d\n',max(sec_root));
83  fprintf(fid,'EMODIF,ALL,SECNUM,1\n');
84
85  sec_root2=max(sec_root)+n_elemz*n_elemc;
86  fprintf(fid,'\nESEL,ELEM,%d,%d\n',n_elemc*n_elemz+1,sec_root2);
87  fprintf(fid,'EMODIF,ALL,SECNUM,1\n');
88
89  fprintf(fid,'\nESEL,ELEM,%d,%d\n',sec_num1(1),max(sec_num1));
90  fprintf(fid,'EMODIF,ALL,SECNUM,3\n');
91
92  sec2_num1=max(sec_num1)+n_elemz*n_elemc;
93  fprintf(fid,'\nESEL,ELEM,%d,%d\n',n_elemc*n_elemz+sec_num1(1),sec2_num1);
94  fprintf(fid,'EMODIF,ALL,SECNUM,3\n');
95
96  fprintf(fid,'\nESEL,ELEM,%d,%d\n',sec_num2(1),max(sec_num2));
97  fprintf(fid,'EMODIF,ALL,SECNUM,4\n');
98
99  sec2_num2=max(sec_num2)+n_elemz*n_elemc;
100 fprintf(fid,'\nESEL,ELEM,%d,%d\n',n_elemc*n_elemz+sec_num2(1),sec2_num2);
101 fprintf(fid,'EMODIF,ALL,SECNUM,4\n');
102
103 fprintf(fid,'\nESEL,ELEM,%d,%d\n',sec_num3(1),max(sec_num3));
104 fprintf(fid,'EMODIF,ALL,SECNUM,5\n');
105
106 sec2_num3=max(sec_num3)+n_elemz*n_elemc;
107 fprintf(fid,'\nESEL,ELEM,%d,%d\n',n_elemc*n_elemz+sec_num3(1),sec2_num3);
108 fprintf(fid,'EMODIF,ALL,SECNUM,5\n');
109
110 fprintf(fid,'\nESEL,ELEM,%d,%d\n',sec_num4(1),max(sec_num4));
111 fprintf(fid,'EMODIF,ALL,SECNUM,6\n');
112
113 sec2_num4=max(sec_num4)+n_elemz*n_elemc;
114 fprintf(fid,'\nESEL,ELEM,%d,%d\n',n_elemc*n_elemz+sec_num4(1),sec2_num4);
```

```
115 fprintf(fid,'EMODIF,ALL,SECNUM,6\n');
116
117 fprintf(fid,'\nESEL,ELEM,%d,%d\n',sec_num5(1),max(sec_num5));
118 fprintf(fid,'EMODIF,ALL,SECNUM,7\n');
119
120 sec2_num5=max(sec_num5)+n_elemz*n_elemc;
121 fprintf(fid,'\nESEL,ELEM,%d,%d\n',n_elemc*n_elemz+sec_num5(1),sec2_num5);
122 fprintf(fid,'EMODIF,ALL,SECNUM,7\n');
123
124 fprintf(fid,'\nESEL,ELEM,%d,%d\n',sect2_elem(1),sect2_elem(sect2_num));
125 fprintf(fid,'EMODIF,ALL,SECNUM,2\n');
126
127
128 %%
129 %Constraints
130 k=1;
131 fprintf(fid,'!\n!Nodal Constrain at blades root\n!\n');
132 for i=1:1:2*n_elemz+2
133     for j=1:1:2*n_elemc+2
134      if mesh(k,4)== 0
135          fprintf(fid,'d,%d,all\n',k);
136      end
137      if k <= 2*n_elemc*n_elemz+2
138      k=k+1;
139      else
140          break;
141     end
142     end
143 end
144
145 fprintf(fid,'\nESEL,ALL');
146
147 %%
148 %Force assignment to each elemnet
149
150 for i=1:1:n_elemz*n_elemc
151           fprintf(fid,'\nESEL,ELEM,%d,',i);
152           fprintf(fid,'\nSFE,ALL,2,PRES,,%f,,,',F(i));
153 end
```

```
154
155 for  i=n_elemz*n_elemc+1:1:n_elemz*n_elemc*2
156             fprintf(fid,'\nESEL,ELEM,%d,',i);
157             fprintf(fid,'\nSFE,ALL,1,PRES,,%f,,,',F(i));
158 end
159
160 fprintf(fid,'\nESEL,ALL');
161 fclose(fid);
```